論文 / 著書情報
Article / Book Information

題目(和文)	
Title(English)	Effect of inherent mineral content on waste tire char (co) gasification
著者(和文)	HUNGWEDouglas
Author(English)	Hungwe Douglas
出典(和文)	学位:博士（工学）, 学位授与機関:東京工業大学, 報告番号:甲第11811号, 授与年月日:2022年3月26日, 学位の種別:課程博士, 審査員:高橋 史武,中﨑 清彦,CROSS JEFFREY SCOTT,江頭 竜一,時松 宏治
Citation(English)	Degree:Doctor (Engineering), Conferring organization: Tokyo Institute of Technology, Report number:甲第11811号, Conferred date:2022/3/26, Degree Type:Course doctor, Examiner:,,,,
学位種別(和文)	博士論文
Type(English)	Doctoral Thesis

EFFECT OF INHERENT MINERAL CONTENT ON WASTE TIRE CHAR (CO) GASIFICATION

Douglas Hungwe

Supervisor: Professor Fumitake Takahashi

A doctoral thesis submitted to

Department of Transdisciplinary Science and Engineering

School of Environment and Society

Tokyo Institute of Technology

March, 2022

Abstract

Waste tire thermochemical conversion via gasification is a promising and sustainable method for simultaneous disposal and energy harvesting from an otherwise problematic waste stream. However, although the subject has garnered interest, the effect of inherent mineral content during (co) gasification has not been reported. Therefore, this work addresses this research gap using an unconventional method. High-ash tire tread and low-ash sidewall char were used as the basis of comparison due to their wide difference in ash content and similar chemical structure. Inherent ash increases activation energy and suppresses size reduction and pore development during gasification. The char-ash transformation of low-ash and high-ash tire char can be described by the zeroth-order reaction and the random pore model. Inherent mineral content negatively impacts reactivity due to the formation of silica-based ash clusters that encapsulate residual carbon and impose diffusion resistance at high conversions. As a recourse, tire char was co-gasified with coconut fiber hydrochars. Cogasification is divided into the pyrolysis stage and the gasification stage. Deoxygenation reactions characterize the pyrolysis stage, while the gasification stage is characterized by activation energy reduction. Tar reforming is more pronounced for Zn-rich tire tread than sidewall due to the catalytic properties of Zn. The extent of synergistic interactions is also hampered by SiO_2 which deactivates active potassium species. These results can be used to justify the separation of tire tread and sidewall char prior gasification to avoid these ash-related problems.

KEY WORDS: Gasification kinetics, Random pore model, Zeroth order reaction, Morphological evolution Hydrothermal Treatment, Demineralization, Synergy, Reactivity, Catalytic tar reforming.

Acknowledgements

This doctoral thesis was completed with the support and contribution of many people. Therefore, I would like to express my sincere gratitude to:

- Associate Professor Fumitake Takahashi, as my supervisor, for his continuous research guidance, discussions, encouragement, and research opportunities.
- Professor Emeritus Kunio Yoshikawa for research opportunities and research funding during my studies.
- Associate Professor Koji Tokimatsu for his support and recommendations
- MEXT, for scholarship support
- The thesis committee members, for constructive feedback and suggestions.
- Dr. Hazel Bantolino Gonzales**,** Dr. Lu Ding, Dr. Saleem Ullah, Sarrut Theppitak, Dr. Reza Khushbouy, and Dr. Petri Kilpeläinen for their support in carrying out some experiments, analysis and suggesting revisions to my manuscripts
- Special thanks to Chido Hove, Charles Davu, and Liberty Mguni for their support

Finally, I am deeply grateful to my wife, daughter, and parents *vari kwaDunira* for their endless love and support.

Contribution of the author

Paper I.

Kinetics and Physicochemical Morphology Evolution of Low and High-Ash Pyrolytic Tire Char during CO_2 Gasification

***Hungwe, D.**; Ding L.; Khoshbouy R.; Yoshikawa K.; Fumitake T.*

Hungwe contributed to the planning of the work, carried out all experiments, and wrote the first draft of the paper. This paper published in the *Energy & Fuel 2020, 34, 1, 118–129* and is presented in chapter two of this thesis.

Paper II.

Potassium demineralization of coconut fiber via combined hydrothermal treatment and washing: Effect on pyrolysis kinetics, mechanisms, and bio-oil composition

***Hungwe, D.**; Ullah, S.; Kilpeläinen, P.; Theppitak S.; Ding L.; Fumitake T.*

Hungwe participated in the planning of the work, collaborated in the experimental work, evaluated the results, and wrote the paper. This paper was published in *Biomass and Bioenergy 2021, 152 106194*; part of the findings is presented in chapter three of this thesis.

Paper III.

Effect of Tire-Char Ash on the Extent of Synergy during CO_2 Cogasification with Hydrochar from Potassium-Rich Coconut Fiber

***Hungwe, D.**; Khoshbouy R.; Ding L.; Ullah, S.; Yoshikawa K.; Fumitake T.*

Hungwe contributed to the planning of the work, carried out all experiments, and paper writing. The work is published in the *Energy & Fuels 2020, 34, 8110−811*. This report is part of chapter four in this thesis.

Table of contents

List of figures

List of tables

Chapter 1: **Introduction**

1.1 Background

World population growth and great advances in technology have catalyzed an increase in socio-economic activities that involve large scale production, consumption of commodities and finally waste generation. The increase in these activities has resulted in a wide range of environmental problems. One of the problems that has become a global concern is waste tire disposal, in 2017 alone, the global tire demand peaked at 2.9 billion tons and almost a billion tires were disposed in the same year [1]. However, appropriate facilities for handling such volumes of waste tire are not yet in place contributing to serious environmental problems. Mahlangu reported that over 160 000 tons of scrap tires are generated in southern Africa annually and approximately 28 million tires are dumped illegally, and estimated to increase by 9.3 million annually [2]. End-of-life tire generation per GDP in this region is higher than that of the European union or the United States because, some tires considered not road-worthy in these countries can be used in Africa because of different safety standards, consequently African countries are a market for these tires which have less than normal road life [3].

In the case of Zimbabwe, most tires are dumped illegally in open space, with some being disposed of in landfills, wherein tires remain intact for over a decade due to their resistance to chemical and biological degradation [4]. Recycling and generation of other valuable secondary products from waste tires will contribute to a reduction on environmental pollution. The reprocessing of scrap tires represents a large energy resource and thus it would be beneficial to convert old tires to a usable energy form [3–5]. Tires' contain high volatile matter and carbon; this leads to high heating values, making them suitable for high energy recovery with a suitable technology [1,3–9]. The polymeric elastomers in tires lead to heating value as high as 35.6 MJ/kg [10]. The preferred processes for energy recovery, waste treatment and production of secondary value added products, are: pyrolysis, gasification and incineration [11].

There is a strong possibility of gasification of old tires in already existing gasification facilities, as such this work will be focused on gasification.

1.2 Composition of waste tires

Pneumatic tires contain: vulcanized rubber, a rubberized fabric containing reinforcing textile cords, steel or fabric belts, and steel-wire-reinforced rubber beads and additives as shown in

Figure 1-1 [12]. Styrene-butadiene-copolymer (SBR) contains about 25 wt.% styrene and is the most generally used vulcanized tire rubber. A blend of SBR with other elastomers such as natural rubber (cis-polyisoprene), synthetic cis-polyisoprene, and cis-polybutadiene are also used in tires in varying quantities [13]. The heat content of the rubber tires is higher than that of coal, thus tire rubber can be a substitute fuel source for power generation. Waste tires have a better burning efficiency and heat value than coal, thus they can replace coal resources to generate power, provided that their collection is coordinated and a constant supply is available [2].

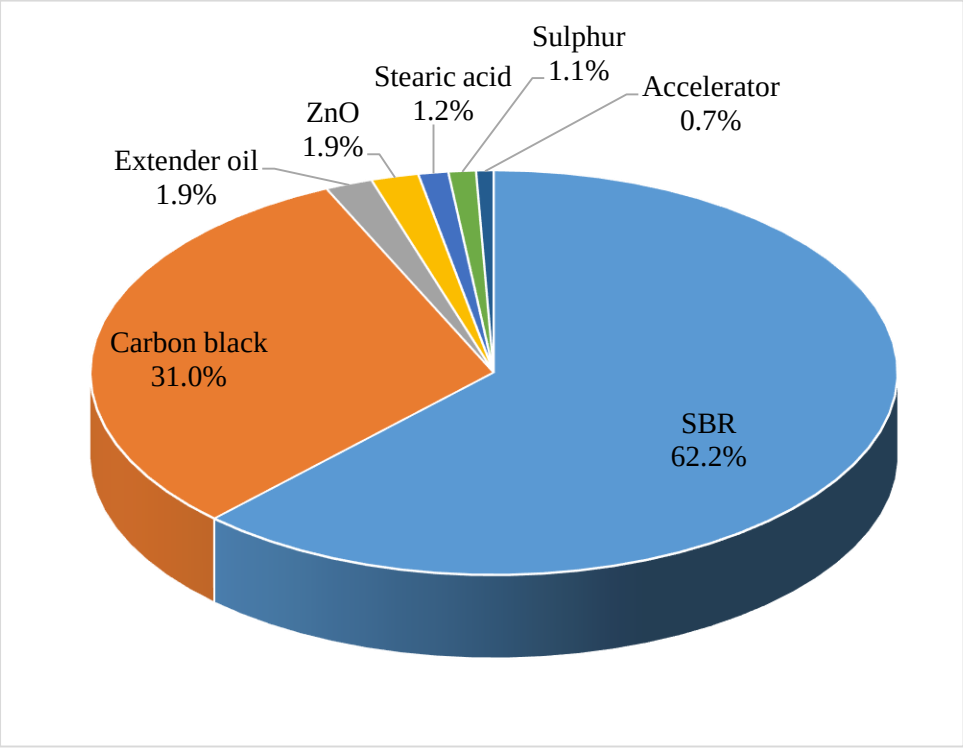

Figure 1-1. Typical composition of a passenger vehicle tire

Carbon black primarily strengthens and imparts abrasion resistance to the rubber. Clay or silica is sometimes used to partial replacement carbon black [12,13]. The extender oil is a mixture of aromatic hydrocarbons and is used to soften the rubber to make it more workable. Sulfur molecules harden the rubber and prevent deformation at elevated temperature by reacting with the double bonds in adjacent polymer chains to cause cross-linking. Additives which are typically an organosulfur compound such as 2-mercaptobenzothiazole act as catalyst for the vulcanization process. The zinc oxide enhances the physical properties of the rubber and acts in harmony with the additives to control the vulcanization process.

1.3 Gasification process and reactions

Gasification is the thermochemical conversion of a solid/liquid carbon-based material into a combustible gas (for use in power generation) by introducing a gasification agent at high temperatures [14,15]. In common terms, the gasification process is the partial or total transformation of solid fuels into gases, which is accomplished by thermal conversion, chemical reactions, and a combination of both. The main gasifying agents used are air, steam, and oxygen; however, a mixture of CO_2-rich flue gas and oxygen has gained popularity due to its ability to suppress NOx emissions and reduce energy consumption during oxyfuel combustion [16,17].

There are three types of reactors used for gasification purposes: fluidized bed, entrained flow, and fixed bed (updraft and downdraft) reactors (Figure 1-2).

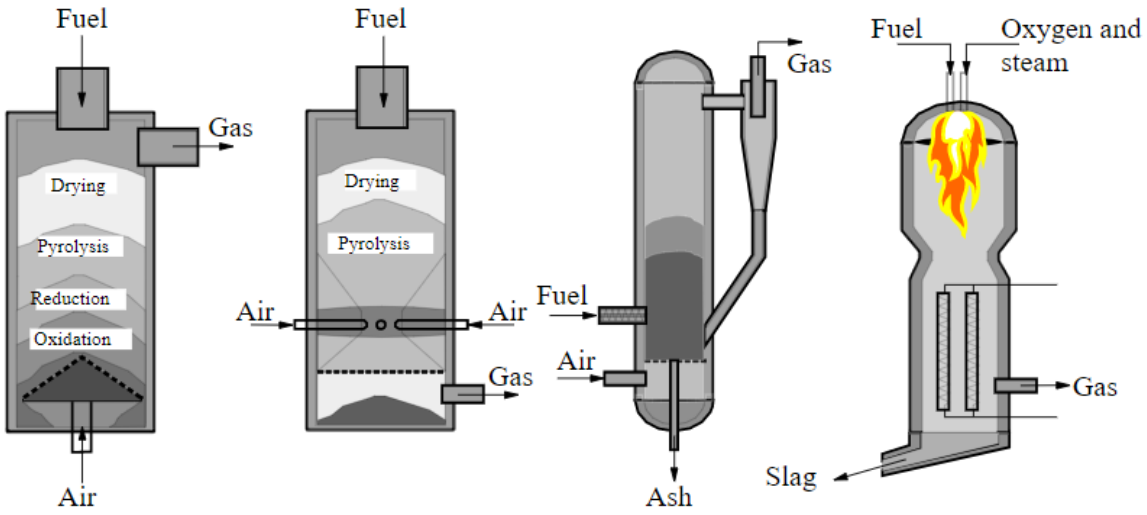

Figure 1-2. Types of gasifiers

The main differences between these gasifiers include, and are not limited to: gasification agent, mode of feedstock introduction and movement within the reactor, range of operating temperature and pressure, and the heating mode of the reactor, which can be either direct and indirect.

In a typical entrained flow, gasifier feedstock and gasification agent are introduced from the part, and the syngas and slag exist from the bottom. As the fuel particles traverse down the reactor, the temperature increases gradually. The first steps of tire transformation are the drying and pyrolysis stages, in which charring occurs within milliseconds. In the pyrolysis stage, primary and secondary decomposition reactions occur. Primary reactions involve the

decomposition of a tire into heavy hydrocarbons, light hydrocarbons and char [18]. The hydrocarbons are thereafter cracked and reformed to form low molecular weight hydrocarbons such as C_2H_4, C_2H_6, C_3H_6 and C_3H_8. Then, the hot charred particles react with the oxidizing agent through a combination of combustion and gasification reactions. The prominent reaction is controlled by regulating the concentration of the oxidizing agent. Gasification is achieved by limiting the concentration of oxidizing agents; consequently, combustion reactions are suppressed. Many reactions occur simultaneously within the reactor. The most predominant tire gasification reactions are expressed in following equations.

Complete oxidation:	$C + O_2 \rightarrow CO_2$	$\Delta H_{25°C} = -394 kJ/mol$	(1-1)
Partial oxidation:	$C + 0.5O_2 \leftrightarrow CO$	$\Delta H_{25°C} = -111 kJ/mol$	(1-2)
Water-gas (primary):	$C + H_2O \leftrightarrow CO + H_2$	$\Delta H_{25°C} = +131 kJ/mol$	(1-3)
Water-gas shift:	$CO + H_2O \leftrightarrow CO_2 + H_2$	$\Delta H_{25°C} = -41.2 kJ/mol$	(1-4)
Methanation:	$CO + 3H_2 \leftrightarrow CH_4 + H_2O$	$\Delta H_{25°C} = -206 kJ/mol$	(1-5)
CO_2 char gasification:	$C + CO_2 \leftrightarrow 2CO$	$\Delta H_{25°C} = +172 kJ/mol$	(1-6)

The CO_2 char gasification reactivity is the slowest, therefore for gasification purposes this reaction is the rate determining step for the whole process [19,20].

1.4 Research on waste tires gasification

Tire gasification research has gained traction over the years. Most studies are, however conducted under laboratory scale facilities [5]. There are fewer pilot and commercial publications. Typically, fundamental gasification studies are carried out using thermogravimetric analysis (TGA) [7,14,21–26]. Thermochemical conversion (pyrolysis, gasification and combustion) characteristics determined used TGA can provide a reliable reference for fixed bed and entrained flow reactors [27,28]. Burhenne et al. [28] observed that the reaction rate and product distribution of different biomass in TGA were similar to that in fixed bed reactors. Kajitani et al. [27] found that the reaction rate curve of the pressurized drop tube furnace is the extension of the TGA rate curve under intrinsic conditions. Therefore, the intrinsic kinetics of TGA can provide reference for kinetics of a drop tube furnace, which is a miniature entrained flow gasifier. Therefore, not only the data of the pressurized drop tube

furnace, but also that of the TGA can be used as a reliable reference for industrial scale gasification reactors.

Table 1-1 shows recent fundamental studies in tire gasification carried out in laboratory-scale facilities, of which most of them are based on the TGA. The studies can be broadly divided into classes; gasification [7–10,22,29] and co-gasification [6,24–26]. In gasification studies, intrinsic gasification kinetics for CO_2-char gasification were obtained by modeling char-ash transformation according to the random pore, volumetric, and shrinking core, or a modified version of these classic models in the temperature range of 800 - 1200°C.

Table 1-1. Recent fundamental studies in tire gasification

Year	Authors	Type of reactor	Gasifying agent	Summary of work
1996	Lee and Kim [10]	Thermo-balance reactor Laboratory scale	CO_2	The effect of particle size on tire gasification rate was investigated for particle size range of 0.25 mm to 1 mm. Gasification rate was found to be independent of particle size
2001	Li et al [5]	TGA Laboratory scale	CO_2	The study reports on the CO_2 gasification reactivity of tire char produced by a rotary kiln. The activity energy ranged between 248 kJ/mol and 383 kJ/mol
2004	Murillo et.al [22]	TGA Laboratory scale	CO_2	In this study, the intrinsic kinetics for activation of pyrolysis tire char was carried out in a thermobalance at different temperatures (850, 900, 950 and 1000 ◦C) in order to determine the activation energy and pre-exponential factor, basic intrinsic kinetic parameters of the activation process. It was found that the activation process was described by the random pore model and it is a first order reaction with an activation energy of 197.7 kJ/mol and a pre-exponential factor of 15.33 m/s.
2006	Gonzalez et.al [29]	TGA Laboratory scale	Steam & CO_2	In this study, activated carbons were prepared from waste tires gasification using steam and carbon dioxide. Activated carbon produced from steam gasification had higher porosity and surface than those produced using carbon dioxide as the gasifying agent.
2013	Lahijani et.al [24]	TGA Laboratory scale	CO_2	In this study, the effect of blending tire char with either palm empty fruit bunch (EFB) and almond shell (AS) on reactivity enhancement was carried out in a TGA. The co gasification of tire-char/AS-char and tire-char/EFB increased conversion rate by a factor of 5 and 10 respectively, due to the presence of alkaline and alkaline earth metals in biomass
2019	Isaac et. al [6]	TGA Laboratory scale	CO_2	In this study, intrinsic gasification kinetics of waste tire char and acid-demineralized tire char was evaluated for co-gasification with Australian coal. The activation energy of tire char and demineralized char was 174.87 kJ/mol and 177.03 kJ/mol.

2019	Preciado-Hernandez et.al [9]	Fixed bed reactor	CO_2	The objective of this study was to determine the experimental gasification kinetics for tire pyrolysis char during activation in a fixed bed reactor under atmospheric pressure. The reaction order, activation energy and pre-exponential factor were found to be 0.7, 112 kJ mol^{-1} and 6.24 × 10−4 s^{-1}, respectively
2020	Betancur et. al [7]	TGA Laboratory scale	CO_2	The main goal of this study was to assess which reaction model could predict the gasification behavior of tire pyrolysis char. Reaction models considered were the Changing Grain Size Model (CGSM), the Random Pore Model (RPM) and a new model based on the RPM named the Hybrid Modified Random Pore Model (HMRPM). It was found that the reaction could be described by the HMRPM, which yielded 0.543, 147.27 kJ/mol and 4.547 × 105 s^{-1}, for reaction order, activation energy and pre-exponential factor, respectively.
2020	Lahijani et.al [26]	TGA Laboratory scale	CO_2	In this paper, an investigation of synergy and inhibition effects during co-gasification of tire char (TC) and rambutan peel (RP) in CO_2 environment was carried out in a TGA. Activation reduction was proportional to the amount of biomass blended with TC. Tire char activation energy was reduced from 297 kJ/mol to a range of 216 to 273 kJ/mol. for blends with 15 - 85% biomass.
2021	Jansen et. al [8]	TGA Laboratory scale	CO_2	Empirical isothermal kinetics for tire gasification was derived from TGA data using different models under atmospheric pressure and the results showed that gasification could be described by the shrinking sphere, reaction control model and the activation energy obtained was in the range 201.7 - 223.1 kJ/mol.

It is reported that the range of energy required to initiate the gasification reaction was found to be in the range of 121 - 383 kJ/mol [5,30]. This wide range of activation energies values can be attributed to several factors, including ash content, type of carbon black in tire char, thermal history of char, specific surface area of chars, and resultant carbon chemical structure. Interestingly, although the mineral content in the tire was found to be wide (5 – 20 wt%) [31], its effect on gasification behavior has not received much attention.

Tire char has a low reactivity due to its highly graphitic carbon structure, low heteroatoms (oxygen and hydrogen) concentration, and high acidic minerals such as sulfur and silica [24,25]. In addition, silica deactivates catalytic minerals and causes gas diffusion resistance during gasification. Consequently, tire char is often blended with alkaline and alkaline earth metal-rich biomass to improve reactivity [15]. Biomass is a source of heteroatoms and AAEMs which catalyze the gasification reactions via suppressing graphitization during conversion. Lahijani et. al [24,25] confirmed the presence of synergistic interaction during cogasification of tire char with palm empty fruit bunch (EFB), almond shell (AS) and rambutan peel (RP). In these studies,

the activation energy was decreased and the extent of decrease was directly proportional to the concentration of AAEMs in the blends.

Recently, Issac et al. [6] reported on the intrinsic kinetics underpinning co-gasification of a waste tire and coal char. They found that blends decreased reactivity as the proportion of tire char increased due to enhanced ash melting, which encapsulated unreacted carbon and increased gas diffusion resistance. These findings suggest that the acid-demineralization method may not be a suitable approach to studying the effect of mineral content on tire gasification behavior.

1.5 The acid-mineralization method

When investigating the effect of mineral content/ash, ideally an ash-rich sample is demineralized, thereafter, the treated and untreated sample are used as a basis for comparison. The acid demineralization method is mostly used for samples containing a large proportion of acid-soluble mineral content such as conventional fuels (biomass and coal) [32]. However, this method has its limitations, particularly for tire char produced at high temperatures (≥ 1000°C). Tire char is rich in acid-insoluble silica and alumina, furthermore, when subjected to high pyrolysis temperatures, silica also reacts with ZnO and other alkaline and alkaline earth metals to produce acid insoluble silicates. Consequently, the proportion of acid insoluble increases thus further reducing the efficiency of acid demineralization. The presence of rubber remnants in the char also reduces the accessibility of otherwise acid soluble species. One research group [6] attempted to investigate the effect of acid-demineralization on tire gasification kinetics, they reduced the ash content from 15.24 to 9.1 wt%, however the activation energy only increased from 174.87 kJ/mol to 177.03 kJ/mol and no significant differences in gasification behaviour were reported. For this reason, an alternative approach to investigating the effect of ash during tire gasification is necessary.

1.6 Research gaps in gasification studies

The literature review shows that many studies focused on gasification kinetics. However, the effect of inherent mineral content on (co) gasification behavior did not receive much attention. Therefore, an alternative approach to the acid demineralization method is suggested and reported in this work.

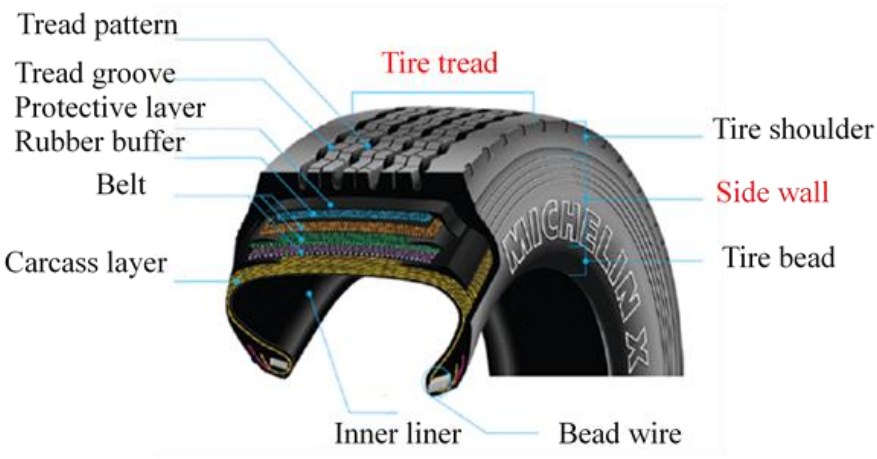

Figure 1-3. Cross section of a pneumatic tire

To successfully investigate the role of mineral content on gasification, two chars of similar chemical carbon structures but widely different ash content must be compared. This criterion made the authors review the typical structure of the waste tire. The Figure 1-3 shows that waste tires can be divided into two main parts, sidewall (SW) and tire tread (TT). These results in two distinct chars that can be used as a basis for comparison. TT is the reinforced hard rubber on the tire circumference that makes contact with the ground. The SW, on the other hand, does not make contact with the road. It is a relatively flexible rubber whose primary purpose is to contain air. Wang et al. [31] reported the dissimilarity between SW and TT ash composition; ash content was 2% and 18%, respectively. The chemical structure of tire char as characterized by Raman spectroscopy is shown in Figure 1-4.

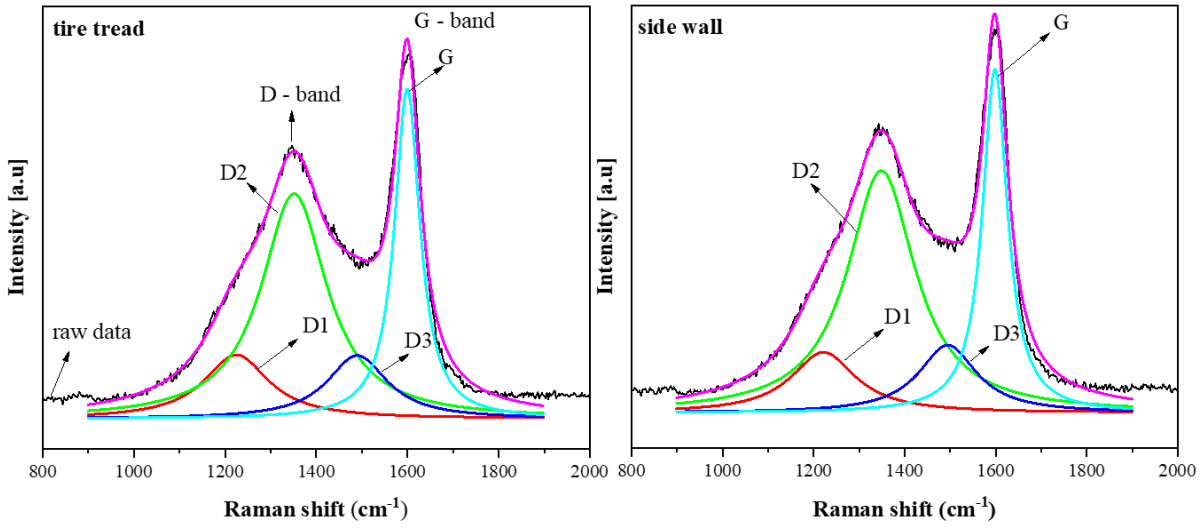

Figure 1-4. Raman spectra and fitted curves of tire tread and sidewall char

Two characteristic peaks appear at ~1350 cm^{-1} (D band) for disordered carbon phase and ~1580 cm^{-1} (G band) for the graphene 2D hexagonal lattice. The Raman spectra were further deconvoluted into 4 bands. The D1 band represents poorly organized carbonaceous materials, such as soot and rubber remnants [33]. The D2 band is characterized by the vibration mode of disordered graphitic lattices with in-plane imperfections, such as defects and heteroatoms [34]. The D3 band is attributed to the sp2 bond, in amorphous carbon, including organic molecules and s of functional group fragments [35]. The G band is related to the stretching vibration of the carbon atom within the polyaromatic structure [36]. The ratio A_G/A_{all} (area under curve fits), which reflects the extent of graphitization in char, is 0.260 for SW and 0.269 for TT. Raman results confirm a similar chemical structure of chars and, therefore, TT and SW can be used as a basis of comparison without the need for acid demineralization.

A recent research group [26] investigated synergism and kinetic analysis during the cogasification of tire char and agro wastes, and they reported that non-isothermal conversion is divided into the pyrolysis and gasification stage for agro waste. In contrast, tire char has only one stage, gasification.

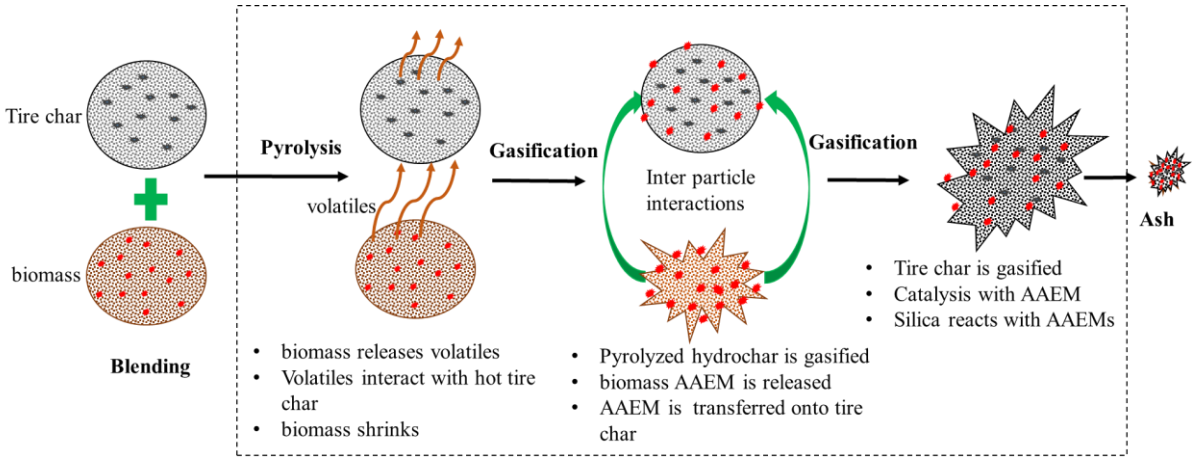

Figure 1-5. Cogasification mechanism of tire char and AAEMs-rich biomass

In the pyrolysis stage, biomass evolved volatiles interacts with hot tire char; however, the nature of these interactions cannot be determined quantitatively using the TGA. Therefore, this study, investigates the nature of these interactions using a large scale fixed bed pyrolysis reactor to gain a holistic understanding of the cogasification process. The main stages of the cogasification mechanism are summarized in Figure 1-5.

1.7 Research objectives

This study investigates the effect of inherent tire ash on (co) and gasification behavior. (1) The first objective is evaluating the effect of ash on char-CO_2 gasification kinetics, reactivity, and morphological evolution. (2) The second objective is to produce hydrochar from coconut fiber by hydrothermal treatment for gasification with waste tire char. The effect of hydrothermal treatment intensity on fuel enhancement, potassium demineralization, and the first stage of gasification (pyrolysis) is evaluated. (3) The last objective is to determine the interactions during co-gasification by comparing low-ash and high ash tire char: 1. bio-volatiles and tire char interactions during the pyrolysis and 2. synergy, reactivity, and activation reduction in the gasification stage.

1.8 Thesis outline

The content of this thesis is divided into 5 chapters, as follows

Chapter 1. Introduction

The introduction outlines the background and motivation for potentially solving the waste tire problem through thermochemical conversion (gasification). The gasification process is also described with special emphasis on the most prevalent chemical reactions and the reactors within which gasification occurs. Recent fundamental studies on gasification using laboratory-scale facilities are reviewed, and research gaps are identified. One notable research gap found was that the effect of ash on (co) gasification had not received much attention. The conventional acid-demineralization method often used to investigate the ash performance is not appropriate for tire char because tire char is rich in acid-insoluble minerals, and the otherwise acid-soluble species are inaccessible to acid action. A brief review of the acid-demineralization method is also provided. Low-ash sidewall and high-ash tire tread are compared to investigate the effect of inherent tire char ash on gasification behavior as an alternative to the acid-demineralization method. Finally, the research objectives and the thesis structure are stated

Chapter 2. Gasification kinetics and physicochemical morphological evolution of low and high-ash tire char

The heterogeneity of waste tire pyrolytic char associated with ash composition and distribution is explored to understand the effect of ash on gasification. In this chapter, high-ash tire tread (TT) and low-ash sidewall (SW) were separated to study gasification kinetics and the influence of ash on char physicochemical morphological evolution during CO_2 gasification. CO_2 gasification of chars were carried out in a TGA within the temperature range 850-925°C,

particle size ≤100 µm, 10 mg samples, and CO_2 flow rate 150 mL/min. The ash in SW and TT was 5.23 and 20. 6 wt%. The gasification profiles were modeled according to the shrinking core model (SCM), volumetric model (VM), the random pore model (RPM) and the zeroth order reaction model. While the TT gasification profiles could be modeled by the RPM, SW is described by the zeroth order reaction model. Activation energy for TT and SW is 177.1 and 165.6 kJ mol^{-1}, respectively. In addition, it was found that inherent ash in TT suppressed particle size reduction and pore structure development at conversion greater than 50% due to the formation of a silica-based skeletal structure that encapsulated residual carbon. Consequently, reaction time and the activation energy were increased. Conversely, SW char was characterized by significant size reduction. These findings further confirmed the inhibiting nature of tire ash.

Chapter 3. Effect of hydrothermal treatment on coconut fiber demineralization and pyrolysis behaviour

In this chapter, the effect of hydrothermal treatment (180 -220°C) on coconut fiber energy-enhancement, demineralization, pyrolysis behavior, and pyrolysates composition was investigated. The high heating value (HHV) of raw coconut fiber (RCF) improved 17.97 kJ/mol to 19.66, 20.62, and 21.53 MJ/kg after hydrothermal transformation at 180, 200, and 220°C due to an increase in dehydration reaction intensity. Chemical fractionation method classified the most occurring inorganic (potassium) as ~76% water-soluble, ~19% ion-exchangeable, and ~5% acid-soluble species. Demineralization results show that pretreatment at ≤200°C leached out most water-soluble and ion-exchangeable potassium. However, at 220°C, electrostatic attraction and increased tortuosity imposed by the high density of oxygenated functional groups and a well-developed porous structure hamper demineralization. Nevertheless, a maximum potassium removal efficiency of 95% could be achieved if followed by water-washing. Although pretreatment marginally affects apparent activation energy, the reaction mechanism of hydrochars became insensitive to the heating rate between 10 and 50°C min^{-1}. The composition of pyrolysis volatiles was determined using pyro-GC-MS at 600°C. Due to pretreatment, the selectivity of thermally stable phenolic and anhydrosugar derivatives increased at the expense of the light oxygenates of low thermal stability because of suppressing fragmentation reactions and enriching polymers with a high degree of polymerization. Light oxygenates decreased from 27.45 area % to 24.02, 16.33, and 13.32 area % for hydrochars produced at 180°C, 200°C, and 220°C, respectively. The high demineralization efficiency

achieved during pretreatment demonstrated that coconut fiber can be safely used for thermochemical conversion.

Chapter 4. Effect of inherent tire ash on co-gasification of biomass/hydrochar and tire char

The first section of this chapter determines the interactions between biomass volatiles produced during the pyrolysis stage and the hot tire char in a fixed bed reactor. It was found that zinc-rich TT char catalyzed tar reforming reactions and intensified deoxygenation reactions. The prominence of deoxygenation reactions was found to be in the following order: dehydration reactions > decarbonylation reactions > decarbonylation reactions.

The last section reports the influence of inherent tire-char ash during cogasification with coconut hydrochar prepared at different intensities in a TGA to ascertain the extent to which synergistic interaction, reactivity, and activation energy reduction were altered. High-ash tire tread (TT) and low-ash sidewall (SW) both exhibited enhanced synergy, reactivity, and activation reduction upon cogasification with hydrochars; however, the extent of promotion was more pronounced in SW− hydrochar blends. This difference was caused by the inhibiting nature of TT inherent ash, particularly the role of Si-containing compounds. Inhibition in TT−hydrochar blends was mainly due to the promotion of alkaline and alkaline earth metal transformation into inactive silicates and, to a lesser extent, the mass transfer effect caused by accumulated ash. The extent of enhancement correlated well with the concentration of available alkaline and alkaline earth metals. The findings may be useful in justifying the exclusion of high-ash tire char as gasification feedstock to mitigate ash- related problems. The TT can be used a sacrificial tar reforming agent instead.

Chapter 5. Conclusions and Recommendations

This chapter summarizes the major findings on the effect of inherent tire ash on gasification and co-gasification interactions using an unconventional approach. Finally, practical implications of the study are summarized and recommendations made for future work.

The relationship between each chapter was illustrated in Figure 1-6.

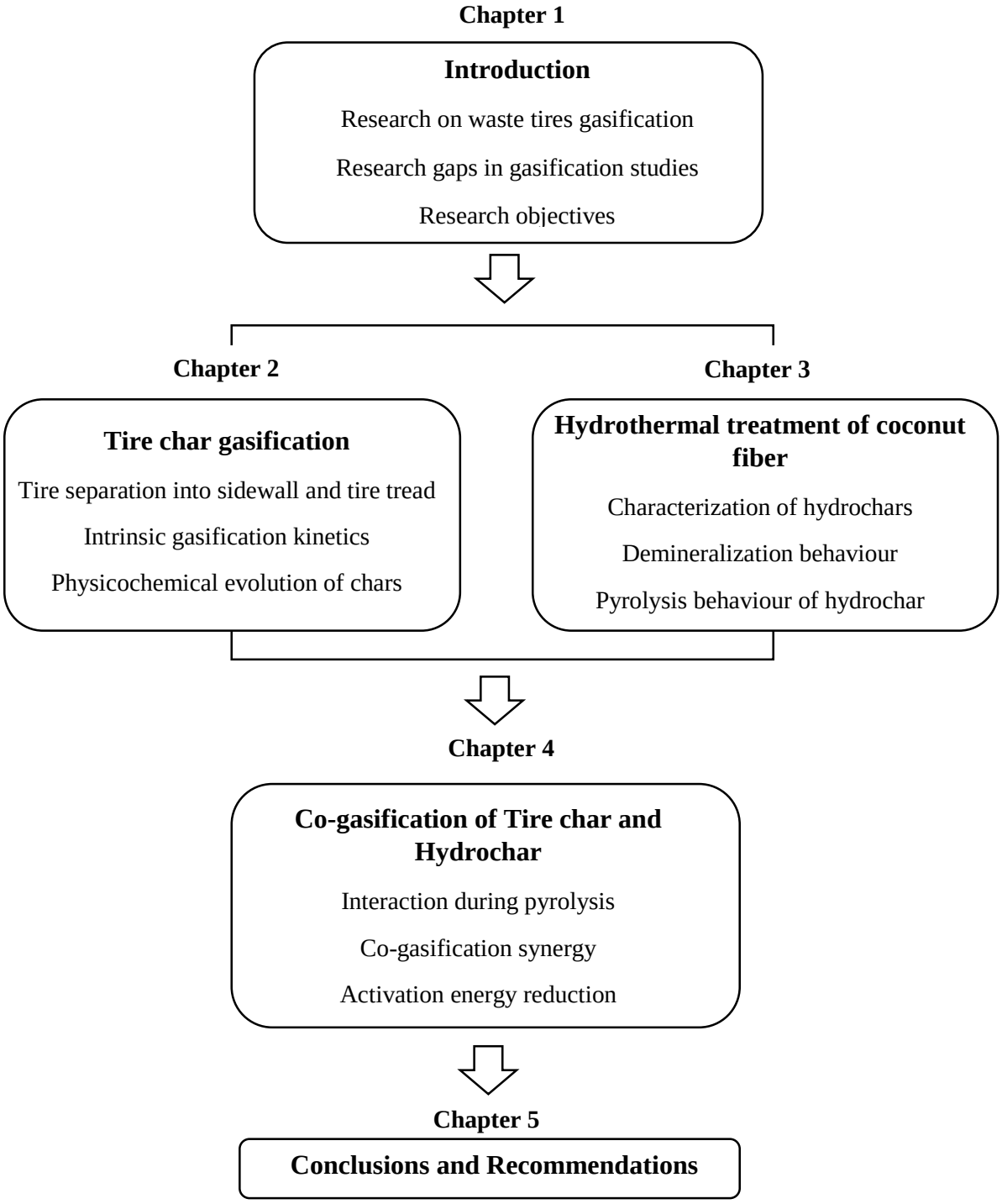

Figure 1-6. The thesis structure

References

[1] Wang Z, Burra KG, Lei T, Gupta AK. Co-gasification characteristics of waste tire and pine bark mixtures in CO_2 atmosphere. Fuel 2019;257:116025. https://doi.org/10.1016/j.fuel.2019.116025.

[2] Mahlangu LM. Waste Tire Management Problems in South Africa and the. UNIVERSITY OF SOUTH AFRICA, 2009.

[3] Sebola MR, Mativenga PT, Pretorius J. A Benchmark Study of Waste Tire Recycling in South Africa to European Union Practice. Procedia CIRP 2018;69:950–5. https://doi.org/10.1016/j.procir.2017.11.137.

[4] Adhikari B, Maiti S. Reclaimation and recycling of waste tires. Prog Polym Sci 2000;25:909–48.

[5] Oboirien BO, North BC. A review of waste tire gasification. J Environ Chem Eng 2017;5:5169–78. https://doi.org/10.1016/j.jece.2017.09.057.

[6] Issac M, Dai B, Zhang L. Kinetics underpinning the C-CO_2 gasification of waste tire char and its interaction with coal char upon co-gasification. Fuel 2019;256:115991. https://doi.org/10.1016/j.fuel.2019.115991.

[7] Betancur M, Natalia Arenas C, Daniel Martínez J, Victoria Navarro M, Murillo R. CO_2 gasification of char derived from waste tire pyrolysis: Kinetic models comparison. Fuel 2020;273:117745. https://doi.org/10.1016/j.fuel.2020.117745.

[8] Jansen AA, van der Walt IJ, Crouse PL. Waste-tire pyrolysis and gasification via the reverse Boudouard reaction: derivation of empirical kinetics from TGA data. Thermochim Acta 2021:179104. https://doi.org/10.1016/j.tca.2021.179104.

[9] Preciado-Hernandez J, Zhang J, Zhu M, Zhang Z, Zhang D. An experimental study of CO_2 gasification kinetics during activation of a spent tire pyrolysis char. Chem Eng Res Des 2019;149:129–37. https://doi.org/10.1016/j.cherd.2019.07.007.

[10] Lee JS, Kim SD. Gasification kinetics of waste tire-char with CO_2 in a thermobalance reactor. Energy 1996;21:343–52. https://doi.org/10.1016/0360-5442(95)00119-0.

[11] Labaki M, Jeguirim M. Thermochemical conversion of waste tires—a review. Environ Sci Pollut Res 2017;24:9962–92. https://doi.org/10.1007/s11356-016-7780-0.

[12] Williams PT. Pyrolysis of waste tires: A review. Waste Manag 2013;33:1714–28. https://doi.org/10.1016/j.wasman.2013.05.003.

[13] Amari T, Themelis NJ, Wernick IK. Resource recovery from used rubber tires. Resour

Policy 1999;25:179–88. https://doi.org/10.1016/S0301-4207(99)00025-2.

[14] Hungwe D, Ding L, Khoshbouy R, Yoshikawa K, Takahashi F. Kinetics and Physicochemical Morphology Evolution of Low and High-Ash Pyrolytic Tire Char during CO_2 Gasification. Energy and Fuels 2020;34:118–29. https://doi.org/10.1021/acs.energyfuels.9b03043.

[15] Hungwe D, Khushbouy R, Ullah S, Lu D, Yoshikawa K, Takahashi F. Effect of Tire-Char Ash on the Extent of Synergy during CO_2 Cogasification with Hydrochar from Potassium-Rich Coconut Fiber. Energy & Fuels 2020;34:8110–9. https://doi.org/10.1021/acs.energyfuels.0c00895.

[16] Butterman HC, Castaldi MJ. Influence of CO_2 injection on biomass gasification. Ind Eng Chem Res 2007;46:8875–86. https://doi.org/10.1021/ie071160n.

[17] McKendry P. Energy production from biomass (part 3): Gasification technologies. Bioresour Technol 2002;83:55–63. https://doi.org/10.1016/S0960-8524(01)00120-1.

[18] Pattabhi K. Of waste tires in a fluid bed reactor 1981;4:79–88.

[19] Umeki K, Moilanen A, Gómez-Barea A, Konttinen J. A model of biomass char gasification describing the change in catalytic activity of ash. Chem Eng J 2012;207–208:616–24. https://doi.org/10.1016/j.cej.2012.07.025.

[20] Ahmed II, Gupta AK. Kinetics of woodchips char gasification with steam and carbon dioxide. Appl Energy 2011;88:1613–9. https://doi.org/10.1016/j.apenergy.2010.11.007.

[21] Yang Y, Zhu J, Yang L, Zhu Y. Co-gasification characteristics of scrap tire with pine sawdust using thermogravimetric and a whole-tire gasifier reactor. Energy Procedia 2019;158:37–42. https://doi.org/10.1016/j.egypro.2019.01.031.

[22] Murillo R, Navarro M V., López JM, García T, Callén MS, Aylón E, et al. Activation of pyrolytic tire char with CO_2: Kinetic study. J Anal Appl Pyrolysis 2004;71:945–57. https://doi.org/10.1016/j.jaap.2003.12.005.

[23] Hungwe D, Ullah S, Kilpeläinen P, Theppitak S, Ding L, Takahashi F. Potassium demineralization of coconut fiber via combined hydrothermal treatment and washing: Effect on pyrolysis kinetics, mechanisms, and bio-oil composition. Biomass and Bioenergy 2021;152:106194. https://doi.org/10.1016/j.biombioe.2021.106194.

[24] Lahijani P, Zainal ZA, Mohamed AR, Mohammadi M. Co-gasification of tire and biomass for enhancement of tire-char reactivity in CO_2 gasification process. Bioresour

Technol 2013;138:124–30. https://doi.org/10.1016/j.biortech.2013.03.179.

[25] Lahijani P, Mohammadi M, Mohamed AR. Investigation of synergism and kinetic analysis during CO_2 co-gasification of scrap tire char and agro-wastes. Renew Energy 2019;142:147–57. https://doi.org/10.1016/j.renene.2019.04.113.

[26] Lahijani P, Mohammadi M, Mohamed AR. Investigation of synergy and inhibition effects during co-gasification of tire char and biomass in CO_2 environment. Biomass Convers Biorefinery 2020. https://doi.org/10.1007/s13399-020-01028-x.

[27] Kajitani S, Suzuki N, Ashizawa M, Hara S. CO_2 gasification rate analysis of coal char in entrained flow coal gasifier. Fuel 2006;85:163–9. https://doi.org/10.1016/j.fuel.2005.07.024.

[28] Burhenne L, Messmer J, Aicher T, Laborie MP. The effect of the biomass components lignin, cellulose and hemicellulose on TGA and fixed bed pyrolysis. J Anal Appl Pyrolysis 2013;101:177–84. https://doi.org/10.1016/j.jaap.2013.01.012.

[29] González JF, Encinar JM, González-García CM, Sabio E, Ramiro A, Canito JL, et al. Preparation of activated carbons from used tires by gasification with steam and carbon dioxide. Appl Surf Sci 2006;252:5999–6004. https://doi.org/10.1016/j.apsusc.2005.11.029.

[30] Preciado-Hernandez J, Zhang J, Jones I, Zhu M, Zhang Z, Zhang D. An experimental study of gasification kinetics during steam activation of a spent tire pyrolysis char. J Environ Chem Eng 2021;9:105306. https://doi.org/10.1016/j.jece.2021.105306.

[31] Wang M, Zhang L, Li A, Irfan M, Du Y, Di W. Comparative pyrolysis behaviors of tire tread and side wall from waste tire and characterization of the resulting chars. J Environ Manage 2019;232:364–71. https://doi.org/10.1016/j.jenvman.2018.10.091.

[32] Sharma A, Matsumura A. A comparative study on demineralization of coals by acid-washing and solvent-extraction methods for low temperature catalytic coal gasification application. Carbon Resour Convers 2019;2:175–81. https://doi.org/10.1016/j.crcon.2019.09.001.

[33] Qi X, Guo X, Xue L, Zheng C. Effect of iron on Shenfu coal char structure and its influence on gasification reactivity. J Anal Appl Pyrolysis 2014;110:401–7. https://doi.org/10.1016/j.jaap.2014.10.011.

[34] Wang Y, Alsmeyer DC, McCreery RL. Raman Spectroscopy of Carbon Materials: Structural Basis of Observed Spectra. Chem Mater 1990;2:557–63. https://doi.org/10.1021/cm00011a018.

[35] Cuesta A, Dhamelincourt P, Laureyns J, Martínez-Alonso A, Tascón JMD. Raman microprobe studies on carbon materials. Carbon N Y 1994;32:1523–32. https://doi.org/10.1016/0008-6223(94)90148-1.

[36] Sadezky A, Muckenhuber H, Grothe H, Niessner R, Pöschl U. Raman microspectroscopy of soot and related carbonaceous materials: Spectral analysis and structural information. Carbon N Y 2005;43:1731–42. https://doi.org/10.1016/j.carbon.2005.02.018.

Chapter 2: **Gasification kinetics and morphological evolution of low and high-ash char**

Abstract: *The heterogeneity of waste tire pyrolytic char associated with ash composition and distribution is explored to understand the effect of ash on gasification. In this paper, high-ash tire tread (TT) and low-ash sidewall (SW) were separated to study gasification kinetics and the influence of ash on char physico-chemical morphological evolution during CO_2 gasification. Morphological development and characterisation of chars were studied using N_2 adsorption and scanning electron microscopy coupled with energy dispersive X-ray analysis (SEM-EDX). Isothermal gasification kinetics were derived from a thermogravimetric analyser and described by the shrinking core model (SCM), volumetric (VM), random pore model (RPM) and the zeroth order reaction model. The results showed that TT char has silica-based ash clusters which inhibit gasification, particularly at high conversions. Moreover, TT ash suppresses surface area development and forms an inherent skeletal structure that inhibits particle size reduction during the reaction. In contrast, SW char exhibited significant particle size reduction, and surface area development was more pronounced compared to TT char. The surface area for SW char increased until 75% conversion and decreased thereafter, albeit insignificant, while TT char surface area decrease was more pronounced after 50% conversion. All models yielded kinetic parameters of nearly the same magnitude, and the RPM was selected as the most suitable model for TT while SW followed the zeroth order reaction model. The activation energy for TT and SW were found to be 177.1 $kJmol^{-1}$ and 165.6 $kJmol^{-1}$, respectively. The model-free method confirmed the reliability of the results. These findings further confirmed the inhibiting nature of tire ash.*

2.1 Introduction

The advent of the automobile industry coupled with great strides in economic growth triggered a large production of tires from both natural and synthetic rubber; consequently, large volumes of end-of-life tire are generated only to meet inadequate tire disposal systems [1]. Traditionally, waste tires are disposed of in landfills or simply controlled burning, which exacerbate an already dire environmental concern, the former consumes more volume than most waste and contributes to the shortening of landfill life while the latter disperses particulate matter and noxious gases into the atmosphere [2,3]. In keeping with green waste management policies, thermal disposal methods such as pyrolysis and gasification have received much attention [2,4]. Chief among the advantages of these technologies is the ability to recover tire components from pyrolysis or gasification and energy harvesting by controlled combustion of products while posing little to no harm to the environment.

Waste tire can be pyrolysed into gas, oil and char, which require further upgrading before use as a fuel or chemical industry feedstock material because products are usually laden with sulphur, an objectionable fuel component [5]. The scope of this work is restricted to pyrolytic char, which is a high calorific carbon-rich solid residue. Apart from its high ash and sulphur content, it is a good candidate for energy harvesting through gasification [6]. Gasification is the thermochemical conversion of a carbon-based material into a combustible gas. The gasification process occurs in a series of steps, and these are initiated by rapid devolatilisation which occurs in milliseconds, followed by a reaction region within which simultaneous pyrolysis and gasification occurs and terminates after protracted gasification of the nascent char. The gasification step has the slowest reaction rate; therefore, it is considered the rate-determining step and is the basis of reaction kinetics studies [7].

As a prerequisite for new or unconventional carbon source application such as tire char, feedstock performance evaluation under conditions of industrial applicability and interest are key. The importance of fundamental studies on gasification characteristics, which include and are not limited to reaction kinetics, co-gasification characteristics, char-ash/slag transformation and interactions cannot be overemphasised. These contribute to assessing feedstock applicability, precise reactor design, optimal reactor operation and also provide a theoretical basis for simulation [8].

Several researchers have established that there is potential for gasification of high calorific friable pyrolytic tire char individually and as an adjunct fuel source in coal-based technology such as fluidised and entrained flow gasifiers [4]. Only a limited number of pyrolytic tire char

gasification kinetics research has been reported [9–15]. Lahijani and colleagues [9,10] mainly researched on tire/biomass co-gasification kinetics while others focused more on the pyrolytic char gasification kinetics, wherein carbon activation and syngas production are the main objectives. It is well established that tire char contains high ash content (2-20 wt.%). It is reasonable to expect ash to have a significant effect on the physicochemical evolution of char during gasification, the effect thereof, however, is dependent on the amount, nature and distribution of ash in the char particles. The possible effects of ash on tire char gasification have not received much attention compared to coal.

Several researchers [16–18], however, have reported on the catalytic effect of alkaline and alkaline earth metals (AAEMs) during coal gasification. The mechanism of catalysis involves suppression of the degree of char graphitization [19] and formation of active sites via AAEMs and oxygen functional group interaction during gasification [20]. Some researchers have reported on the negative effect of inert and or acidic ash, and these include; inhibition of surface area development [21], ash encapsulation of unreacted carbon [22–24] and acting as sites for AAEMs deactivation [25,26] at elevated temperatures. The role of ash in tire char gasification is, therefore, a subject of interest if tire char gasification is to be understood and effectively exploited.

Waste tires can be divided into two main parts (SW and TT); this results in two distinct chars that can be used as a basis for comparison. TT is the reinforced inflexible rubber on the tire circumference that makes contact with the ground. The SW, on the other hand, does not make contact with the road. It is a relatively flexible rubber whose primary purpose is containing air. Wang et al. [24] reported on the dissimilarity between SW and TT char ash composition; ash content was 2% and 18% respectively. This heterogeneity has not been accounted for in previous gasification kinetic characterisation studies. Thus the authors of this paper were technically impugned to investigate and report the kinetics of separate TT and SW char as well as the possible effects of ash on morphological evolution during gasification.

There is no criterion consensus on the kinetic analysis of gasification experimental data [27], such that there is a plethora of reports with seemingly contradicting results particularly in tire gasification [10,14,15]. The most common criterion is comparing single-step reaction models strictly on a statistical basis and adopting that which yields the highest coefficient of determination (R^2) [28]. A high coefficient of determination does not necessarily translate to a correct interpretation of the reaction mechanism. The most-reported model is the random pore

model, which can predict the maximum rate, however Gomez et al. [27] demonstrated that the maximum rate is an artefact of experimental design, particularly gas switching during thermogravimetric analysis (TGA). Tanner and Bhattacharya [28] showed that when the maximum rate was eliminated, three basic models (random pore model (RPM), volumetric model (VM) and shrinking core model (SCM)) showed high similarity of fit, consequently the appropriate model was chosen based on the model`s theoretical sophistication. In some cases, the RPM was reported to underestimate the kinetic parameters although the fit was good [15]. The reasons above highlight the uncertainty associated with the accuracy and consistency of findings in the literature, therefore it is imperative to test the consistency of results. Gomez and Mahinpey [27] proposed the determination of kinetic parameters by an isoconversional method, which is independent of restrictions imposed by any particular conventional solid-gas reaction model. Kinetic parameters determined by this model-free method are a good yardstick to evaluate the consistency of results obtained from model-dependent approaches. The discussion above motivated the approach adopted in this work to determine the reaction kinetics of waste pyrolytic tire char. In this chapter, fundamental kinetic characterisation of high-ash and low-ash tire char in the chemical reaction controlled temperature range was evaluated using three basic gas-solid reaction models, and the resultant kinetic parameters were tested for consistency by a free-model approach. Char morphological evolution during gasification is reported and employed as an additional criterion for reaction model discrimination. The effect of ash composition on the physico-chemical evolution is also presented by comparing low and high-ash pyrolytic tire semichars.

2.2 Materials and methods

2.2.1 Sample preparation

Dunlop end-of-life waste tire was used in this study because it is the most common tire brand in Zimbabwe. The tire was separated into TT and SW. Samples were reduced to small shreds, and all reinforcement wires and textiles were excluded from the samples. The resultant tire shreds were further washed in distilled water to remove any impurities which may compromise the accuracy of char characterisation study. Pyrolysis experiments were carried out in a tubular electric glass drop-tube reactor, a detailed description of the equipment is reported elsewhere [29]. 80 g of each sample was introduced separately into a reactor operated 1000°C and residence time of 30 minutes was adopted to ensure all volatile matter was expelled from the samples. An inert atmosphere was maintained in the reactor by injecting N_2 gas at a flow rate

of 200 ml/min. The nascent chars were then pulverised, sieved to a different size ranges (~50 µm, ~100 µm, ~150 µm and 200 µm) and stored in sealed containers.

2.2.2 Analytical methods

The proximate analysis of all samples was carried out using the TGA analyser, (Shimadzu DTG-60H with thermal analyzer TA-60WS, Japan). The ultimate analysis of the char samples was performed using the Vario Micro Cube Elemental Analyser (Elementary, Japan). The results are shown in Table 2-1.

Table 2-1**.** Properties of samples (dry basis)

Sample		Proximate analysis, wt%			Ultimate analysis, wt%			
	Moisture	C_{fix}	VM	Ash	C	H	N	S
TT Char	5.32	74.09	-	20.60	72.97	1.15	0.41	2.15
SW Char	3.62	91.14	-	5.23	90.72	0.76	0.47	2.23

Note: VM-volatile matter; C_{fix}-fixed carbon calculated by difference

The ash composition was analysed by energy dispersive X-ray fluorescence spectrometer (XRF: S2 Ranger/LE, Bruker AXS, Germany) and the results are presented in Table 2-2. The characteristic char analysis was done in duplicates, and relative error data obtained after multiple experiments were less than 3%.

Table 2-2. Ash composition of raw materials

Sample	SiO_2	Al_2O_3	Fe_2O_3	CaO	MgO	SO_3	ZnO	K_2O	Na_2O
TT Ash	27.67	6.86	5.60	10.66	2.49	31.42	10.43	1.62	1.73
SW Ash	9.18	6.12	3.06	7.65	0.77	39.78	29.07	0.31	3.06

Scanning electron microscopy (SEM: JSM-6610LA, JEOL Ltd., Japan) was used to observe the char samples` morphological surface characteristics. Char samples were secured to specimen holders by a double-sided adhesive carbon tape. The samples thus furnished were then coated with Pt-Pd using a sputter coating device (MSP-1S, Vacuum device Ltd., Japan) to eliminate electrostatic charge-up, which compromises the integrity of the sample. Energy-dispersive X-ray analysis coupled with SEM (SEM-EDX: EX-94300S4L1Q, JEOL Ltd., Japan) was used for elemental semi-quantification of various components in the char, platinum and palladium were excluded from the mapping to avoid overestimation. In this study, at least

100 particles for each experimental sample were analyzed, and a mean value was considered representative. The char surface area was measured using an ASAP 2020 analyser by N_2 gas adsorption method at 77.15K for pores with a diameter range from 2 nm to 200 nm. The Brunauer–Emmet–Teller (BET) model was used to calculate the specific surface areas of the samples.

2.2.3 Char-CO_2 gasification experiments in TGA

Isothermal CO_2-gasification rate of reaction of char samples was measured by TGA within a temperature range of 850 and 925°C, to ensure that only kinetic parameters under chemical reaction control regime were determined [10,12]. All experiments were carried out at atmospheric pressure and 100% CO_2 concentration. Gasification reactions in TGA are strongly influenced by gas diffusion effects which emanate from experimental design, and these were systematically eliminated to obtain reliable results. Gas flow rate optimisation at a worst-case scenario was carried out by considering three flowrates (100 mL/min, 150 mL/min and 200 mL/min) at 925°C and on ~200µm particles. The conversion time profiles were coincident, indicating that gas flow within this range exerted negligible external diffusion resistance. A gas flow rate of 150 mL/min was then selected in this study according to three criteria. Firstly, this flow rate is high enough to reduce gas equilibration time after switching from N_2 to CO_2; as a result, the false maximum reaction rate induced by gas switching is negligibly visible [28]. Secondly, the adopted flow rate eliminated external diffusion effects associated with particle size and distribution of the test samples [7] and finally, the gas flow was adequate to maintain a constant reaction atmosphere in the TGA by rapid purging of product gas which is known to affect the gasification reaction [30]. A series of experimental runs at different size ranges (~50 µm, ~100 µm, ~150 µm and 200 µm) was carried out to determine the particle size range below which pore diffusion is negligible. It was found that for particles of ≤100 µm size range the effect of size on gasification could be considered insignificant. As a result, the ~100 µm particles were used in this study. As a measure to further minimise systematic diffusion caused by poor char loading practise [28], a monolayer of 10 ± 0.5 mg of sample was loaded into an alumina crucible almost half-filled with silica sand, in which case gas-solid interaction is promoted. A crucible measuring 15 mm in diameter and 2.0 mm in wall-height was selected for gasification experiments to eliminate diffusion effects associated with char mass and bed depth [27,30]. The typical experimental procedure followed is: Char samples were charged in the crucible, heated to the target temperature at a 25°C/min under N_2 gas atmosphere (80 mL/min) and held for 5 minutes to ensure temperature equilibration. The N_2 gas was then

switched to high purity CO_2 gas (150 mL/min), and gasification initiated. All experiments were done in duplicates to test for repeatability, and the relative error data obtained after multiple experiments was less than 3%. The semichars were prepared by interrupting gasification TGA tests at times corresponding to different conversions, this was achieved by switching CO_2 flow for N_2 gas to stop the reaction. After cooling to ambient temperature, the samples were collected and stored for further analysis.

2.2.4 Kinetic model discrimination

The original thermogravimetric data was normalised on an ash-free basis according to the following equation, which defines conversion at any time:

$$x = \frac{m_0 - m_t}{m_0 - m_a} \tag{2-1}$$

where m_0 is the initial mass of samples, m_t is the instantaneous sample mass at any time t and m_a is the mass of ash.

Normalised data were modelled according to the four basic models, namely; VM, SCM, RPM, and the zeroth order reaction model. The criterion of comparison between reaction models based on three complementary steps. The accuracy of correlation between experimental data and the single-step chemical reaction models is compared and based on the key statistical indicator R^2. The precision and appropriateness of the models is determined by comparing model results to those obtained from the free model approach (FMA) [27]. Char surface morphological transformations observed during gasification are used as adjunct confirmation of appropriateness of the models.

2.3 Results and discussion

2.3.1 Char characterisation

Pyrolytic tire char ash can be classified into inert ash and active ash. Inert ash includes chemical species such as SiO_2 and Al_2O_3, and these species have no active role in carbon gasification, but rather, they are reported to deactivate AAEMs through deactivation reactions [31–33]. Active ash species are any components other than inert ash species. The active ash of tire char can further be divided into two classes. One class is known to reduce the gasification reaction activation energy, AAEM and Fe [34] are typical examples, this class is referred to as catalytic ash in this work. The second class is ZnS, the role of this species is not fully known and as a

result it is separated from the catalytic ash in the ternary diagrams. Table 1-1 and Table 2-1 show that TT char has almost four times as much ash as SW char and the ash compositions thereof are distinct. Tire tread ash is mainly composed of SiO_2 and SO_3, while ZnO and SO_3 are the main components of SW ash.

The physical and chemical morphological evolution of char during gasification is mostly influenced by the nature and amount of inherent ash, and high inert ash content hinders pore char development as a result available reaction surface area is diminished.[23] Due to the high ash content in TT char, observations show that there exist ash clusters that cover a considerable area on the surface of the char, and it can be speculated that these clusters can also be found in the bulk of the carbon matrix. Figure 2-1 shows typical SEM images of TT and SW char, and the rectangular perimeter highlights an ash cluster. The corresponding EDX analysis is shown in Table 2-3. Multiple equal areas measuring 400 μm^2 on at least 100 particles were chosen randomly and mapped out with a bias on characterising ash clusters in order to establish the extent to which carbon encapsulation.

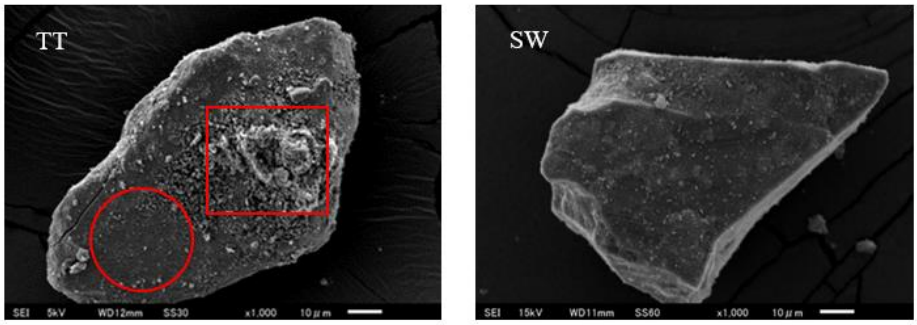

Figure 2-1. SEM images of different chars

Table 2-3. EDX analysis of TT char (ash: rectangular perimeter; carbon matrix: circular perimeter)

	C	O	S	Zn	Si	Al	Ca	Na	Fe
Carbon matrix	81.37	13.61	1.02	2.2	0.26	0.43	0.79	0.21	0.11
Ash	9.32	36.91	4.06	6.12	35.01	2.24	1.35	1.78	3.21

The composition of ash was measured using SEM-EDX. The working principle of the SEM-EDX analyser is that it detects reflected X-ray from a few micrometres below particle surface, therefore by strict description, elemental data includes both surface and intra-structure information. This analysis was exploited to gain insights on the carbon distribution within ash agglomerates.Ternary plots presenting the Carbon, Active ash, Inert ash distribution were prepared as shown in Figure 2-2. Secondary ternary plots were plotted for easy visualisation of

ash composition, three classes namely; Catalytic ash, inert ash and (Zn/S). Zn and S were put in the same category because these elements may exist in the form ZnS [35] and their effect on gasification is not yet well established. Figure 2-2 c and d show the compositional distribution of carbon in SW, the char surface consists of a high percentage of carbon, and this implies that carbon is not encapsulated or covered in ash. This analysis confirms the absence of ash clusters, which was expected considering the low ash percentage of SW char. The SW ash composition has less than 10% Si and Al, it is reasonable to expect SW ash to have active catalytic performance given that chemical deactivation reaction with Si is inhibited by low Si concentration. Figure 2-2 a and b show that TT ash clusters have a low percentage of carbon.

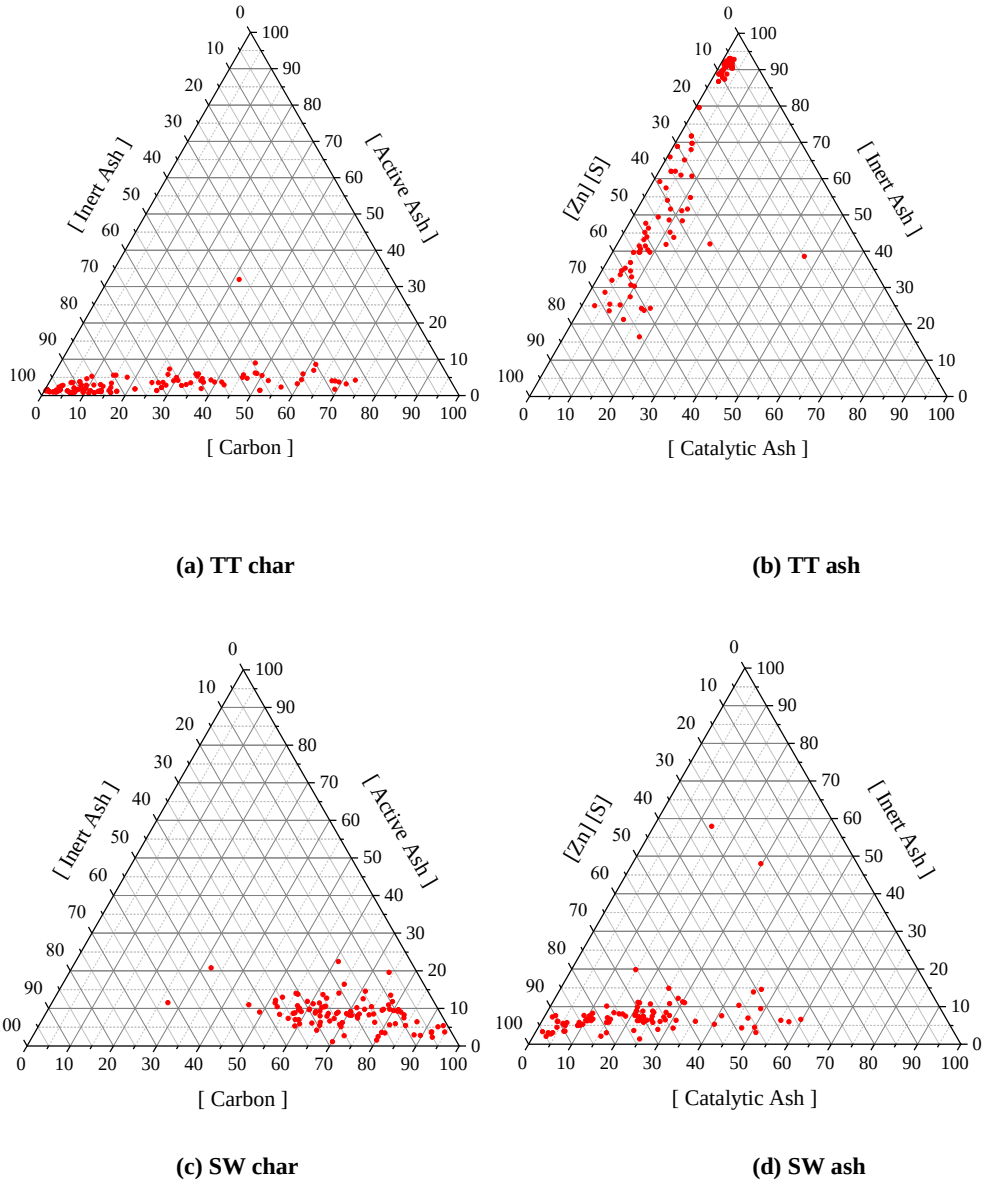

Figure 2-2. The compositional distribution of char and ash in ash clusters: (a) Tire tread char, (b) Tire tread ash, (c) Sidewall char and (d) Sidewall ash

The implication is that ash clusters not only encapsulate carbon but also covers the char carbon matrix. It is speculated that during gasification these sites are capable of impeding gas flow into the bulk of the carbon matrix and as a consequence, inhibition is expected, especially at high conversion if the ash is non-flaking. Coupled with a significant percentage of SiO_2 and Al_2O_3, the catalytic capacity of AAEM is likely to be diminished with reaction progress. On the contrary, SW char inhibition will be insignificant compared to TT char given the low ash content of SW char. The SiO_2 and Al_2O_3 to AAEM ratios are very small, thus catalytic deactivation reactions are expected not to be on a scale that poses a significant adverse effect on the AAEM catalytic capacity. The ternary plots also show that the ash components are not uniformly distributed in the TT char; therefore, it is reasonable to infer that pyrolysis promotes agglomeration or lumping of ash components.

2.3.2 Model fitting

Processed conversion-time data is shown in Figure 2-3. The conversion-time profiles are different. SW char shows an almost linear relationship without any indication of pronounced inhibition effects even at high conversion. TT char exhibits a protracted time delay in reaching completion, which is characteristic of inhibition effects caused by mainly by ash accumulation or intraparticle diffusion [36]. Based on the reactivity curves and proximate analysis, it is reasoned that inhibition is as a result of high inherent char ash content in TT. As a result, the reaction time for TT char is longer than SW char.

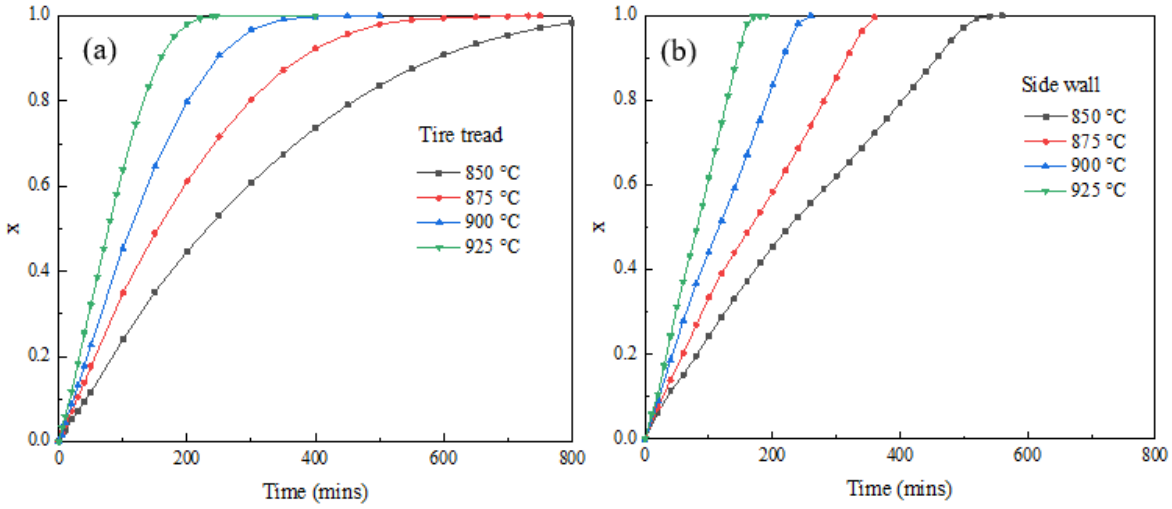

Figure 2-3. Gasification reactivity curves of (a) Tire tread and (b) Sidewall

There are three basic reaction models by which solid-gas reactions are usually described. The difference between these models is a consequence of the fundamental assumptions made in formulating a mathematical presentation of chemical reactions.

The volumetric model assumes that the gas has unimpeded access in and around a particle such that the chemical reaction simultaneously occurs throughout the particle and is described by the equation:

$$\frac{dx}{dt} = k(1-x) \tag{2-2}$$

where dx/dt is the reaction rate, k is the gasification reaction rate, and x is the conversion.

The shrinking core model assumes that the chemical reaction is initiated on the outermost surface of a spherical particle, and the reaction zone progresses towards the centre, leaving behind non-flaking ash. The mathematical presentation of the shrinking core model [37] is shown in the equation:

$$\frac{dx}{dt} = k(1-x)^{\frac{2}{3}} \tag{2-3}$$

The random pore model accounts for the structural evolution of the char as the chemical reaction proceeds, in particular, the growth and coalescence of pores [38]. The commonly used simplified form of the random pore model is shown in the following equation.

$$\frac{dx}{dt} = k(1-x)\sqrt{1-\varphi \ln(1-x)} \tag{2-4}$$

where φ is a dimensionless structural parameter indicating the pore structure of pristine char. This parameter was treated as a fitting parameter determined by regression optimisation.

A summary of the modelling results is shown in Table 2-4; it is shown that all models represent a high similarity of fit. However, the highest correlations are in the SCM and RPM.

Table 2-4. Comparison of fits obtained from different models

		SCM		RPM			VM	
Sample	Temp(°C)	k_0 (min^{-1})	R^2	k_0 (min^{-1})	φ	R^2	k_0(min^{-1})	R^2
TT	850	9.02×10^{-4}	0.997	2.34×10^{-3}	2.15	0.999	3.39×10^{-3}	0.982
	875	1.38×10^{-3}	0.990	3.58×10^{-3}	2.09	0.995	5.23×10^{-3}	0.980
	900	2.01×10^{-3}	0.983	5.19×10^{-3}	2.17	0.990	7.55×10^{-3}	0.964
	925	3.00×10^{-3}	0.972	7.73×10^{-3}	2.21	0.992	1.11×10^{-2}	0.946
SW	850	1.01×10^{-3}	0.976	1.93×10^{-3}	6.12	0.986	3.65×10^{-3}	0.939
	875	1.41×10^{-3}	0.972	2.71×10^{-3}	6.03	0.984	5.01×10^{-3}	0.934
	900	2.05×10^{-3}	0.965	3.93×10^{-3}	6.31	0.984	7.30×10^{-3}	0.926
	925	3.03×10^{-3}	0.957	5.77×10^{-3}	6.11	0.979	1.09×10^{-2}	0.907

The experimental conversion curves and corresponding model fits are shown in Figure 2-4. The RPM has the highest correlation; similar results of nearly perfect modelling were reported by Murillo et al. [12]. There is no consensus on the model that best describes pyrolytic tire char conversion, and contradictory findings were published by Lee and Kim [14], they reported that the modified volumetric model was the most appropriate. Recently, Preciado-Hernandez et al. [15] reported that the volumetric model fit experimental data well. This could be an artefact of the characteristics of tire char from different makes, the thermal history of the char and the type of experimental equipment used. The high correlation of all models considered in this paper also supports the existing contradictions that are present in literature, any one of these models results in nearly the same kinetic parameters, (see Table 2-5).

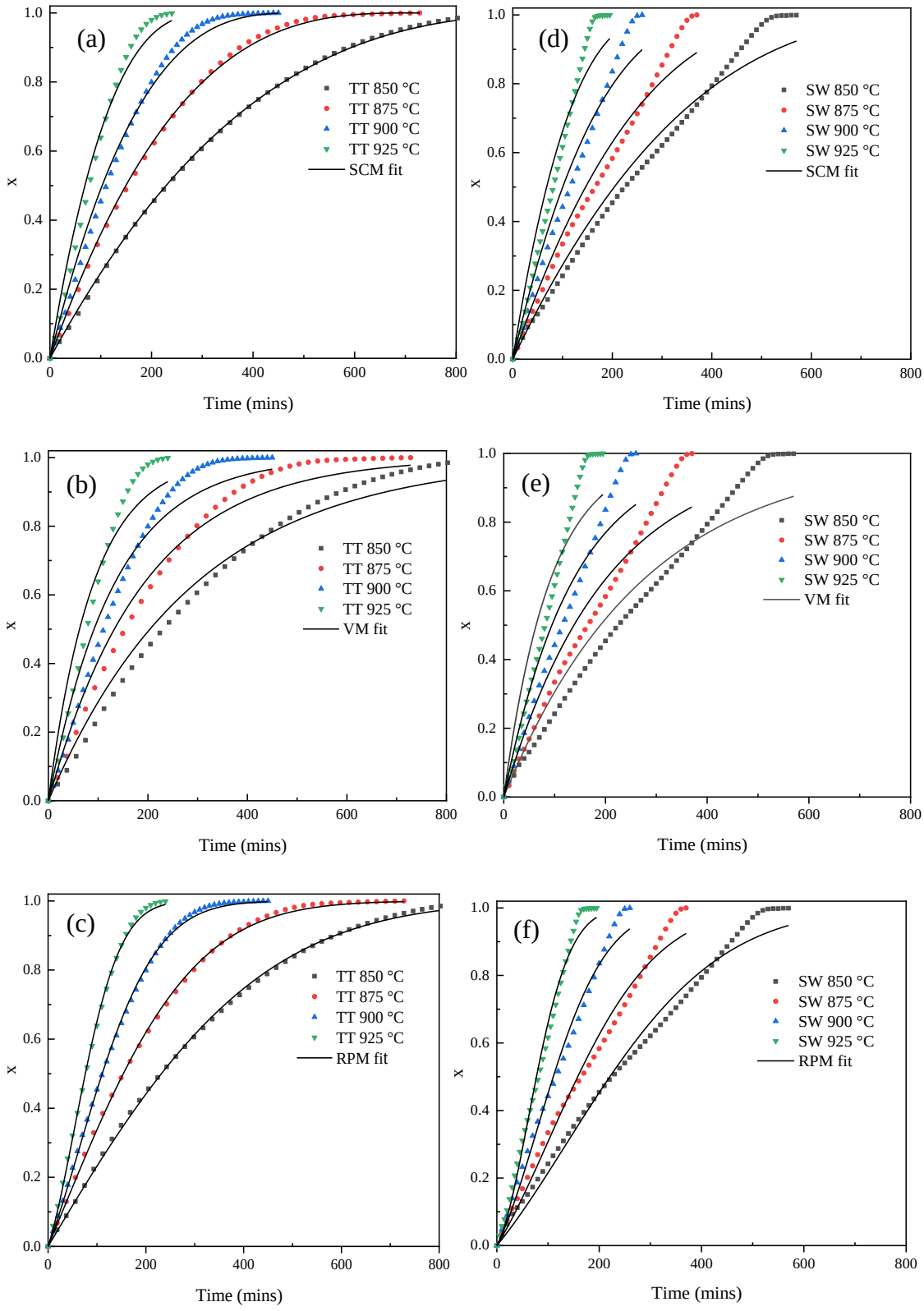

Figure 2-4. Modelling results: (a) Tired tread (SCM), (b) Tire tread (VM), (c) Tire tread (RPM), (d) Sidewall (SCM), (e) Sidewall (VM) and (f) Sidewall (RPM)

Selecting the appropriate model based solely on their coefficient of determination and degree of theoretical sophistication is associated with a high degree of uncertainty, in this case;

therefore, it is imperative to probe the morphological evolution characteristics of char as supporting criterion for model discrimination.

The Arrhenius equation that describes the effect of temperature on the rate of reaction is used to determine kinetic properties, and the equation is shown below:

$$k = k_0 e^{-\left(\frac{E_A}{RT}\right)} \tag{2-5}$$

where k_0 is the pre-exponential factor, E_A represents the activated energy and R is the universal gas constant. The activation energy and the pre-exponential factor was calculated by determining the gradient and y-intercept of Arrhenius plots shown in Figure 2-5, according to the following equation below:

$$\ln k = \ln k_0 + \left(\frac{-E_A}{R}\right)\frac{1}{T} \tag{2-6}$$

The temperature range adopted for experiments is in the chemical reaction regime zone because there is no break in linearity in the Arrhenius plots. The derived kinetic parameters are summarised in Table 2-5.

Table 2-5. Comparison of kinetic parameters of gasification obtained from different models

	SCM		RPM		VM	
Sample	E (kJ/mol)	k_0(min^{-1})	E (kJ/mol)	k_0 (min^{-1})	E ($kJmol^{-1}$)	k_0(min^{-1})
TT	178.2	1.75×10^5	177.1	4.03×10^5	175.4	4.39×10^5
SW	164.1	4.23×10^4	163.5	7.64×10^4	163.6	1.45×10^5

All three models produced similar results, in terms of kinetic parameters, as can be seen by the parallel Arrhenius plots. From these results it is difficult to ascertain which model is most appropriate since the models have a high coefficient of determination; therefore, morphological evolution during gasification is explored to aid selection.

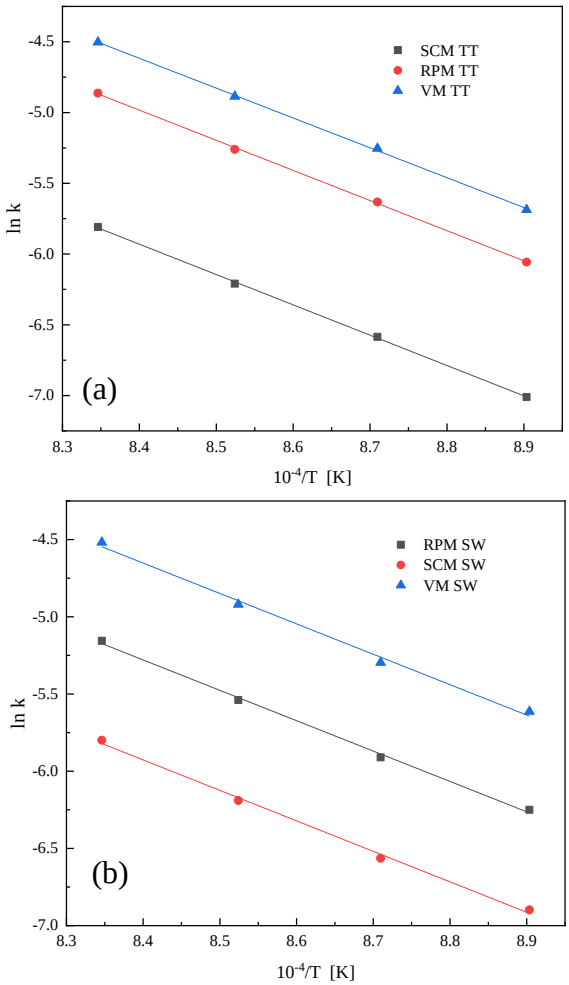

Figure 2-5. Arrhenius plots showing the temperature dependence of CO_2 gasification for (a) Tire tread and (b) Sidewall

The linear gasification profile of the sidewall suggests a constant rate of conversation, which is not accounted for in the classic solid-gas models; however, this mechanism can be modelled using zeroth-order kinetics. Zeroth-order linear fits are shown in Figure 2-6; the correlation of fits is better than that of the three classic models.

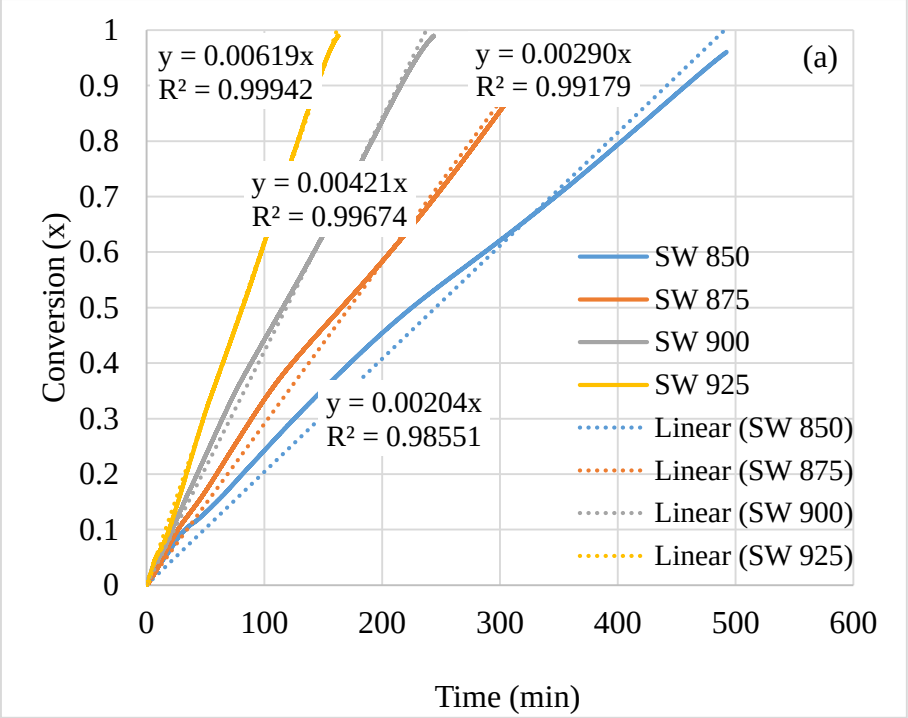

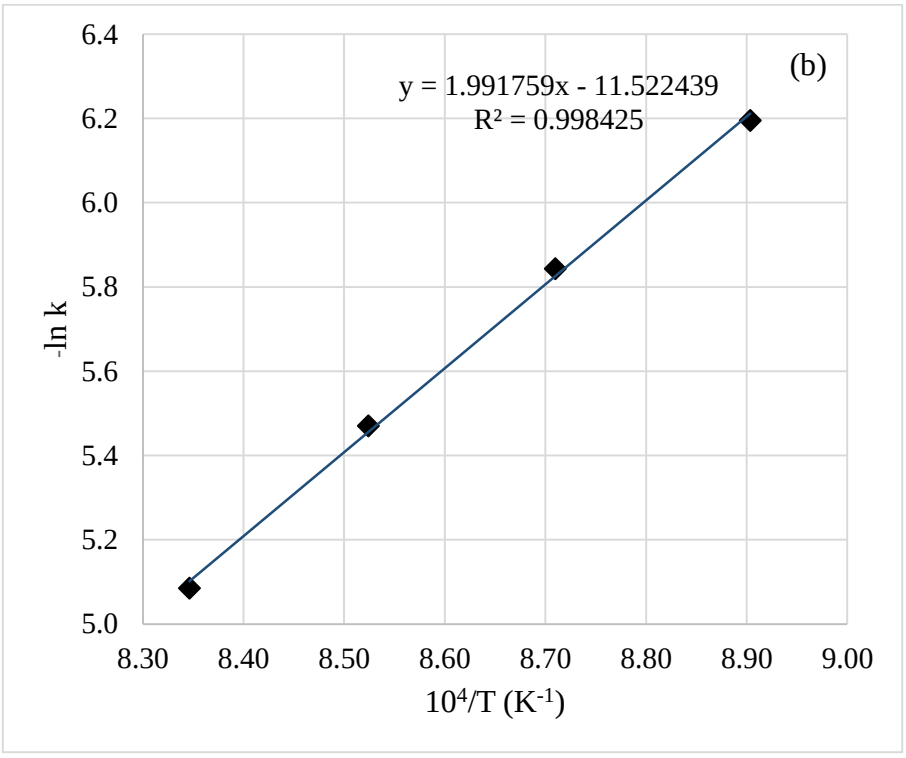

Figure 2-6. (a) Zeroth law fitting and (b) Arrhenius linear plot

Therefore, sidewall gasification is described by the zeroth-order mechanism, and the activation energy calculated from the Arrhenius plot (Figure 2-6) is 165.6 kJ/mol while the pre exponential factor is 1.01×10^{5} min^{-1}. It should be noted that the magnitude of activation energy is similar to those obtained from the classic model.

2.3.3 Model consistency evaluation

It is noted from the literature that some kinetic parameters obtained from conventional models discussed above can be inconsistent, thus resulting in erroneous interpretation of reaction mechanism; therefore, it is necessary to use a method that is independent of these models as a yardstick. The consistency of the kinetic parameters obtained from the single-step reaction models is assessed according to the isoconversion or model-free method [27]. This method allows for the calculation of the activation energy without the need for mathematically describing the physico-chemical property of the chars. The model-free method is derived in an ensuing manner.

The general rate law for char-gasification, under chemical reaction regime and constant pressure, is given by

$$r = \frac{dx}{dt} = k(T) f(x) \tag{2-7}$$

where $f(x)$ represents an appropriate reaction model as a function of conversion.

Equation 2-7 can be solved by separating variables and integrating the equation to yield,

$$\int_0^x \frac{dx}{f(x)} = G(x) = k_x(T) t_x(T) \tag{2-8}$$

where k_x and t_x are the rate constant and residence time (min) at a particular conversion x, and all are expressed as a function of temperature. By combining the general rate law and the Arrhenius equation, on solving the formal solution can be reduced to the following expression:

$$\ln[t_x(T)] = \alpha + \frac{E_A}{RT} \tag{2-9}$$

where $\alpha = \ln G(x) - lnk_0$, is a constant for a particular conversion.

The activation energy for SW and TT char gasification, calculated from the slope of $\ln(t_x)$ vs $1/T$ plots are shown in Figure 2-7. The isoconversional procedure was applied to four particular conversions ranging from 25-90%. The gradients of the plots have a linear trend that does not change significantly with conversion. The results obtained from all models are similar to those obtained at $x = 0.75$ by the isoconversional method, hence the model results are considered reliable. The same criterion was used by Gomez and Mahinpey [27], they reported that results activation energy calculated at 80% conversion represented the entirety of the gasification reaction. Activation energies determined at different conversion levels must be of

similar magnitude if and only if the reaction follows a single pathway and the char is homogenous, however results show that activation energy increases with conversion. An ideal char retains its catalytic activity as the reaction progresses, such that the activation energy is expected to remain constant in the entre conversion range; however, in reality, there is deviation. The change in activation energy for TT and SW char from 25 to 90% conversion is 26.3% and 19.5% respectively. The gasification of carbonaceous material is associated with evolution of physico-chemical structure [39,40], catalyst deactivation or loss [33], intraparticle diffusion at high conversions and thermal annealing [41–44]. The increase in activation energy observed in this study is attributed to these interrelated factors.

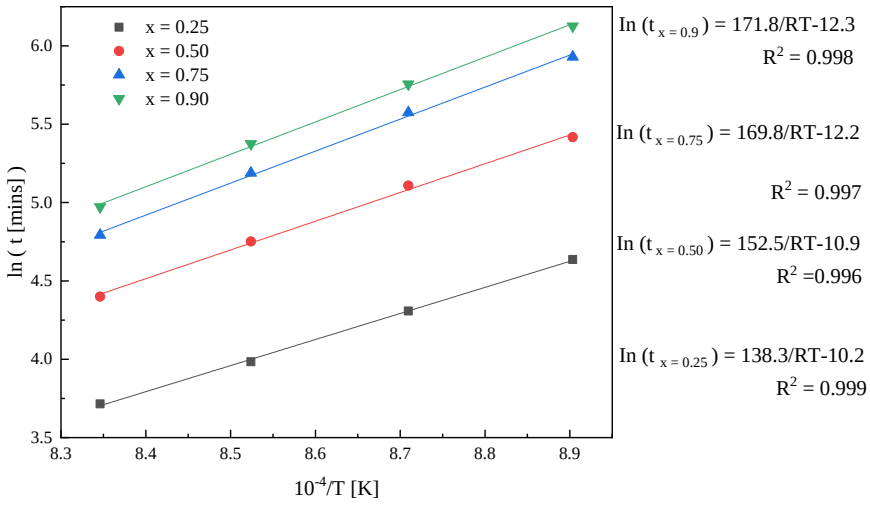

(a) SW char

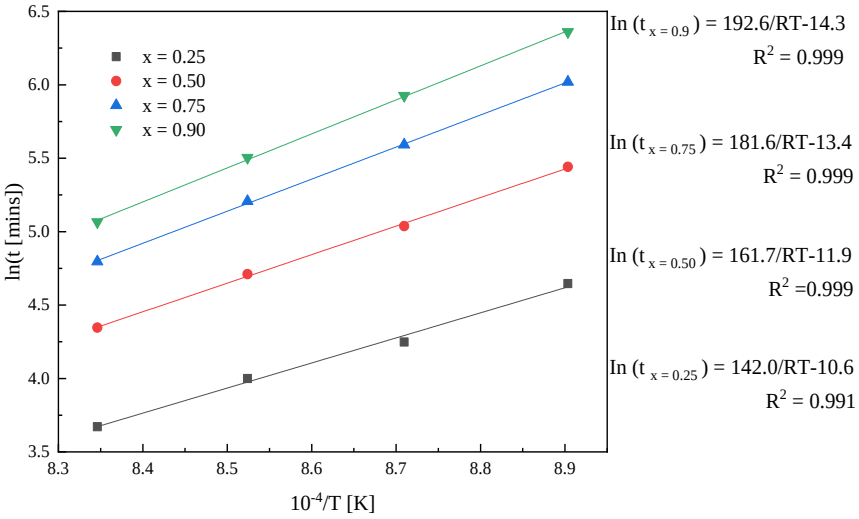

(b) TT char

Figure 2-7. Logarithm of time versus reciprocal of temperature for (a) Sidewall and (b) Tiretread char

The change in activation energy with reaction progress may also be described by considering the precise composition of tire pyrolytic char. Pyrolytic tire char is a composite of carbonised rubber deposits and inorganic species lodged in and around a mesoporous carbon black structure [45]. By virtue of their formation mechanism, the polymerised hydrocarbon deposits are disorganised. As a result, they react readily compared to carbon black, which has a behaviour akin to an inert material during gasification [12]. If this is so, this implies that pyrolytic tire char, regardless of origin, has lower initial activation energy. Then, after preferential consumption of active sites in the form of deposits, carbon black commences reaction, at much higher activation energy. By comparing the trend of activation energy (E_A) variation with conversion, the postulation made agrees well with observations. The difference between E_A of TT and SW at 25% conversion is an insignificant 3.7 kJ/mol. Moreover, the E_A difference at 50%,75% and 90% conversion is 9.2, 11.8 and 20.8 kJ/mol, respectively. In all cases, the E_A of TT is larger than that of SW, and this trend is attributed to the effect of high ash content on gasification. It is reasoned that as the reaction progresses, ash to carbon ratio increases, such that ash accumulation blocks pores or encapsulates the carbon matrix. Consequently, ash clusters impede the gasifying agent from accessing active sites and simultaneously hinders the escape of gasification products. These inferences are supported by the speculations made about the role of ash agglomerates on gasification. A significant change in catalyst activity in TT char can be accounted for by the high content of silica, which promotes active catalyst deactivation. For SW char it is reasonable to infer that catalytic activity is lost when catalytic species are volatilised and lost during gasification. The inference can be supported and corroborated by SEM-EDX results shown in Table 2-7 and Table 2-8.

2.3.4 Variation of surface area

The measured Brunauer–Emmet–Teller surface area (S_{BET}) of pristine TT and SW char by the N_2 adsorption technique is 112 m^2g^{-1} and 42 m^2g^{-1} with a calculated mesoporous ratio of 67.51% and 62.06 %, respectively. These results are similar to those reported by Wang et al. [24], they reported S_{BET} of 121 m^2g^{-1} and 44 m^2g^{-1} for TT and SW char, respectively. Table 2-6 shows the variation of S_{BET} with conversion for TT and SW during gasification at 925°C only. It is observed that surface area increases significantly from the onset till 50% conversion for both chars. Beyond which, both samples exhibit a drop in the rate of surface area development. The maximum surface area for TT lies between 50 and 75% conversion, and similar trends were reported other researchers [13,15,46,47]. López et al. [47] and Zabaniotou et al. [46] reported that maximum surface area occurred at 60% and 60-65% conversion when

the activation temperature was 950°C and 970°C respectively. The degree of surface area growth in SW is higher than that of TT, and this is possibly a result of ash which has been reported to hinder pore growth [39]. The mesoporous nature of the chars may have a negative effect on the extent of surface area growth since mesoporous growth inevitably leads to early of pores merging into macropores of lower surface area.

Table 2-6. Variation of surface area during gasification

Conversion	SA (m^2/g)	
	TT char	SW char
0.00	111.82	41.94
0.25	160.30	71.30
0.50	360.68	161.05
0.75	339.84	171.95
0.90	200.38	157.28

It is inferred within reason that the decrease in surface area for TT is a composite consequence of pore coalescence, carbon consumption, and ash accumulation within already developed pores. In the case of SW, S_{BET} increases until 75% conversion, overall, it maintains a high surface area in the whole conversion spectrum, this correlates well with the nearly linear conversion profile shown in Figure 2-3. These findings suggest that char physical structure development is inhibited by high ash content especially at high conversion because TT char has a relatively large S_{BET} drop after 75% conversion. The foregoing discussion renders the SCM an inappropriate model to describe tire char gasification mechanism, because it does not account for pore development.

2.3.5 Char morphological evolution during gasification

The char physico-chemical structure evolution was explored, SEM-EDX was used to determine surface morphology and element composition of chars produced at different char gasification conversion. Figure 2-9 shows the surface morphology at different conversions for SW and TT char. Table 2-7 and Table 2-8 show that, in the case of TT char, surface ash accumulates with an increase in conversion, while SW char does not exhibit any significant change in the carbon and ash content. This seemingly unchanging surface composition of SW char can be attributed to the low amount and nature of the ash, it is reasonable to propose that within the considered conversion range, new carbon matrix is exposed as the reaction progresses and ash residue

flakes or is transferred into the gas phase rather than accumulate on the char surface. This speculation is supported by considering one of the most abundant ash component, sulfur. It does not increase with conversion, thus confirming that it does not accumulate on the char surface. Within the aforementioned range, the SEM images in Figure 2-9 suggests that apart from the surface reaction, there is significant internal reaction which results in pore growth. Significant internal structure development was confirmed by surface area evolution trend.

Table 2-7. EDX analysis of SW char at different conversions

Conversion	C	O	S	Zn	Si	Al	Ca	Na	Fe
x = 25	74.77	18.37	2.26	1.72	1.24	0.95	0.25	0.32	0.12
x = 50	71.08	18.61	2.40	2.24	3.38	1.34	0.32	0.42	0.20
x = 75	67.77	21.35	2.34	2.28	3.46	1.40	0.65	0.44	0.34
x = 90	65.00	22.85	2.87	2.77	3.61	1.37	0.61	0.54	0.38

Table 2-8. EDX analysis of TT char with different conversions

Conversion	C	O	S	Zn	Si	Al	Ca	Na	Fe
x = 25	61.51	14.46	4.35	3.41	14.44	0.25	1.05	0.21	0.32
x = 50	42.80	31.80	2.25	2.74	18.05	0.47	1.23	0.22	0.44
x = 75	12.22	40.14	1.51	3.91	38.87	0.49	2.21	0.19	0.46
x = 90	7.47	43.98	1.06	4.12	41.01	0.44	0.98	0.15	0.79

Observations show that TT char surface morphology did not change significantly with reaction progress. However, the inner core was eroded, causing cavities to appear on the char surface. The size of the cavities increased with an increase in conversion. These cavities are as a result of internal reactions which give rise to pore growth and coalescence. This is typical of random pore model which assumes that char particle is composed of cylindrical pores of various sizes. This internal reaction can be seen by the cavities on the char at 50%, as the pores overlap, the cavities become larger and larger as shown by the progressive increase in size at 75% and 90% conversion. The ash agglomerates characterised herein above formed a relatively inactive shell which remained intact in the course of the reaction. Table 2-8 and Figure 2-9 show that TT char ash particles formed an inherent silica-based skeletal structure which remains intact and blanketed the carbon matrix. The observation explains the drastic drop in surface carbon content in TT.

From the findings of the morphological evolution and surface area variation with reaction progress, the mechanism for char evolution can be inferred to occur as follows. The gasifying

agent diffuses into the bulk of the char particles through the pores wherein it reacts at active sites, consequently consuming carbon edges or deformations by the gasification reaction. As the reaction progresses, mesopores grow and intersect to form larger pores and cavities start to appear on the char surfaces.

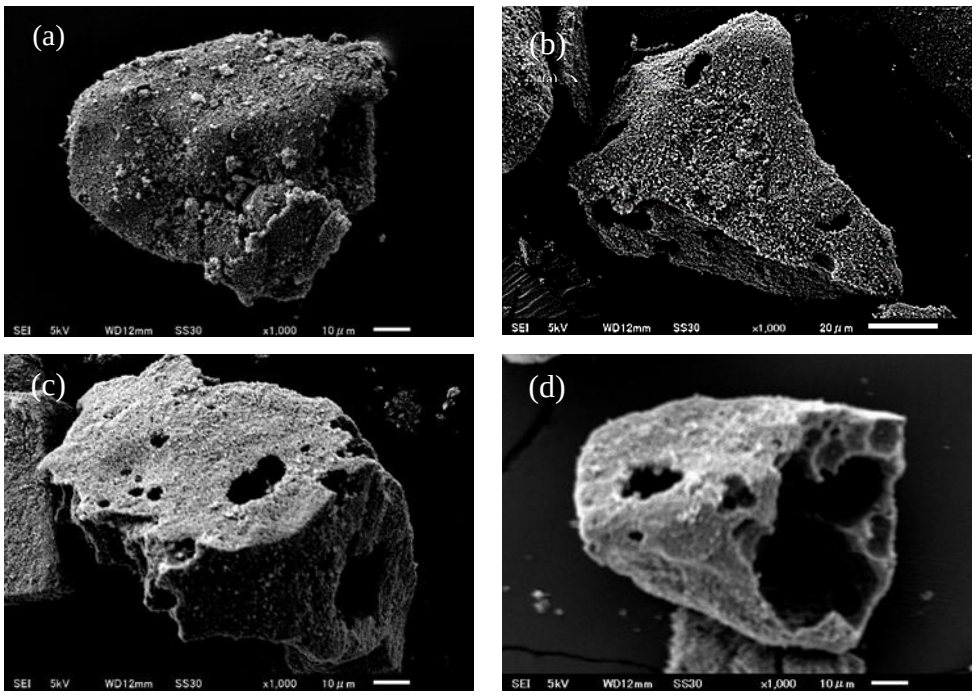

Figure 2-8. SEM images of tire tread char particles at different conversions (a) 25% (b) 50% (c) 75% (d) 90%

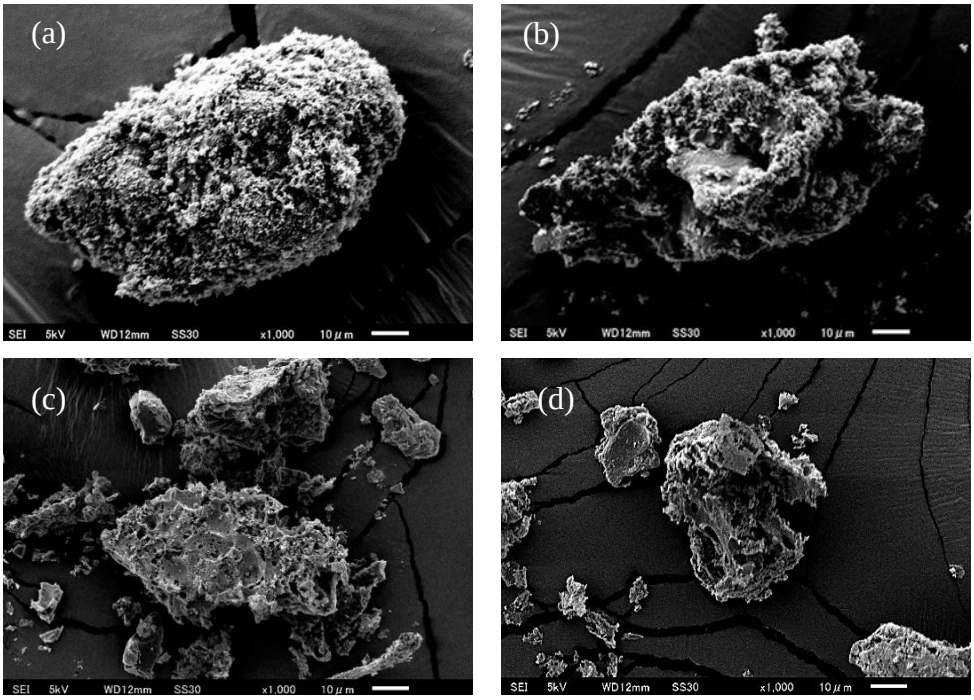

Figure 2-9. SEM images of sidewall char particles at different conversions (a) 25% (b) 50% (c) 75% (d) 90%

The growth of the pores is more pronounced in the first half of the reaction, beyond which, interrelated factors such as ash accumulation in pores, carbon consumption and loss of catalytic activity causes a gradual deceleration in gasification rate. Carbon consumption exposes more ash clusters, which in turn coalesce and produce a coherent silica-based skeletal structure which remains unchanged in size as the reaction progresses. The size thereof depends on the location of the ash clusters within the char. The ash encapsulated carbon becomes difficult to access and consequently a protracted reaction time is observed for TT char. Tire tread char transformation during gasification can therefore be illustrated simply using Figure 2-10, while the transformation for sidewall is shown in Figure 2-11.

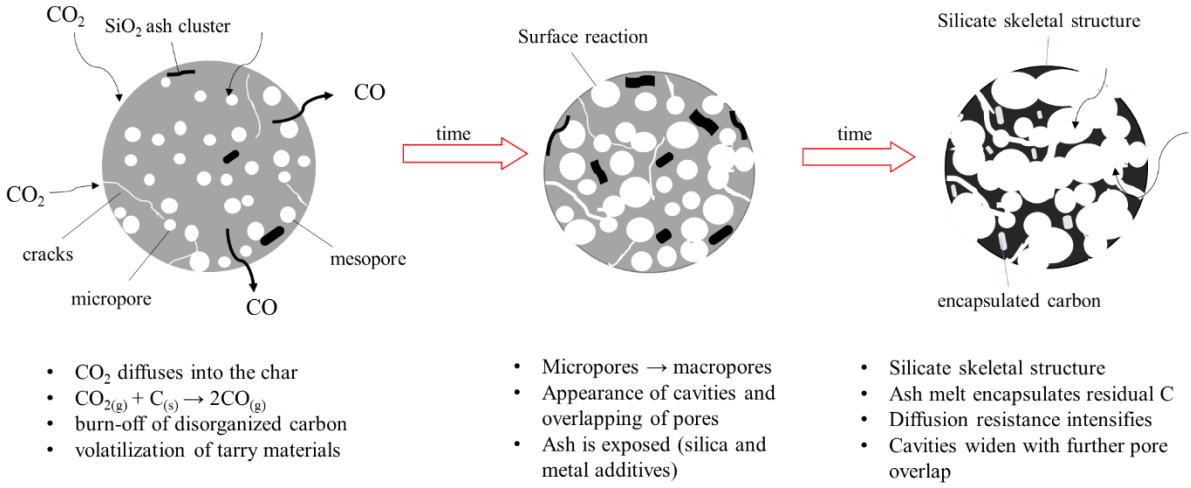

Figure 2-10. Tire tread morphological evolution during gasification

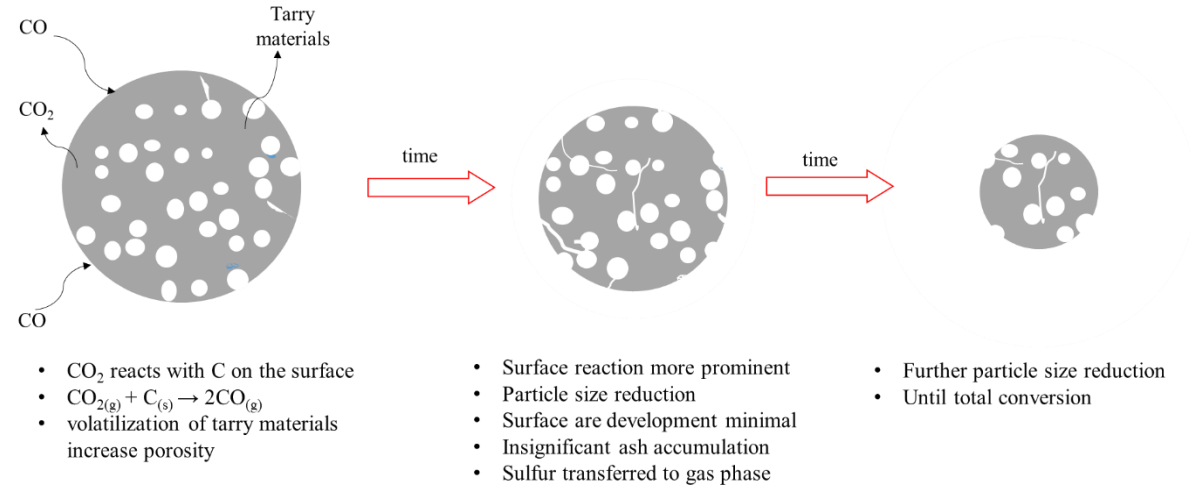

Figure 2-11. Sidewall morphological evolution during gasification

The discussion above justifies the appropriateness of the random pore model in describing the tire gasification, besides the fact that other models have a lower coefficient of determination

do not account for internal structural variations. The erosion of the inner part of the char particle also implies that the SCM is not an appropriate model for tire char gasification. This is further evidence that a high coefficient of determination (R^2) does not necessarily translate to correct interpretation of the reaction mechanism.

3.6 Comparison of SW and TT char gasification reactivity

The reactivity index R_x , is used for the quantitative evaluation of gasification reactivity, according to the literature, it can be calculated at either 50% or 90% conversion [48,49]. Reactivity calculated at 50% conversion does not account for the possible effects associated with ash accumulation at high conversion while R_x calculated at 90% does. Therefore, in this study, reactivity is calculated at both conversions in an attempt to gain an insight on the reactivity spanning over a broader conversion spectrum. It is postulated that when the ash does not have a significant inhibition effect on char gasification, then reactivity at these two different conversions is similar. The reactivity index is calculated as follows,

$$R_x = \frac{t_x}{x} \tag{2-10}$$

where $t_x$is the gasification time in minutes needed to reach char conversion of x

Figure 2-12 shows the relationship between pyrolytic tire char reactivity index and gasification temperature.

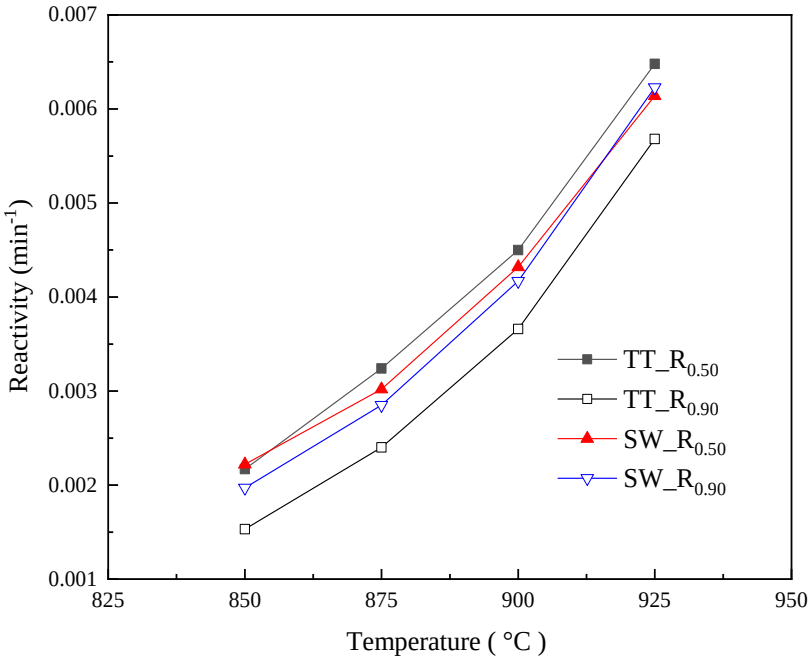

Figure 2-12. Variation of char reactivity with temperature at 50 and 90% conversion

As expected from endothermic reactions, both TT and SW char reactivity increases with temperature. The difference in SW reactivity calculated according to $R_{0.50}$ and $R_{0.90}$ is very small, with the former slightly higher than the latter. This dissimilarity decreases with temperature increase. This observation confirms the absence of inhibition effects even at high conversions, and in fact, the ash effect is diminished as temperature increases. Given the nature and amount of ash, this could mean that ash species are expelled together with product gas, through volatilization and possibly thermal decomposition of sulfides and oxides. On the other hand, the magnitude of difference between $R_{0.50}$ and $R_{0.90}$ for TT is significant, the change in reactivity averages at 21.6%. This order of magnitude confirms the presence of inhibition imposed by ash accumulation on char particles. In contrast to SW char, the difference is not diminished by an increase in temperature, suggesting that ash species are immobilised in ash clusters. Interestingly, according to $R_{0.50,}$ TT char has a slightly higher reactivity compared to SW char, while according to $R_{0.90}$, SW has a much higher reactivity. These seemingly contradicting results are a consequence of the role of ash during gasification. It is reasoned that at lower conversions, active ash species in TT char participate in gasification reaction, however as carbon is consumed more inert ash is exposed and in turn act as sites for active catalyst deactivation and immobilisation. These clusters also prevent gas penetration into char.

The reactivity of tire chars between 850 and 925 °C is in the range of 1.5×10^{-3} - 6.5×10^{-3} min^{-1}. Wei et al. [23] reported that the reactivity of bituminous coal within a similar temperature range was 1.1×10^{-2} - 6.4×10^{-2} min^{-1}. It is observed that tire char reactivity is significantly lower than coal, although pyrolytic tire char has a higher surface area than coal char.

2.4 Conclusion

The CO_2 gasification kinetics of TT and SW char between 850 and 925°C were determined using a TGA. Gasification profiles for TT and SW is described by the random pore model and zeroth order reaction mechanism, respectively. The activation energy for TT and SW is 177.1 kJ mol^{-1} and 165.6 kJ $mol^{-1,}$ respectively. The consistency of the kinetic parameters was tested using a model-free method. The difference in the morphological evolution of the two chars was found to be as a result of ash proportion. Ash clusters found in TT char and had a negative effect on the reactivity and morphological evolution of char during gasification. High inert ash content in char is associated with a drop in gasification reactivity at high conversions due to ash encapsulation and suppression of pore structure development. Although the kinetic parameters are not very different, the char-ash transformation of TT may result in unreacted

carbon in the ash, thus not fully utilising the fuel. Unreacted carbon in slag/ash is a common gasifier operational concern associated with high inert ash carbonaceous material. The findings in this study may be used to justify separation of waste tire into SW and TT prior reactor charging, to avert the problem. This can be done easily by using conventional tire tread cutters, normally used during tire re-treading.

References

[1] Loloie Z, Mozaffarian M, Soleimani M, Asassian N. Carbonization and CO_2 activation of scrap tires: Optimization of specific surface area by the Taguchi method. Korean J Chem Eng 2017;34:366–75. https://doi.org/10.1007/s11814-016-0266-4.

[2] Labaki M, Jeguirim M. Thermochemical conversion of waste tires—a review. Environ Sci Pollut Res 2017;24:9962–92. https://doi.org/10.1007/s11356-016-7780-0.

[3] Wang WC, Bai CJ, Lin CT, Prakash S. Alternative fuel produced from thermal pyrolysis of waste tires and its use in a di diesel engine. Appl Therm Eng 2016;93:330–8. https://doi.org/10.1016/j.applthermaleng.2015.09.056.

[4] Oboirien BO, North BC. A review of waste tire gasification. J Environ Chem Eng 2017;5:5169–78. https://doi.org/10.1016/j.jece.2017.09.057.

[5] Martínez JD, Cardona-Uribe N, Murillo R, García T, López JM. Carbon black recovery from waste tire pyrolysis by demineralization: Production and application in rubber compounding. Waste Manag 2019;85:574–84. https://doi.org/10.1016/j.wasman.2019.01.016.

[6] Donatelli A, Iovane P, Molino A. High energy syngas production by waste tires steam gasification in a rotary kiln pilot plant. Experimental and numerical investigations. Fuel 2010;89:2721–8. https://doi.org/10.1016/j.fuel.2010.03.040.

[7] Huo W, Zhou Z, Wang F, Wang Y, Yu G. Experimental study of pore diffusion effect on char gasification with CO_2 and steam. Fuel 2014;131:59–65. https://doi.org/10.1016/j.fuel.2014.04.058.

[8] Varde N, Fogler HS. Asynchronous learning of chemical reaction engineering. vol. 35. 2001.

[9] Lahijani P, Mohammadi M, Mohamed AR. Investigation of synergism and kinetic analysis during CO_2 co-gasification of scrap tire char and agro-wastes. Renew Energy 2019;142:147–57. https://doi.org/10.1016/j.renene.2019.04.113.

[10] Lahijani P, Zainal ZA, Mohamed AR, Mohammadi M. Co-gasification of tire and biomass for enhancement of tire-char reactivity in CO_2 gasification process. Bioresour Technol 2013;138:124–30. https://doi.org/10.1016/j.biortech.2013.03.179.

[11] Lahijani P, Mohammadi M, Mohamed AR. Investigation of synergy and inhibition effects during co-gasification of tire char and biomass in CO_2 environment. Biomass Convers Biorefinery 2020. https://doi.org/10.1007/s13399-020-01028-x.

[12] Murillo R, Navarro M V., López JM, García T, Callén MS, Aylón E, et al. Activation of pyrolytic tire char with CO2: Kinetic study. J Anal Appl Pyrolysis 2004;71:945–57. https://doi.org/10.1016/j.jaap.2003.12.005.

[13] Cunliffe AM, Williams PT. Influence of process conditions on the rate of activation of chars derived from pyrolysis of used tires. Energy and Fuels 1999;13:166–75. https://doi.org/10.1021/ef9801524.

[14] Lee JS, Kim SD. Gasification kinetics of waste tire-char with CO_2 in a thermobalance reactor. Energy 1996;21:343–52. https://doi.org/10.1016/0360-5442(95)00119-0.

[15] Preciado-Hernandez J, Zhang J, Zhu M, Zhang Z, Zhang D. An experimental study of CO_2 gasification kinetics during activation of a spent tire pyrolysis char. Chem Eng Res Des 2019;149:129–37. https://doi.org/10.1016/j.cherd.2019.07.007.

[16] Kong Y, Kim J, Chun D, Lee S, Rhim Y, Lim J, et al. Comparative studies on steam gasification of ash-free coals and their original raw coals. Int J Hydrogen Energy 2014;39:9212–20. https://doi.org/10.1016/j.ijhydene.2014.04.054.

[17] Ochoa J, Cassanello MC, Bonelli PR, Cukierman AL. CO_2 gasification of Argentinean coal chars: A kinetic characterization. Fuel Process Technol 2001;74:161–76. https://doi.org/10.1016/S0378-3820(01)00235-1.

[18] Mühlen HJ, Sowa F, van Heek KH. Comparison of the gasification behaviour of a West and East German Brown coal. Fuel Process Technol 1993;36:185–91. https://doi.org/10.1016/0378-3820(93)90026-Z.

[19] Shenqi X, Zhijie Z, Jie X, Guangsuo Y, Fuchen W. Effects of alkaline metal on coal gasification at pyrolysis and gasification phases. Fuel 2011;90:1723–30. https://doi.org/10.1016/j.fuel.2011.01.033.

[20] Moulijn JA, Cerfontain MB, Kapteijn F. Mechanism of the potassium catalysed gasification of carbon in CO_2. Fuel 1984;63:1043–7. https://doi.org/10.1016/0016-2361(84)90185-6.

[21] Li S, Whitty KJ. Physical phenomena of char-slag transition in pulverized coal

gasification. Fuel Process Technol 2012;95:127–36. https://doi.org/10.1016/j.fuproc.2011.12.006.

[22] Ding L, Dai Z, Guo Q, Yu G. Effects of in-situ interactions between steam and coal on pyrolysis and gasification characteristics of pulverized coals and coal water slurry. Appl Energy 2017;187:627–39. https://doi.org/10.1016/j.apenergy.2016.11.086.

[23] Wei J, Guo Q, He Q, Ding L, Yoshikawa K, Yu G. Co-gasification of bituminous coal and hydrochar derived from municipal solid waste: Reactivity and synergy. Bioresour Technol 2017;239:482–9. https://doi.org/10.1016/j.biortech.2017.05.014.

[24] Wang M, Zhang L, Li A, Irfan M, Du Y, Di W. Comparative pyrolysis behaviors of tire tread and side wall from waste tire and characterization of the resulting chars. J Environ Manage 2019;232:364–71. https://doi.org/10.1016/j.jenvman.2018.10.091.

[25] Di Blasi C. Modeling chemical and physical processes of wood and biomass pyrolysis. Prog Energy Combust Sci 2008;34:47–90. https://doi.org/10.1016/J.PECS.2006.12.001.

[26] Irfan MF, Usman MR, Kusakabe K. Coal gasification in CO_2 atmosphere and its kinetics since 1948: A brief review. Energy 2011;36:12–40. https://doi.org/10.1016/j.energy.2010.10.034.

[27] Gomez A, Silbermann R, Mahinpey N. A comprehensive experimental procedure for CO2 coal gasification: Is there really a maximum reaction rate? Appl Energy 2014;124:73–81. https://doi.org/10.1016/j.apenergy.2014.02.077.

[28] Tanner J, Bhattacharya S. Kinetics of CO_2 and steam gasification of Victorian brown coal chars. Chem Eng J 2016;285:331–40. https://doi.org/10.1016/j.cej.2015.09.106.

[29] Hardi F, Imai A, Theppitak S, Kirtania K, Furusjö E, Umeki K, et al. Gasification of Char Derived from Catalytic Hydrothermal Liquefaction of Pine Sawdust under a CO_2 Atmosphere. Energy and Fuels 2018;32:5999–6007. https://doi.org/10.1021/acs.energyfuels.8b00589.

[30] Ollero P, Serrera A, Arjona R, Alcantarilla S. Diffusional effects in TGA gasification experiments for kinetic determination. Fuel 2002;81:1989–2000. https://doi.org/10.1016/S0016-2361(02)00126-6.

[31] Wei J, Gong Y, Guo Q, Ding L, Wang F, Yu G. Physicochemical evolution during rice

straw and coal co-pyrolysis and its effect on co-gasification reactivity. Bioresour Technol 2017;227:345–52. https://doi.org/10.1016/J.BIORTECH.2016.12.068.

[32] Zhang Y, Zheng Y, Yang M, Song Y. Effect of fuel origin on synergy during co-gasification of biomass and coal in CO_2. Bioresour Technol 2016. https://doi.org/10.1016/j.biortech.2015.10.076.

[33] Novaković A, Van Lith SC, Frandsen FJ, Jensen PA, Holgersen LB. Release of potassium from the systems K-Ca-Si and K-Ca-P. Energy and Fuels 2009;23:3423–8. https://doi.org/10.1021/ef8010417.

[34] Shen L, Nakamura A, Murakami K. Effect of Fe_2O_3 on steam gasification of subbituminous coal/woody biomass mixture. Energy Sci Eng 2018;6:281–8. https://doi.org/10.1002/ese3.193.

[35] Undri A, Sacchi B, Cantisani E, Toccafondi N, Rosi L, Frediani M, et al. Carbon from microwave assisted pyrolysis of waste tires. J Anal Appl Pyrolysis 2013;104:396–404. https://doi.org/10.1016/j.jaap.2013.06.006.

[36] Ding L, Gong Y, Wang Y, Wang F, Yu G. Characterisation of the morphological changes and interactions in char, slag and ash during CO_2 gasification of rice straw and lignite. Appl Energy 2017;195:713–24. https://doi.org/10.1016/J.APENERGY.2017.03.098.

[37] Szekely J, Evans JW. A structural model for gas-solid reactions with a moving boundary. Chem Eng Sci 1970;25:1091–107. https://doi.org/10.1016/0009-2509(70)85053-9.

[38] Bhatia SK, Perlmutter DD. A random pore model for fluid-solid reactions: I. Isothermal, kinetic control. AIChE J 1980;26:379–86. https://doi.org/10.1002/aic.690260308.

[39] Zou X, Ding L, Liu X, Guo Q, Lu H, Gong X. Study on effects of ash on the evolution of physical and chemical structures of char during CO_2 gasification. Fuel 2018;217:587–96. https://doi.org/10.1016/j.fuel.2017.12.009.

[40] Ding L, Gong Y, Wang Y, Wang F, Yu G. Characterisation of the morphological changes and interactions in char, slag and ash during CO_2 gasification of rice straw and lignite. Appl Energy 2017;195:713–24.

https://doi.org/10.1016/J.APENERGY.2017.03.098.

[41] Senneca O, Salatino P, Masi S. Microstructural changes and loss of gasification reactivity of chars upon heat treatment. Fuel 1998;77:1483–93. https://doi.org/10.1016/S0016-2361(98)00056-8.

[42] Laurendeau NM. Heterogeneous kinetics of coal char gasification and combustion. Prog Energy Combust Sci 1978;4:221–70. https://doi.org/10.1016/0360-1285(78)90008-4.

[43] Russell N V., Gibbins JR, Williamson J. Structural ordering in high temperature coal chars and the effect on reactivity. Fuel 1999;78:803–7. https://doi.org/10.1016/S0016-2361(98)00210-5.

[44] Senneca O, Russo P, Salatino P, Masi S. The relevance of thermal annealing to the evolution of coal char gasification reactivity. Carbon N Y 1997;35:141–51. https://doi.org/10.1016/S0008-6223(96)00134-0.

[45] Roy C, Darmstadt H. Carbon blacks recovered from rubber waste by vacuum pyrolysis - Comparison with commercial grades. Plast Rubber Compos Process Appl 1998;27:341–5.

[46] Zabaniotou A, Madau P, Oudenne PD, Jung CG, Delplancke MP, Fontana A. Active carbon production from used tire in two-stage procedure: Industrial pyrolysis and bench scale activation with H_2O-CO_2 mixture. J Anal Appl Pyrolysis 2004;72:289–97. https://doi.org/10.1016/j.jaap.2004.08.002.

[47] López G, Olazar M, Artetxe M, Amutio M, Elordi G, Bilbao J. Steam activation of pyrolytic tire char at different temperatures. J Anal Appl Pyrolysis 2009;85:539–43. https://doi.org/10.1016/j.jaap.2008.11.002.

[48] Gil M V., Riaza J, Álvarez L, Pevida C, Rubiera F. Biomass devolatilization at high temperature under N_2 and CO_2: Char morphology and reactivity. Energy 2015;91:655–62. https://doi.org/10.1016/j.energy.2015.08.074.

[49] Zhou ZJ, Hu QJ, Liu X, Yu GS, Wang FC. Effect of iron species and calcium hydroxide on high-sulfur petroleum coke CO_2 gasification. Energy and Fuels 2012;26:1489–95. https://doi.org/10.1021/ef201442t.

Chapter 3: **Effect of hydrothermal treatment on coconut fiber demineralization and pyrolysis behavior**

Abstract: *Coconut fiber was subjected to hydrothermal treatment to improve its fuel properties and reduce potassium concentration. The effect of hydrothermal treatment (180°C–220°C) (and water washing) on coconut fiber demineralization and pyrolysis behavior was investigated. The high-heating value (HHV) of RCF is 17.9 MJ kg^{-1}; however, the HHV of resultant solids improved by 9.7%–20.1% after hydrothermal treatment. The energy density of coconut fiber is comparable to subbituminous coal after hydrothermal transformation. Chemical fractionation method classified the most occurring inorganic (potassium) as ~76% water-soluble, ~19% ion-exchangeable, and ~5% acid-soluble species. Demineralization results show that combined pretreatment at ≤200°C leached out all water-soluble and exchangeable potassium. However, at 220°C, electrostatic attraction and increased tortuosity imposed by the high density of oxygenated functional groups and a well-developed porous structure hamper demineralization. Nevertheless, a maximum potassium removal efficiency of 95% could be achieved. Although pretreatment marginally affects apparent activation energy, the reaction mechanism of hydrochars became insensitive to the heating rate between 10 and 50°C min^{-1}. Due to pretreatment, the selectivity of thermally stable phenolic and anhydrosugar derivatives increased at the expense of the light oxygenates of low thermal stability because of suppressing fragmentation reactions and enriching polymers with a high degree of polymerization. Light oxygenates decreased from 27.45 area % to 24.02, 16.33, and 13.32 area % for hydrochars produced at 180°C, 200°C, and 220°C, respectively. The high demineralization efficiency shows that coconut fiber can be used liberally without posing significant ash-related problems, moreover hydrothermal treatment can improve the energy density of coconut fiber.*

3.1 Introduction

Applying thermochemical conversion for producing clean fuels is vital in alleviating environmental problems and ensuring a sustainable use, management, and disposal of agricultural wastes, such as coconut residue. Coconut waste is a vast resource with a global annual production of approximately 12 million tons of copra equivalent, potentially generating at least 39,400-GWh power in gasifiers [1]. Typically, coconut fiber is a recalcitrant and potassium-rich lignocellulosic biomass [2] that can be used as feedstock in bio-oil and syngas production [3–5]. However, the high moisture content, low energy density, inherent alkaline and alkaline earth metals (AAEMs), and other inorganics impede the direct application of coconut fiber, compromising the integrity of reactors within which the thermochemical conversion occurs [6,7]. The high moisture content associated with freshly harvested biomass and its hygroscopic nature exacerbate contamination because evolved vapor function as a medium through which water-soluble inorganics are transferred into the syngas and on reactor walls. Ash-related issues associated with a high concentration of AAEM include alkaline-induced slagging, silica-melt-induced slagging or ash fusion, agglomeration, and corrosion [6]. Hydrothermal treatment (HTT) can mitigate these shortcomings. Although a reduction in equilibrium moisture content and significant improvements in fuel properties are possible simultaneously, only partial demineralization is achieved under conditions of practical importance [8,9]. Therefore, HTT is frequently followed by water washing to remove persistent residual inorganics [9].

Hydrothermal biomass transformation is achieved in an aqueous medium under subcritical conditions via hydrolysis, deoxygenation, aromatization, and recondensation reactions [10]. The transformation is illustrated in Figure 3-1[10]. Coconut fiber demineralization using HTT has not garnered much attention; however, several studies have been conducted for other biomass [9,11–13]. These studies emphasized the demineralization degree as a function of HTT temperature, reaction time [11,14], and biomass/water ratio [9,15]. Several anomalous behaviors have been observed in some studies, but have not been extensively investigated. Among these is the break in the monotonic relationship between AAEMs' removal efficiency and HTT temperature between 200°C and 220°C [9]. Moreover, the development of inorganic-retaining properties imposed at elevated hydrothermal treatment intensities has occurred [16]. AAEMs' influence (water-soluble, ion-exchangeable, and acid-soluble species) on demineralization must also be delineated in the same context. These different AAEMs classes should, therefore, behave differently during pretreatment. This pretreatment technique allows

investigating these phenomena because, under subcritical conditions, water functions as an acidic organic solvent because of a change in the ionic product and dielectric constant [17]. Simultaneously, biomass monomer degradation produces organic acidic hydrolysates (acetic, levulinic, and galactouronic acid), providing an acidic environment in which ion exchange and acid solubilization can occur [16,17]. Therefore, the authors address the notable research gaps to gain further insights into demineralization phenomena using hydrothermal pretreatment. The control of AAEMs is a critical factor in assessing the application of biomass, AAEM-lean biomass like wood is preferred because it does not cause severe reactor problems. Therefore, the total removal of mobile AAEMs is a good indicator of the applicability of AAEM-rich biomass in gasification facilities.

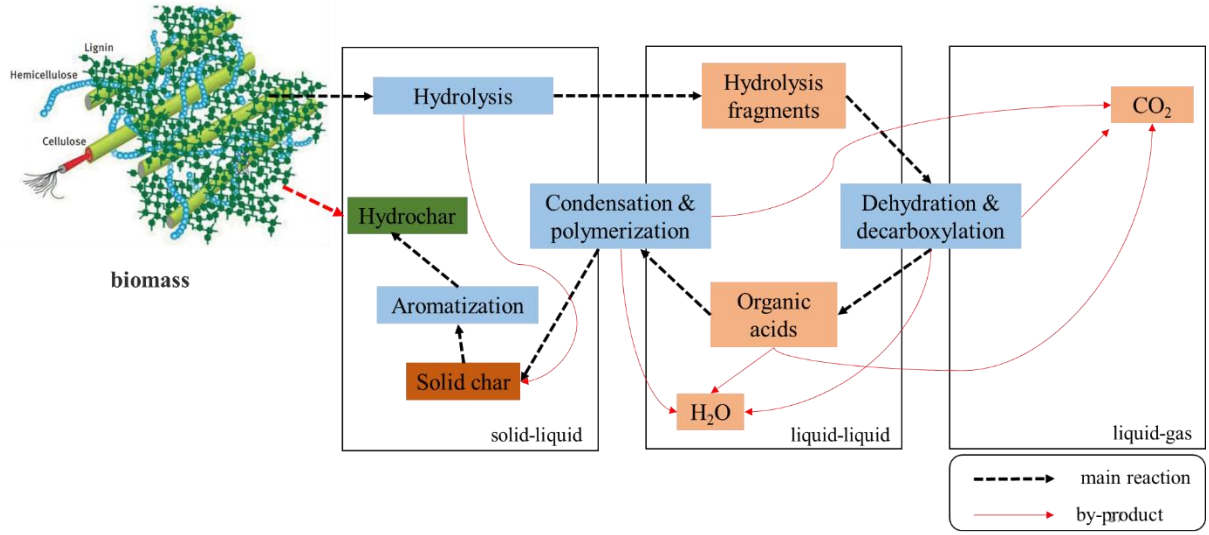

Figure 3-1. Hydrothermal transformation of biomass

In addition to investigating the effect of HTT temperature on fuel properties of coconut fiber his study also investigates the effect of HTT and water washing on removing water-soluble, ion-exchangeable, and acid-soluble potassium as a function of HTT intensity. Furthermore, the influence of physicochemical evolution (active oxygenated functional groups and specific surface area) imposed by the hydrothermal carbonization on leaching behavior during pretreatment is discussed. The effect of HTT on pyrolysis kinetics and mechanisms was determined using thermogravimetric analysis, whereas the pyrolysates composition was evaluated using pyrolysis-gas chromatography/mass spectrometry (Py-GC/MS).

3.2 Materials and Methods

3.2.1 Hydrothermal treatment and washing

An electric-heated and continuously stirred (120 rpm) autoclave reactor (MMJ-500, OM Lab Tech, Japan) of heating rate 7°C min^{-1} was employed for all hydrothermal treatment runs. Each of three experimental runs was initiated by loading the reactor with 20 g of raw coconut fiber (RCF) and 200 g of distilled water. Then the reactor was purged using argon and heated to a target temperature (180, 200, and 220°C), where it was held for 30 min. After that, the reactor was gradually cooled to 35°C, vented, and the slurry was offloaded and dewatered using vacuum filtration. The pH of the exhaust liquid fraction was then measured. The solid hydrochar was divided into two fractions, and one fraction was then immediately used for water-washing experiments while the other was left as is. Unwashed samples were dried in an oven at 105°C for 24 h and stored in air-tight bags for further analysis. In the washing step, 2 g (dry mass) samples were put in 25 µm nylon bags and placed in a Buchner funnel connected to a vacuum pump. These samples were then washed with ultra-pure water for 5.0 min to effect semi continuous washing of hydrochars. The funnel was kept half-filled with water throughout the washing step. After completing washing tests, the solid residue was oven-dried at 105°C for 24 h. The washed hydrochars produced at temperatures 180, 200, and 220°C, were tagged HTW180, HTW200, and HTW220, while the unwashed hydrochars were tagged HT180, HT200, and HT220, respectively.

3.2.2 Analysis of samples

Proximate and ultimate analysis results shown in Table 3-1 were obtained according to the standard methods ASTM D1765-84 (2007) and ASTM D3176-89 (2002), respectively. The chemical composition results shown in Table 3-2 were determined by standard procedures described in detail in earlier publications [18,19]. The modified chemical fractionation analysis employing semi continuous water washing [20] was used to determine potassium species' occurrence (as water-soluble (K[H_2O]), ion-exchangeable (K[NH_4Ac]), and acid-soluble (K[HCl])). The AAEM concentration of different fractions was measured with an inductively coupled plasma optical emission spectrometer (ICPE-9000, Shimadzu, Japan). X-ray fluorescence spectrometry (XRF; S2 Ranger/LE, Bruker AXS, Germany) was used to determine the ash composition of raw coconut fiber. Boehm back titration was used to estimate reactive OFGs which are typically carboxylic, lactonic and phenolic groups on the accessible surface of samples, and comprehensive details of the method are reported elsewhere [21].

Table 3-1. Composition of RCF and hydrochars

Samples	Ultimate Analysis (wt.%)						Proximate Analysis (wt.%)		
	C	O*	H	N	S	Cl	FC	VM	Ash
RCF	45.58	44.33	5.64	0.33	0.06	0.46	17.95	78.45	3.60
HT180	49.26	42.80	5.85	0.24	0.01	0.34	18.68	79.82	1.50
HT200	51.73	40.73	5.75	0.19	0.03	0.07	21.52	76.98	1.50
HT220	53.95	38.20	5.64	0.30	0.02	0.19	26.73	71.57	1.70

*Oxygen was calculated by difference.

Qualitative analysis of OFGs was determined using Fourier-transformed infrared spectroscopy (FTIR) in the range of 4000 - 400 $cm^{-1.}$ It should be noted that the term OFGs in this paper only refers to reactive OFGs, and does not account for stable OFGs (ether or quinone, or pyrone). The surface area was measured by the N_2 gas adsorption method using an ASAP 2020 analyzer at 77.15 K for pores with a diameter range from 2 to 200 nm, and the Brunauer−Emmet−Teller (BET) model was applied to calculate specific surface areas of samples.

Table 3-2. Chemical composition of RCF and washed hydrochars

Component	RCF	HT180	HT200	HT220
Monosaccharides [a]	66.40	67.70	70.10	72.00
Arabinose	0.60 (0.06)	0.10 (0.04)	0.10 (0.05)	0.10 (0.04)
Galactose	0.40 (0.05)	0.10 (0.02)	0.80 (0.03)	0.00
Glucose	46.30 (0.11)	52.10 (0.09)	68.30 (0.11)	71.30 (0.08)
Xylose	19.10 (0.07)	15.40 (0.10)	0.90 (0.08)	0.60 (0.04)
Mannose	0.00	0.00	0.00	0.00
Lignin	29.30	27.40	25.10	23.30
Acid Insoluble	27.00 (0.31)	26.20 (0.41)	24.30 (0.31)	22.90 (0.50)
Acid soluble	2.30 (0.21)	1.22 (0.10)	0.80 (0.10)	0.40 (0.30)
Extractives	1.90 (0.30)	1.20 (0.20	0.70 (0.10)	0.40 (0.20)
Others [b]	2.30 (0.13)	3.60 (0.17)	4.10 (0.12)	4.30 (0.09)
Total	100	100	100	100

The values in parenthesis are standard deviation analysis results.
[a] Monosaccharide moieties are presented as their anhydro forms
[b] Includes acetyl groups of xylan, pectin and proteins

3.2.3 Py-GCMS experiments.

The analyses of pyrolysates containing GC-amenable compounds were performed using a foil pulse Pyrola 2000 pyrolyzer (Pyrol AB, Lund, Sweden) connected to the GC-MS instrument (Agilent GC model 7890B coupled to an Agilent 5977B quadrupole-MSD with EI ionization). The column was a 25 m x 0.2 mm i.d., 0.33 mm HP-5 column (Agilent Technologies Inc.), and

the carrier gas was helium gas injected at a flow rate of 0.8 ml min^{-1}. The oven temperature program is; 50ºC (held for 1.0 min) to 300ºC at 8ºC min^{-1}. The injector temperature was 300ºC with a split at 20 ml min^{-1}. The samples were pyrolyzed at 600ºC with 2 seconds residence time. The EI mode with 70 eV was applied. The identification of the eluted compounds was done by comparing the spectra with those of spectral libraries (Wiley 10 and NIST 2012). The components were semi-quantified by calculating the percentage of each compound based on the total peak area of all identified compounds.

3.2.4 Thermogravimetric experiments.

Pyrolysis experiments for kinetic analysis were carried out under high-purity N_2 at a flow rate of 150 ml min^{-1} in a thermogravimetric analyzer employing an alumina crucible measuring 15 mm diameter and 2 mm height. Each experimental run was carried on an 8.0 ± 0.5 mg sample with particle size measuring ~100 µm. These conditions were chosen to eliminate diffusion effects often associated with thermogravimetric analysis, details are reported a previous study [22]. The samples were heated from ambient temperature to 105°C at a heating rate of 5°C min^{-1} and held for 15 min to ensure moisture elimination. After that, samples were then heated to 900°C at varying heating rates of 10, 20, 30, 40, and 50°C min^{-1}. Experiments were done in duplicate to ensure reproducibility.

3.2.5 Kinetic analysis

Thermally stimulated heterogeneous solid-state reaction kinetics can be described by the fundamental equation,

$$\frac{d\alpha}{dt} = k(T)f(\alpha) = A\exp\left(-\frac{E_\alpha}{RT}\right)f(\alpha) \qquad (3\text{-}1)$$

where $d\alpha/dt$ is the reaction rate, $k(T)$ is the Arrhenius rate constant, T is the temperature, A is the pre-exponential factor, t is the time , E_α is the activation energy and R is the universal gas constant (8.314 J K^{-1} mol^{-1}) and $f(\alpha)$ is the reaction model. The experimental conversion α is calculated from the following equation;

$$\alpha = \frac{m_0 - m_t}{m_0 - m_r} \qquad (3\text{-}2)$$

where m_0, m_t and m_r are the initial mass, mass at any given time and the residual mass after pyrolysis.

The activation energy E_α at any particular conversion α is determined by using the Vyazovkin AIC (advanced isoconversional) method, which minimizes the function $\Phi(E_\alpha)$,

$$\Phi(E_\alpha) = \sum_{i}^{n} \sum_{j \neq i}^{n} \frac{I(E_\alpha, T_i(t_\alpha))}{I(E_\alpha, T_j(t_\alpha))} = \min \tag{3-3}$$

In the following equation,

$$J(E_\alpha, T(t)) = \int_{T_{\alpha-\Delta\alpha}}^{T_\alpha} \exp\left(\frac{-E}{RT(t)}\right) dt \tag{3-4}$$

where n is the number of heating programs and $T_i(t)$ is the actual reaction temperature variation. Substituting the time, t_α , at a particular conversion α and corresponding reaction temperature T into Equation 3-3 and varying E_α until the minimum is attained gives an estimate of activation energy. The trapezoidal rule with a step size of 0.01 was used to evaluate the integral in Equation 3-4.

3.2.6 Criado method

The kinetic mechanism describing solid-state thermo-chemical conversion of biomass in an inert environment was determined by the Criado method [23] shown in Equation 3-5:

$$\frac{Z(\alpha)}{Z(0.5)} = \frac{f(\alpha) \times g(\alpha)}{f(0.5) \times g(0.5)} = \left(\frac{T_\alpha}{T_{0.5}}\right)^2 \times \frac{(d\alpha/dt)_\alpha}{(d\alpha/dt)_{0.5}} \tag{3-5}$$

where $f(\alpha)$ and $g(\alpha)$ represent differential and integral algebraic expressions describing solid-state kinetic models. A list of these models is shown in Table 3-3. T_α is the pyrolysis temperature recorded at conversion degree α.

Table 3-3. Pyrolysis reaction models with different f(α) and g(α) functions

Symbols	Mechanisms	$f(\alpha)$	$g(\alpha)$
Diffusion reaction			
D1	One-way transport	$(1/2)\alpha$	α^2
D2	Two-way transport (Valensi model)	$[-\ln(1-\alpha)]^{-1}$	$\alpha+(1-\alpha)\ln(1-\alpha)$
D3	Three-way transport (Jander model)	$(3/2)(1-\alpha)^{2/3}[1-(1-\alpha)^{1/3}]^{-1}$	$[1-(1-\alpha)^{1/3}]^2$
D4 (GB)	Ginstling–Brounshtein equation	$(2/3)(1-\alpha)^{2/3}[1-(1-\alpha)^{1/3}]$	$1-2\alpha/3-(1-\alpha)^{2/3}$
Zh	Zhravlev equation	$(2/3)(1-\alpha)^{5/3}/[1-(1-\alpha)^{1/3}]$	$[(1-\alpha)^{-1/3}-1]^2$
Order-based reaction			
R1	1st order random nucleation	$(1-\alpha)$	$-\ln(1-\alpha)$
R2	2nd order random nucleation	$(1-\alpha)^2$	$(1-\alpha)^{-1}-1$
R3	3rd order random nucleation	$(1-\alpha)^3$	$(1/2)[(1-\alpha)^{-2}-1]$
Chemical reaction			
F1	First-order reaction	$\alpha(1-\alpha)$	$-\ln(1-\alpha)$
F2	Contracting cylinder	$2(1-\alpha)^{2/3}$	$1-(1-\alpha)^{1/2}$
F3	Contracting sphere	$2(1-\alpha)^{2/3}$	$1-(1-\alpha)^{1/3}$
Power models			
P2	Power law	$2\alpha^{1/2}$	$\alpha^{1/2}$
P3	Power law	$3\alpha^{2/3}$	$\alpha^{1/3}$
P4	Power law	$4\alpha^{3/4}$	$\alpha^{1/4}$
Nucleation models			
A1	Avrami–Erofeev	$(1/2)(1-\alpha)[-\ln(1-\alpha)]^{1/3}$	$[-\ln(1-\alpha)]^{2/3}$
A2	Avrami–Erofeev	$2(1-\alpha)[-\ln(1-\alpha)]^{1/2}$	$[-\ln(1-\alpha)]^{1/2}$
A3	Avrami–Erofeev	$3(1-\alpha)[-\ln(1-\alpha)]^{2/3}$	$[-\ln(1-\alpha)]^{1/3}$
A4	Avrami–Erofeev	$4(1-\alpha)[-\ln(1-\alpha)]^{3/4}$	$[-\ln(1-\alpha)]^{1/4}$

3.3 Results and Discussion

3.3.1 Proximate, ultimate, and XRF analysis

Table 3-1 shows the proximate and ultimate analysis results of RCF, hydrochars, and washed hydrochars. A typical mass and components balance for RCF hydrolyzed at 220°C is shown in the Figure 3-2. After HTT at 180°C, 200°C, and 220°C, coconut fibers retained 80.9%, 77.1%, and 71.7% of their original mass, respectively. This trend is attributed to the increased solubilization of hemicellulose, which is intensified at elevated temperatures. As a result, the carbon content in hydrochars increased from 45.58% to a range of 49.26 - 53.95%; simultaneously, the oxygen content decreased from 44.33 to a range of 42.80 - 38.20 %. An increase in carbon content is accompanied by an increase in fixed carbon content and a decrease in the volatile matter, as shown by the proximate analysis results. These increases in carbonization degree can be clearly explained using changes in the atomic ratios of O/C and H/C represented in the Van Krevelen diagram (Figure 3-3) .The high-heating value (HHV) [24] of RCF is 17.9 MJ kg^{-1}; however, the HHV of resultant solids improved by 9.7%–20.1%.

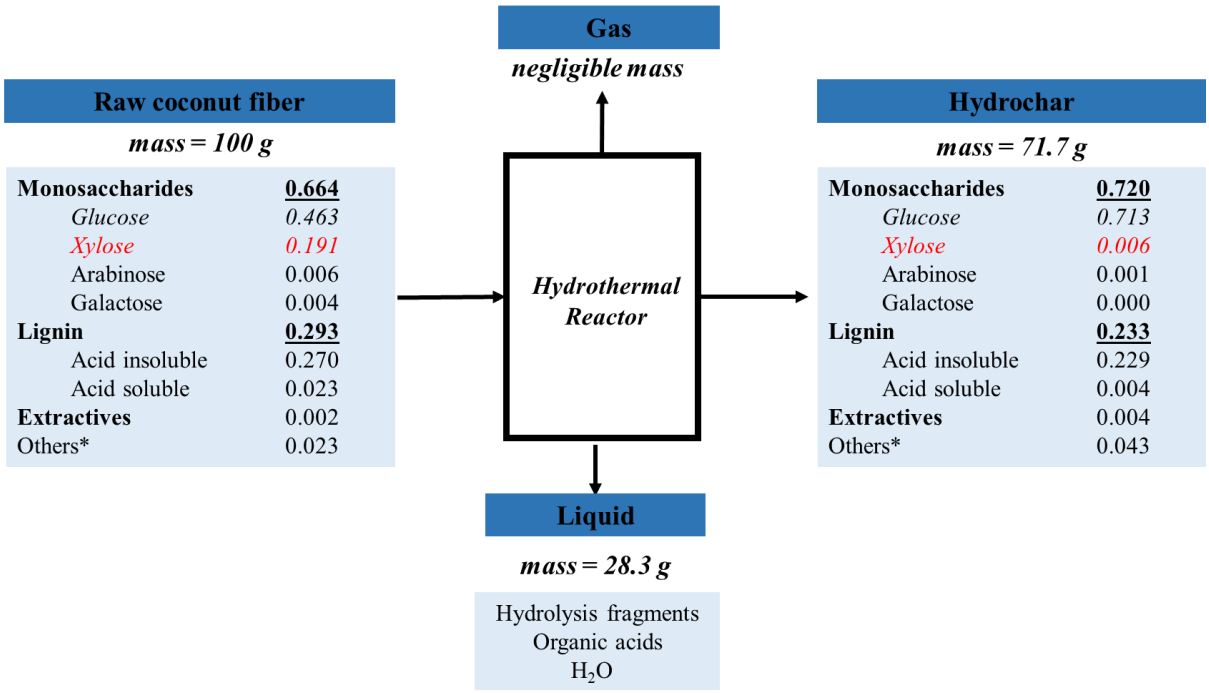

Figure 3-2. Mass and component balance for RCF hydrolysed at 220°C

The enhancement degree is a function of carbonization temperature. The monotonic relationship between carbon content and HTT temperature corroborates this observation. The HHV of the hydrochars is in the range of 19.66-21.53 MJ/kg, which is similar to the energy density of sub-bituminous coal (18-25 MJ/kg). Therefore, hydrothermal treatment is an effective approach to improving fuel properties because the hydrochars have energy density comparable to coal. Combined HTT and washing remarkably reduced the mineral content, with chlorine being removed entirely. Therefore, inorganic chlorine primarily exists as water-soluble species in the coconut fiber. From the Van Krevelen diagram in Figure 3-3, the hydrothermal transformation of RCF into energy-dense hydrochars was achieved mainly through the dehydration reaction pathway and, to a lesser degree, decarboxylation reactions.

These reactions entail extensively degrading polysaccharides with a low degree of polymerization (xylose) and enriching polysaccharides with a high degree of polymerization (glucose). The ash analysis of the most abundant mineral content in RCF expressed in weight % is K_2O = 45.12%, SiO_2 = 32.85%, CaO = 5.80%, Na_2O = 3.79%, MgO = 2.06%, Fe_2O_3 = 1.64%, and Al_2O_3 = 1.50%. Because K is the most abundant and notorious AAEM, this study focuses exclusively on K removal using HTT.

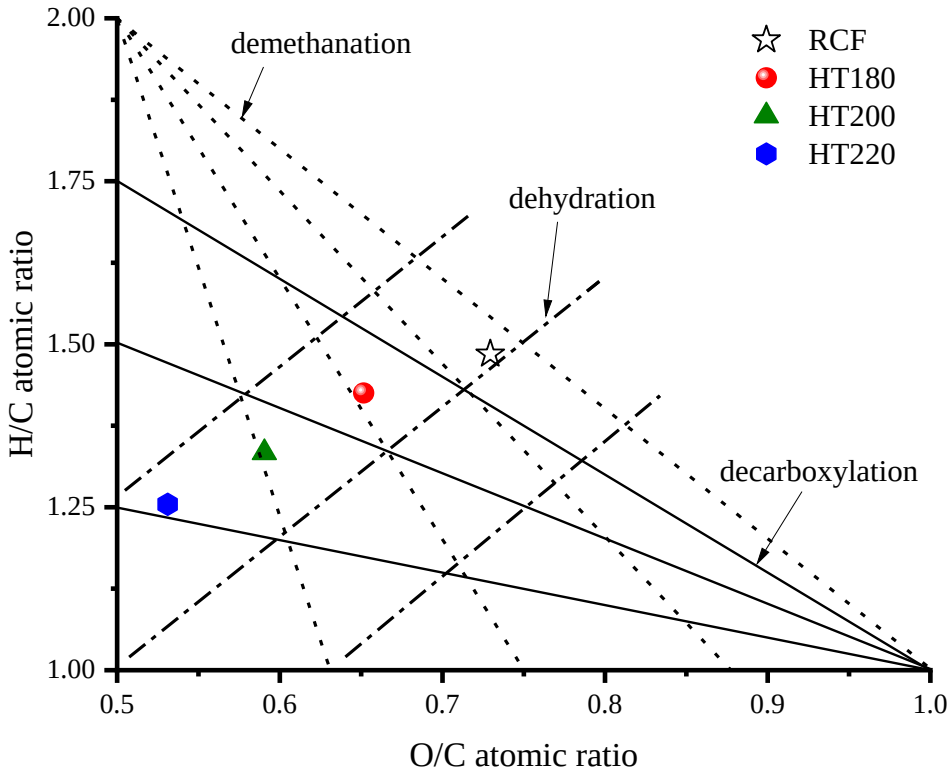

Figure 3-3. Van Krevelen diagram for raw coconut fiber (RCF), hydrochars produced at 180°C (HT180), 200°C (HT200), and 220°C (HT220)

3.3.2 Chemical composition of samples

Table 3-2 shows the chemical composition of ash-free RCF and resultant hydrochars. The coconut fibers mainly comprise carbohydrates (hemicellulose and cellulose) and lignin. Glucose and xylose, the principal monosaccharide moieties of cellulose and xylan, are the most abundant in RCF. Miscellaneous amounts of arabinose and galactose were also detected. However, mannose was below the detection limit. The occurrence of xylose and nonoccurrence of mannose indicate that RCF's monomeric composition is akin to hardwoods [25]; therefore, RCF is lean in hexoses (less than 30%). During pretreatment, the xylose/carbohydrate ratio reduced from 28.8% to 22.7%, 1.3%, and 0.8% for hydrochars produced at 180°C, 200°C, and 220°C, respectively. This trend can be attributed to hemicellulose hydrolysis, initialized by water ionization and catalyzed by the acidic environment provided by organic acids from biomass degradation. Typical organic acids formed from coconut residue degradation during HTT include but are not limited to formic, acetic, levulinic, and propionic acids [16]. The exhaust liquid fraction produced at 180°C, 200°C, and 220°C had pH values of 4.57, 4.02, and 4.11, respectively. Although HT220 has a greater hydrolysis extent of xylose than HT200, the

pH increased marginally. This pH increase can be attributed to repolymerization reactions (forming pseudolignins via the redeposition of hydrolysates, such as furfurals) [26].

The acid-soluble/acid-insoluble lignin ratio reduced from 7.8% to 1.7%–4.4% because of the acidic environment and scission of weak α-O-4 and β-O-4 ether linkages, which can be cleaved at low temperatures of 200°C–250°C [25,27]. Besides enhanced hydrolysis, the hydrolytic attack on lignin intensified as the temperature increased because of changes in the water's dielectric constant, improving its solvent properties for less-polar bio-components [28]. Therefore, as the hydrothermal carbonization intensified, the carbohydrate/lignin ratio increased from 2.3 to 2.5–3.1. From the Van Krevelen diagram and Table 3-2, HTT extensively ruptured the glycosidic bonds in hemicellulose and partially dissolved the lignin and cellulose via extensive dehydration and mild decarboxylation reaction pathways.

3.3.3 Effect of pretreatment on potassium demineralization

Figure 3-4 shows the occurrence, transformation, and removal of potassium species in RCF as a function of factors governing the demineralization degree, namely, pretreatment intensity and physicochemical structure evolution. From the modified chemical fractionation method, [20] the untreated sample comprises ~76% water-soluble, ~19% ion-exchangeable, and ~5% acid-soluble K species.

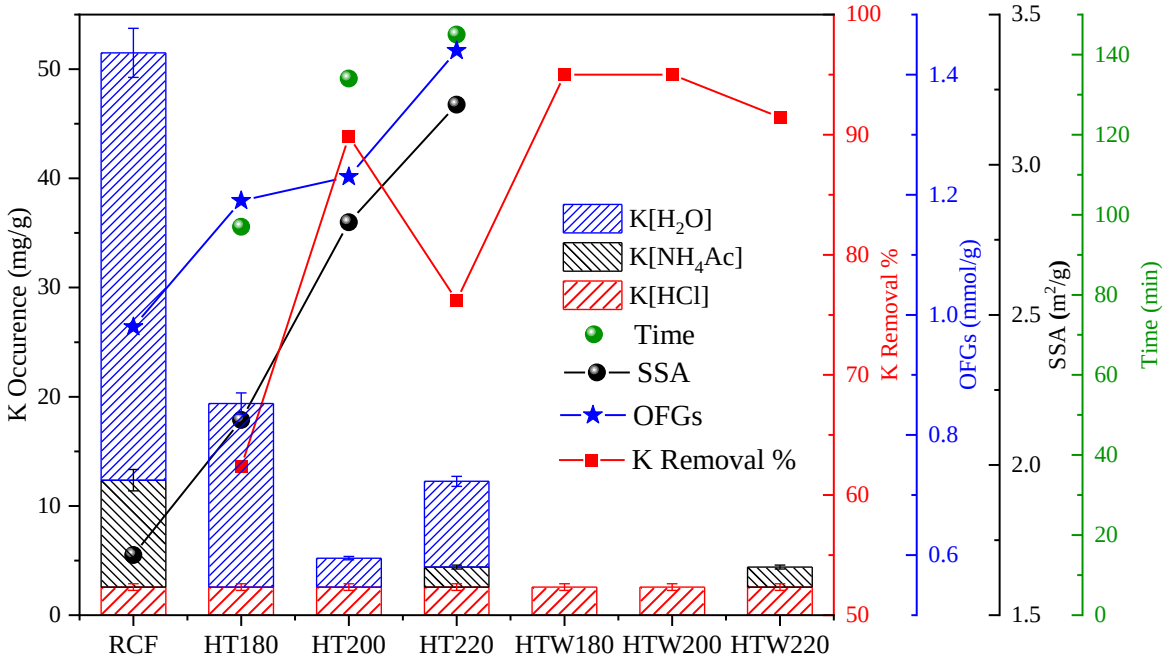

Figure 3-4. Effect of HTT and washing on removing water-soluble ($K[H_2O]$), ion-exchangeable ($K[NH_4Ac]$), and acid-soluble (K[HCl]) potassium as a function of HTT temperature, and specific surface area (SSA) and oxygenated functional groups (OFGs)

However, K frequently occurs in water-soluble and ion-exchangeable forms [29]; therefore, it is likely that K classified as acid-soluble occurs as included mineral in precipitated alkaline earth metal salts, such as calcium. This class of K species remained unaffected after HTT and washing. A recent study demonstrated that most calcium and magnesium-containing minerals were retained in coconut fibers after HTT in the same temperature range [2], corroborating the inference made above.

Hydrothermal pretreatment converts ion-exchangeable potassium species into water-soluble species because of the hydronium ion action generated by organic acids (formic, acetic, lactic, and propionic) from monomer degradation [30,31]. However, acid-soluble species remained unaffected, indicating that acidic conditions achieved during HTT were not stringent enough to effect solubilization. Liaw et al. [20] reported that K removal efficiency from mallee leaves and wood during water leaching increased with leaching time. Tan et al. [15] reported a similar relationship between K removal efficiency and time for low-temperature (≤120°C) HTT of empty fruit branch (EFB). Nurdiawati et al. [13] reported similar findings in demineralizing EFB using batch HTT between 100°C and 180°C. These studies were conducted under conditions that do not impose extensive active OFGs' emergence and micropore development to biomass. Therefore, when biomass retains most of its physicochemical integrity during demineralization in aqueous media, a monotonic relationship (direct proportionality) exists between demineralization degree and leaching time. Note that the leaching time represented in this figure is the period within which the fiber was in contact with water, including reactor heating time to the target temperature, holding time, and reactor cooling time. This relationship is evident for hydrochars produced below 220°C, indicating that the hydrothermal transformation degree is not as pronounced to alter leaching behavior within this range. However, for HT220, despite experiencing the harshest conditions and lengthy contact time, not all ion-exchangeable species were transformed, and more potassium species are retained in the hydrochar than for HT200. This anomalous demineralization trend indicates that at 220°C, the hydrothermal transformation of coconut fibers hampers leaching behavior. A similar trend for potassium removal was observed for EFB demineralization using HTT [9]; however, no detailed explanation or discussion was provided, except that it could be an artifact of increased porosity.

The anomalous trend could be associated with the physicochemical structure of hydrochars. FTIR analysis was performed to qualitatively depict the extent of the HTT-induced chemical transformation of fibers (Figure 3-5). The HT220 spectrum is distinct from all other spectra,

confirming that chemical transformation is more pronounced at temperatures ≥220°C; conversely, hydrochar produced at ≤200°C is similar to that of pristine coconut fiber. The most noticeable FTIR trace for HT220 is observed in region (3) with a peak of 1116 cm^{-1}, attributed to the C–O stretching in phenolic hydroxyl groups because of the surficial lignin enrichment from hemicellulose hydrolysis and pseudolignin formation. Therefore, a band in region (4) [875–750 cm^{-1}] for aromatic out-of-plane bonding is observed at a higher intensity for HT220. In region (2) [1800–1500 cm^{-1}], the peaks at 1593 and 1726 cm^{-1} are attributed to both conjugated and unconjugated C=O stretching, typically in carbonyl, carboxyl, quinone, or esters [32]. The broad band in region (1) is attributed to O–H stretching in carboxyl or hydroxyl groups, confirming OFGs. Boehm titration was used to estimate OFGs' concentration. In HT220, a significant emergence of new OFGs occur. Potassium removal efficiency can be correlated with OFGs prevalence and specific surface area. Discussed below are factors altering potassium-leaching behavior.

While the high concentration of K in HT180 and HT200 can easily be attributed to the short and long residence time, respectively, the same is untrue for HT220. The OFGs' density in and on hydrochars produced below 220°C is insignificant to pose a perceivable hindrance to the leaching rate.

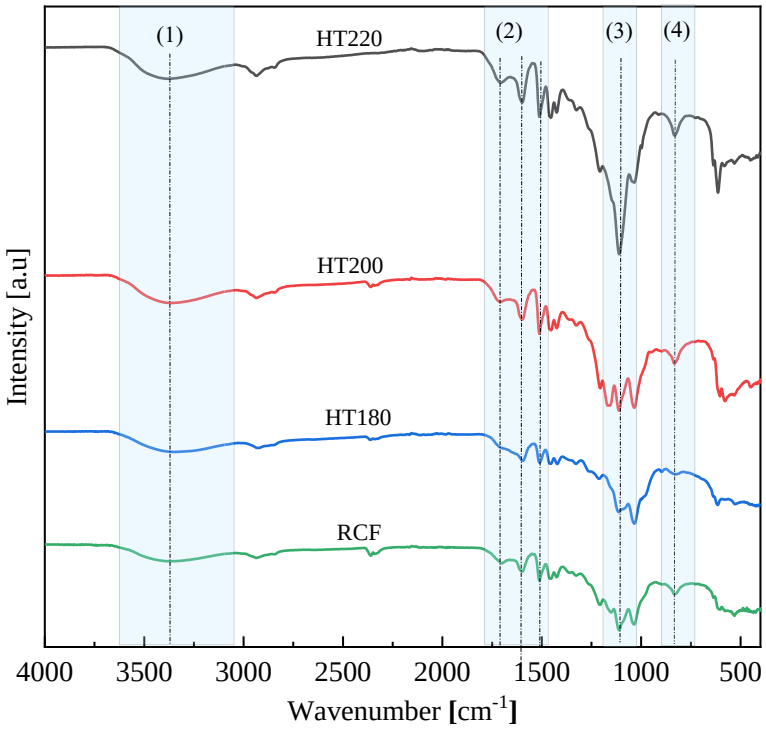

Figure 3-5. FTIR spectra of raw coconut fiber (RCF), hydrochars produced at 180°C (HT180), 200°C (HT200), and 220°C (HT220)

Furthermore, the change in the specific surface area and potassium retention within HT220 indicate complex porous network development, where the tortuosity is increased, decreasing cation effective diffusivity (leaching rate). Tortuosity can be defined as the ratio of the pathway length traversed by an ion within the porous structure to the shortest possible distance between two points. This specific surface area trend indicates that at 220°C, significant development of the porous structure occurs compared to lower temperatures. The high K retention corroborates this inference, despite extensive and lengthy contact with the hydronium-rich environment. The high OFGs' density within intraparticle porosity further intensifies mass transfer resistance by the electrostatic attraction between cationic species and lone pair electrons in OFGs. These intraparticle phenomena could be more prominent in narrower channels as the proximity between nucleophilic sites and cations increases. Because the formation of secondary organically bound K is improbable, the presence of K [NH_4Ac] could be because of an incomplete transformation, which is a consequence of the shielding effect imposed by the emergence of OFGs around these species. These nucleophilic groups hinder accessibility by either lowering the diffusion rate or immobilizing hydronium ions required for ion exchange within the carbonaceous matrix. Moreover, the increase in the liquid fraction pH at 220°C indicates that it is reasonable to infer that lignin/furfural recondensation reactions within the carbonaceous material could result in mass transfer limitations during K diffusion.

In summary, combined HTT and washing remove all water-soluble and organically bound K species through leaching and ion exchange when the physicochemical structure evolution is marginal. K retaining properties were attributed to the increased OFGs' concentration and porosity furnished at a hydrothermal temperature of 220°C. Therefore, lower temperatures are appropriate for maximum demineralization. The high removal efficiency of potassium indicates that coconut fiber can be used for gasification purposes without causing severe ash-related issues.

3.3.4 Effect of pretreatment on pyrolysis behaviour

Figure 3-6 shows the thermogravimetric conversion and derivative thermogravimetric (DTG) curves of RCF and hydrochars at heating rates between 10 and 50°C min^{-1}. Active pyrolysis is in the conversion range $\alpha = 0.05–0.80$, whereas passive pyrolysis is in the range $\alpha \geq 0.80$ for all samples. From the DTG for RCF, two prominent peaks exist. For example, for the heating rate of 50°C min^{-1}, the minor peak (310°C) and major peak (369°C) is ascribed to hemicellulose and cellulose decomposition, respectively. Above these temperatures, tailing

representing lignin decomposition occurs. After pretreatment at 180°C, the hemicellulose peak is reduced to a shoulder peak because of hemicellulose degradation from HTT. When the temperature is further increased to 200°C and 220°C, the hemicellulose peak disappears because of extensive hemicellulose degradation. Therefore, the hemicellulose peak intensity correlates with the xylose concentration (Table 3-2) in the samples. Conversely, the cellulose peak intensity trend indicates that combined HTT and washing enriches cellulose in resultant hydrochars.

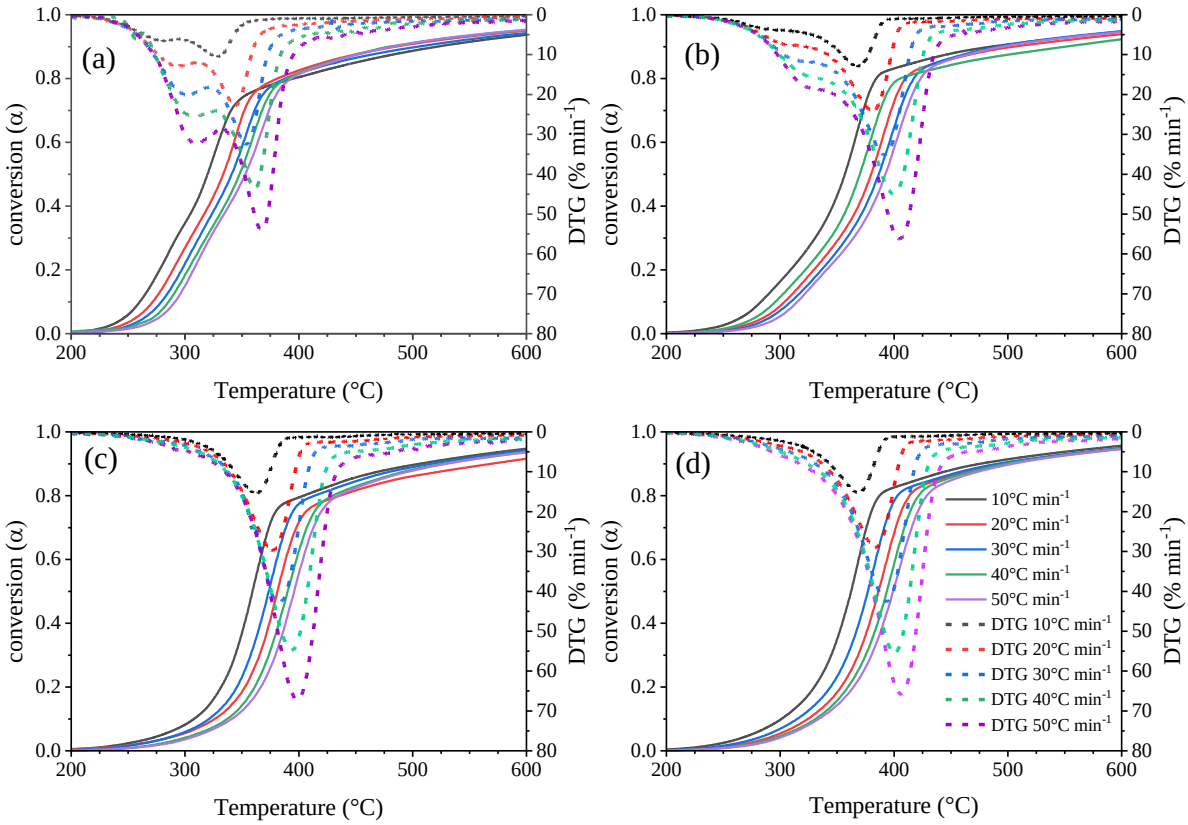

Figure 3-6. TGA conversion and DTG curves for (a) RCF (b) HT180, (c) HT200, and (d) HT220 obtained at heating rates 10, 20, 30, 40, and 50°C min^{-1}

3.3.5 Activation energy

The activation energy (E_α) and conversion extent (α) variation in Figure 3-7 reflects the successive thermo-degradation of lignocellulose components according to their thermal stability and polymerization degree. The Vyazovkin AIC method was used to determine all samples' decomposition kinetics in the conversion range of 0.05–0.80 and temperature range of 150°C–900°C.

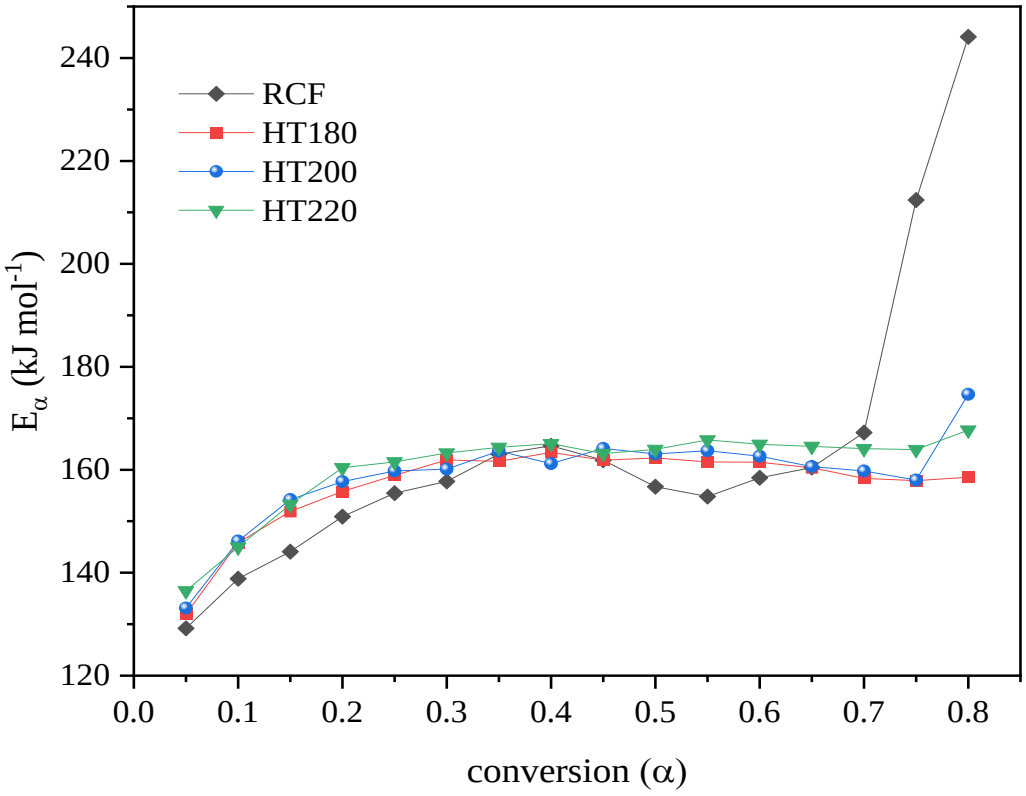

Figure 3-7. Variation of activation energy with conversion calculated using the Vyazovkin AIC method

The apparent E_α variation for RCF can be conveniently divided into three stages, namely, stage I, α = 0.05–0.40, E_α = 150.49 ± 12.35 kJ mol^{-1}; stage II, α = 0.40–0.70, E_α = 159.91 ± 4.39 kJ mol^{-1}; and stage III, α = 0.70–0.80, E_α = 228.25 ± 22.42 kJ mol^{-1}. The expulsion of nonstructural components (extractives) from bone-dry biomass typically initiates the first stage, followed by the scission of hemicellulose side-branches, such as O-acetyl groups to form acetic acid [33]. The increase in E_α in this region indicates parallel reactions during hemicellulose pyrolysis [34]. As the temperature increases, there is cleavage of β-1,4-glucosidic bonds linking hexose and pentose units in the amorphous structured polymer. Before the cleavage of the weakest lignin ether linkages, α-O-4 and β-O-4 at 200°C–250°C [27], a substantial decomposition of lignin propyl side-chains at 180°C occurs [35]. Significant inter-ring dehydration of cellulose occurs during this stage, marking the onset of amorphous cellulose depolymerization because of the weakening of glycosidic bonds. Cellulose depolymerization E_α is constant because of constant decomposition pathways [36,37] and the absence of parallel reactions. However, in stage II, the E_α variation is parabolic because of the catalytic role of AAEMs (which lowers E_α), particularly the most abundant potassium species, where fragmentation reactions for cellulose primary products are likely to be dominant.

Therefore, lighter oxygenated compounds could be enriched at the expense of anhydrosugars. Amorphous cellulose depolymerizes first, followed by crystalline cellulose with a higher degree of polymerization via the cleavage of β-1,4 glycosidic bonds [38]. Beyond α = 0.70, passive pyrolysis of lignin commences with simultaneous charring and release of phenolic compounds. E_α increases because of parallel reactions during lignin thermo-transformation [34]. Here, highly-ordered lignin units linked by thermally stable carbon-carbon linkages (β-1, β-5, and 5-5) are decomposed as the temperature increases beyond 350°C [39]. As the temperature increases, deoxygenation reactions (decarboxylation, decarboxylation, and dehydration) and dehydrogenation intensify, producing low-molecular gases (CO_2, CO, H_2O, and H_2) and lignin-rich char [40].

The same description holds for hydrochar pyrolysis, except for the possible role of AAEMs and solubilized bio-components imposed by pretreatment. After pretreatment, noticeable changes in the E_α variation occur. A reduction in the conversion range for stage I (α = 0.05–0.20) occurs, which is ascribed to hemicellulose degradation imposed by HTT. Simultaneously, cellulose enrichment occurs in stage II (α = 0.20–0.75). In stage I, the average E_α for HT180, HT200, and HT220 is 143.23 ± 10.22, 144.48 ± 10.64, and 144.91 ± 8.38 kJ mol^{-1}, respectively. Note that the second stage for HT180 stretches until α = 0.80. The nearly constant E_α in stage II confirms the absence of parallel reactions, and in the second stage, primary cellulose products, such as levoglucosan, could be prevalent. The average E_α for HT180, HT200, and HT220 in this stage is 160.30 ± 2.20, 162.23 ± 4.31, and 164.06 ± 1.32 kJ mol^{-1}, respectively. According to the monomeric composition of hydrochars, stage I for HT180 can be mostly attributed to residual hemicellulose after pretreatment, whereas for HT200 and HT220, it is mostly attributed to thermally unstable lignin. Residual hemicellulose and nonstructural components contribute to a lesser extent for hydrochars produced at ≥200°C. Therefore, apart from delaying passive pyrolysis, pretreatment in this study only marginally affects the increase in E_α.

3.3.6 Solid-state reaction mechanisms

Experimental plots for RCF and corresponding washed hydrochars vary with conversion and heating rate, indicating the complexity of the pyrolysis mechanism (Figure 3-8). The variation demonstrates that one model cannot entirely describe the progressive degradation of these biomass samples.

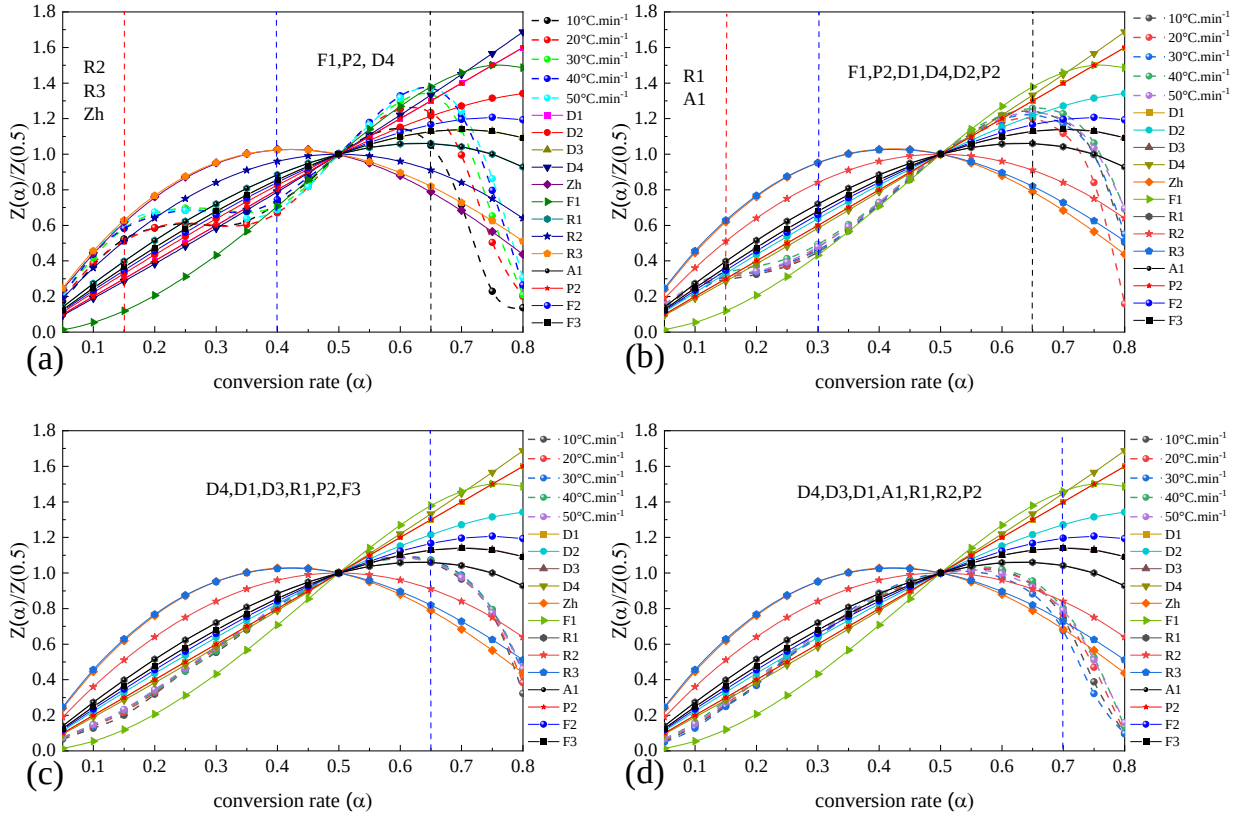

Figure 3-8. Determining the pyrolysis mechanism using Z-master and experimental plots from the Criado method; (a) RCF, (b) HT180, (c) HT200, and (d) HT220

Theoretical or Z-master plots for RCF (Figure 6 (a)) at 10–20°C min^{-1} (α = 0.05–0.15) closely overlap with the R2 theoretical plot, corresponding to second-order random nucleation with two nuclei on an individual particle [35]. However, by increasing the heating rate to 30–50°C min^{-1}, the mechanism is better described by the third-order random nucleation with three nuclei on an individual particle (R3) and the Zhravlev equation in the same conversion range [41].

At all heating rates, in the conversion range α = 0.15–0.40, the experimental plots cross the theoretical plots, indicating a transition for multiple and complex reaction mechanisms [42]. At heating rates of 20–50°C min^{-1} (α = 0.4–0.65), the (F1) first-order reaction model can describe the pyrolysis mechanism. At 10°C min^{-1}, the profile is described by the F1 model up to conversion 0.5, whereas the Ginstlinge–Brounshtein model for three-dimensional diffusion (D4), or power law (P2) describe the range α = 0.5–0.55. The sudden drop in profiles (20–50°C min^{-1}) characterized by poor fitting at conversion greater than 0.65 indicates multiple and complex mechanisms [42]. For 10°C min^{-1}, the complex mechanism starts at α = 0.55.

The pyrolysis profiles for HT180 (Figure 3-8(b)) are near coincident for α = 0.05–0.65, indicating that solid-state reaction mechanisms are unaffected by any appreciable extent at

heating rates equal or less than 50°C min^{-1}. This observation is attributed to the enrichment of bio-components of a higher polymerization degree imposed by hydrothermal carbonization. Between the conversion range of 0.05–0.15, the experimental plots agree with the R1 theoretical plots, corresponding to first-order random nucleation with one nucleus on an individual particle. The Avrami–Erofeev model (A1) also overlaps the experimental plots in the range of 0.05–0.10. In the range α = 0.15–0.30, fitting is poor at all heating rates, indicating the transition of multiple and complex reaction mechanisms. In α = 0.30–0.55, the F1 (first-order) chemical reaction model better describes the degradation profiles. Within the range α = 0.55–0.60, the experimental profiles are more closely inclined to diffusion-reaction models, i.e., one-dimensional (D1) and three-dimensional (D4) described by the Ginstling–Brounshtein equation depending on the heating rate. In the conversion range α = 0.60–0.65, the D2 model describes the experimental plot for the heating rate of 20°C min^{-1}, whereas the other heating rates are closer to the D1 model. The P2 model plot coincides with the D1 model; hence, the P2 model in the conversion range α = 0.60–0.65 can also describe experimental plots other than the 20°C min^{-1}. Beyond α = 0.65, a dramatic drop in depolymerization profiles occurs, coupled with poor fitting, indicating complex reaction mechanisms.

For HT200 (Figure 3-8(c)), degradation profiles at varying heating rates are also at near coincidence because of the same abovementioned reason. However, note the absence of the transition for multiple and complex mechanisms at conversions lower than 0.50. Therefore, hydrothermal pretreatment simplifies the overall pyrolysis mechanism by introducing homogeneity in hydrochars. In conversion ranges α = 0.05–0.35, α = 0.35–0.5, α = 0.5–0.60, and α = 0.6 – 0.65, the Ginstling–Brounshtein equation, one-way transport (D1), three-way transport (Jander model), and first-order random nucleation models (R1) describe the mechanisms, respectively. The P2 and F3 models also closely overlap the experimental plots in the conversion ranges α = 0.30–0.50 and α = 0.50–0.60, respectively. Beyond α = 0.65, like HT180, multiple complex mechanisms are observed.

The degradation behavior of HT220 (Figure 3-8 (d)) is akin to that of HT200, particularly the change in mechanisms regarding the heating rate variance. In the conversion range α = 0.05–0.25, experimental plots are closest to the P2 and D4 mechanisms, whereas the range α = 0.25–0.35 overlaps with D3 and D1 reaction mechanisms. Experimental plots in the range α = 0.35–0.55 closely match the A1 and R1 mechanisms, whereas the second-order random nucleation models (R2) can describe the range α = 0.55–0.70. At conversions greater than 0.70, a

discrepancy exists between the reduced experimental and Z-master plots, indicating complex reaction mechanisms.

By correlating the chemical composition of samples and their corresponding pyrolysis mechanisms, hemicellulose and cellulose thermal degradation follow mostly random nucleation and diffusion-reaction mechanisms, respectively. This inference can explain why random nucleation reactions describe the first stage of RCF and HT180 pyrolysis, whereas diffusion reactions describe the initial stage of HT200 and HT220. Depending on pretreatment intensity, the region for multiple complex reactions below the conversion of 0.5 was either reduced or removed. Therefore, during pretreatment, the overall reaction mechanism is simplified. Furthermore, the mechanisms for coconut fibers became less sensitive to changes in heating rate after pretreatment.

3.3.7 Effect of pretreatment on the composition of volatiles

Fast pyrolysis results of samples exhibited a disparate composition of pyrolysates (Figure 3-9). However, to establish the distinction among the broad spectrum of compounds detected, pyrolysates was classified into carbohydrate and lignin-derived units. Carbohydrate-derivatives (in blue) from hemicellulose and cellulose include compound groups (cyclopentenone, anhydrosugars, pyrone, and furan derivatives, and light oxygenated compounds). Lignin comprises p-hydroxyphenyl, guaiacol, syringol units, and other phenolic compounds were conveniently classified under the same group in this work and designated in red as lignin-derived. Identified but unclassified compounds include trimethylamine and fatty acid derivatives.

The chemical composition of RCF and hydrochar pyrolysates is distinct, with compound groups, such as anhydrosugars and pyrone derivatives not detected for RCF. The absence of anhydrosugars can be attributed to the catalyzing effect of inorganics, such as AAEMs, promoting secondary cracking of primary pyrolysates into low-molecular compounds. Among hydrochar pyrolysates, the chemical composition is the same; however, a significant variance exists in relative proportions of the compound groups. The chemical composition of RCF is marked with a high concentration of light oxygenates (or low-molecular weight aldehydes, ketones, and acids), such as acetic acid, methylglyoxal, and 3-hydroxypropanal. The prevalence of these compounds can be ascribed to but is not limited to thermal dissociation of xylose and associated cleavage of O-acetyl groups [25], compounded by catalyzing secondary

cracking reactions imposed by AAEMs at the expense of primary cellulose products, such as levoglucosan [43].

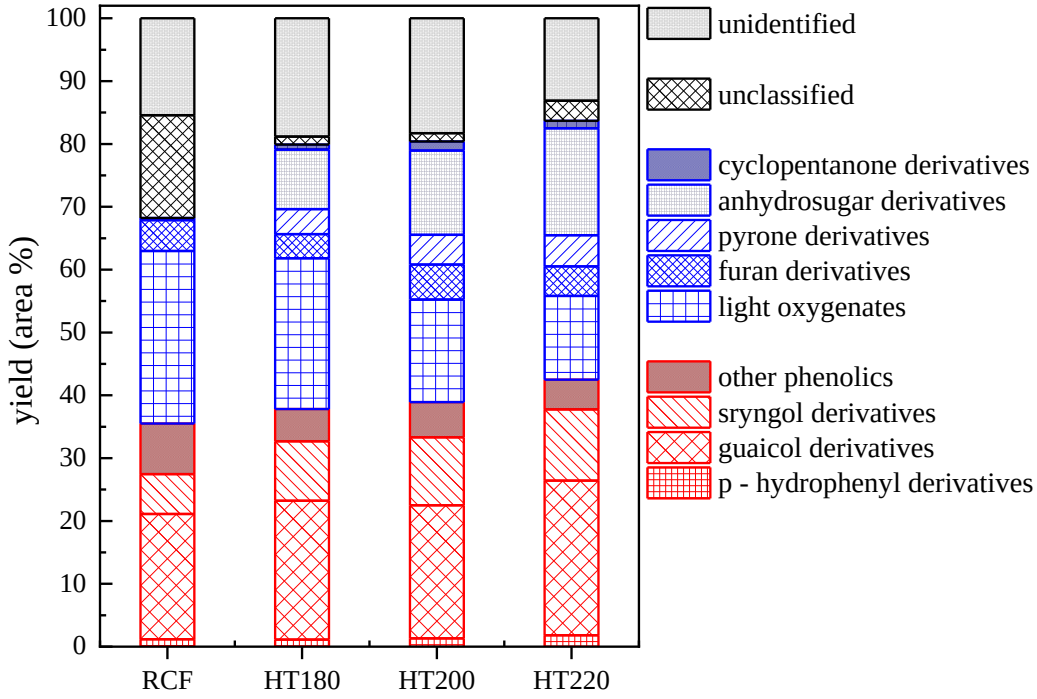

Figure 3-9. Effect of pretreatment intensity on yields of various product groups obtained from the pyrolysis of untreated and differently treated coconut fiber

After pretreatment, anhydrosugars selectivity increase with pretreatment intensity to 9.46, 13.42, and 17.02 area % for HT180, HT200, and HT220, respectively, because of enriched glucose-based carbohydrates with a high polymerization degree. These polymers are typically depolymerized into anhydrosugars and furan derivatives via the scission of glycosidic bonds [44]. Correspondingly, light oxygenates decreased from 27.45 area % to 24.02, 16.33, and 13.32 area % for HT180, HT200, and HT220, respectively, because of suppressing fragmentation reactions during demineralization. However, pretreatment enhanced the selectivity of cyclopentenone and pyrone derivatives. Furthermore, pretreatment enhanced the selectivity of high-molecular-weight phenolic compounds from 35.51 area % to 37.81, 38.91, and 42.50 area % for HT180, HT200, and HT220, respectively. Therefore, pretreatment favored primary pyrolysis products by suppressing fragmentation reactions posed by demineralization.

3.4 Conclusion

This study highlighted the effect of HTT (180°C–220°C) on K demineralization and pyrolysis behavior. The high-heating value (HHV) of RCF is 17.9 MJ kg^{-1}; however, the HHV of resultant solids improved by 9.7%–20.1% after hydrothermal treatment. RCF comprises ~76%

water-soluble, ~19% ion-exchangeable, and ~5% acid-soluble K species. All water-soluble and ion-exchangeable K could be removed after washing hydrochars produced at 180°C–200°C. However, at 220°C, a significant physicochemical structure evolution reduced the degree of K demineralization. The potassium removal efficiency of 93% was achieved. After pretreatment, the activation energy marginally increased in the conversion range of 0.05–0.80; however, charring was delayed. The mechanism changed according to the chemical composition of the samples. Typically, xylose-rich samples were described by order-based reaction mechanisms and followed by a region for multiple and complex mechanisms at conversions below 0.4. However, xylose-lean samples were initiated by diffusion-reaction mechanisms, and the complex region was eliminated. Therefore, pretreatment simplified the overall mechanism of coconut fibers. Pretreatment increased the selectivity of phenolic compounds and anhydrosugars (levoglucosan). Anhydrosugars were enriched by suppressing fragmentation reactions catalyzed by potassium.

References

[1] Raghavan K. Biofuels From Coconuts. 2010.

[2] Hungwe D, Khushbouy R, Ullah S, Lu D, Yoshikawa K, Takahashi F. Effect of Tire-Char Ash on the Extent of Synergy during CO_2 Cogasification with Hydrochar from Potassium-Rich Coconut Fiber. Energy & Fuels 2020;34:8110–9. https://doi.org/10.1021/acs.energyfuels.0c00895.

[3] Almeida TM, Bispo MD, Cardoso ART, Migliorini M V., Schena T, De Campos MC V., et al. Preliminary studies of bio-oil from fast pyrolysis of coconut fibers. J Agric Food Chem 2013;61:6812–21. https://doi.org/10.1021/jf401379s.

[4] Schena T, Lazzari E, Primaz C, Canielas Krause L, Machado ME, Bastos Caramão E. Upgrading of coconut fibers Bio-Oil: An investigation by Gc×Gc/Tofms. J Environ Chem Eng 2020;8:103662. https://doi.org/10.1016/j.jece.2020.103662.

[5] Inseemeesak B, Areeprasert C. Fiber extraction and energy recovery from Cocos nucifera Linn mesocarp residues employing steam explosion and anaerobic digestion. Ind Crops Prod 2020;147:112180. https://doi.org/10.1016/j.indcrop.2020.112180.

[6] Niu Y, Tan H, Hui S. Ash-related issues during biomass combustion: Alkali-induced slagging, silicate melt-induced slagging (ash fusion), agglomeration, corrosion, ash utilization, and related countermeasures. Prog Energy Combust Sci 2016;52:1–61. https://doi.org/10.1016/j.pecs.2015.09.003.

[7] Namkung H, Lee YJ, Park JH, Song GS, Choi JW, Kim JG, et al. Influence of herbaceous biomass ash pre-treated by alkali metal leaching on the agglomeration/sintering and corrosion behaviors. Energy 2019;187:115950. https://doi.org/10.1016/j.energy.2019.115950.

[8] Areeprasert C, Zhao P, Ma D, Shen Y, Yoshikawa K. Alternative solid fuel production from paper sludge employing hydrothermal treatment. Energy and Fuels 2014;28:1198–206. https://doi.org/10.1021/ef402371h.

[9] Novianti S, Nurdiawati A, Zaini IN, Prawisudha P, Sumida H, Yoshikawa K. Low-potassium Fuel Production from Empty Fruit Bunches by Hydrothermal Treatment Processing and Water Leaching. Energy Procedia 2015;75:584–9. https://doi.org/10.1016/j.egypro.2015.07.460.

[10] Theppitak S, Hungwe D, Ding L, Xin D, Yu G, Yoshikawa K. Comparison on solid biofuel production from wet and dry carbonization processes of food wastes. Appl Energy 2020;272:115264. https://doi.org/10.1016/j.apenergy.2020.115264.

[11] Reza MT, Lynam JG, Uddin MH, Coronella CJ. Hydrothermal carbonization: Fate of

inorganics. Biomass and Bioenergy 2013;49:86–94. https://doi.org/10.1016/j.biombioe.2012.12.004.

[12] Novianti S, Nurdiawati A, Zaini IN, Sumida H, Yoshikawa K. Hydrothermal treatment of palm oil empty fruit bunches: an investigation of the solid fuel and liquid organic fertilizer applications. Biofuels 2016;7:627–36. https://doi.org/10.1080/17597269.2016.1174019.

[13] Nurdiawati A, Novianti S, Zaini IN, Nakhshinieva B, Sumida H, Takahashi F, et al. Evaluation of Hydrothermal Treatment of Empty Fruit Bunch for Solid Fuel and Liquid Organic Fertilizer Co-Production. vol. 79. Elsevier B.V.; 2015. https://doi.org/10.1016/j.egypro.2015.11.469.

[14] Mosqueda A, Wei J, Medrano K, Gonzales H, Ding L, Yu G, et al. Co-gasification reactivity and synergy of banana residue hydrochar and anthracite coal blends. Appl Energy 2019. https://doi.org/10.1016/j.apenergy.2019.05.008.

[15] Tan C, Saritpongteeraka K, Kungsanant S, Charnnok B, Chaiprapat S. Low temperature hydrothermal treatment of palm fiber fuel for simultaneous potassium removal, enhanced oil recovery and biogas production. Fuel 2018;234:1055–63. https://doi.org/10.1016/j.fuel.2018.07.137.

[16] Nakason K, Panyapinyopol B, Kanokkantapong V, Viriya-empikul N, Kraithong W, Pavasant P. Hydrothermal carbonization of unwanted biomass materials: Effect of process temperature and retention time on hydrochar and liquid fraction. J Energy Inst 2018;91:786–96. https://doi.org/10.1016/j.joei.2017.05.002.

[17] Jain A, Balasubramanian R, Srinivasan MP. Hydrothermal conversion of biomass waste to activated carbon with high porosity: A review. Chem Eng J 2016;283:789–805. https://doi.org/10.1016/j.cej.2015.08.014.

[18] Ghalibaf M, Ullah S, Alén R. Fast pyrolysis of hot-water-extracted and soda-AQ-delignified okra (Abelmoschus esculentus) and miscanthus (miscanthus x giganteus) stalks by Py-GC/MS. Biomass and Bioenergy 2018;118:172–9. https://doi.org/10.1016/j.biombioe.2018.09.001.

[19] Ullah S, Pakkanen H, Lehto J, Alén R. A comparable study on the hot-water treatment of wheat straw and okra stalk prior to delignification. Biomass Convers Biorefinery 2018;8:413–21. https://doi.org/10.1007/s13399-018-0306-x.

[20] Liaw SB, Wu H. Leaching characteristics of organic and inorganic matter from biomass by water: Differences between batch and semi-continuous operations. Ind Eng Chem Res 2013;52:4280–9. https://doi.org/10.1021/ie3031168.

[21] Khoshbouy R, Takahashi F, Yoshikawa K. Preparation of high surface area sludge-based activated hydrochar via hydrothermal carbonization and application in the removal of basic dye. Environ Res 2019;175:457–67. https://doi.org/10.1016/j.envres.2019.04.002.

[22] Hungwe D, Ding L, Khoshbouy R, Yoshikawa K, Takahashi F. Kinetics and Physicochemical Morphology Evolution of Low and High-Ash Pyrolytic Tire Char during CO_2 Gasification. Energy and Fuels 2020;34:118–29. https://doi.org/10.1021/acs.energyfuels.9b03043.

[23] Criado JM. Kinetic analysis of DTG data from master curves. Thermochim Acta 1978;24:186–9. https://doi.org/10.1016/0040-6031(78)85151-X.

[24] Channiwala SA, Parikh PP. A unified correlation for estimating HHV of solid, liquid and gaseous fuels. Fuel 2002;81:1051–63. https://doi.org/10.1016/S0016-2361(01)00131-4.

[25] Wang S, Dai G, Yang H, Luo Z. Lignocellulosic biomass pyrolysis mechanism: A state-of-the-art review. Prog Energy Combust Sci 2017;62:33–86. https://doi.org/10.1016/j.pecs.2017.05.004.

[26] Yoo CG, Ragauskas AJ. Opportunities and Challenges of Lignin Utilization. Lignin Util. Strateg. From Process. to Appl. Part 1 - Oppor. Challenges Lignin Util., American Chemical Society; 2021, p. 1–12. https://doi.org/10.1021/bk-2021-1377.ch001.

[27] Chu S, Subrahmanyam A V, Huber GW. The pyrolysis chemistry of a β-O-4 type oligomeric lignin model compound. Green Chem 2013;15:125–36. https://doi.org/10.1039/C2GC36332A.

[28] Teo CC, Tan SN, Yong JWH, Hew CS, Ong ES. Pressurized hot water extraction (PHWE). J Chromatogr A 2010;1217:2484–94. https://doi.org/10.1016/j.chroma.2009.12.050.

[29] Zevenhoven M, Yrjas P, Skrifvars BJ, Hupa M. Characterization of ash-forming matter in various solid fuels by selective leaching and its implications for fluidized-bed combustion. Energy and Fuels 2012;26:6366–86. https://doi.org/10.1021/ef300621j.

[30] Girisuta B, Janssen LPBM, Heeres HJ. Green chemicals: A kinetic study on the conversion of glucose to levulinic acid. Chem Eng Res Des 2006;84:339–49. https://doi.org/10.1205/cherd05038.

[31] Titirici MM, White RJ, Falco C, Sevilla M. Black perspectives for a green future: Hydrothermal carbons for environment protection and energy storage. Energy Environ

Sci 2012;5:6796–822. https://doi.org/10.1039/c2ee21166a.

[32] Kumar H, Alén R, Sahoo G. Characterization of Hardwood Soda-AQ Lignins Precipitated from Black Liquor through Selective Acidification. BioResources 2016;11:9869–79. https://doi.org/10.15376/biores.11.4.9869-9879.

[33] Wang S, Ru B, Lin H, Luo Z. Degradation mechanism of monosaccharides and xylan under pyrolytic conditions with theoretic modeling on the energy profiles. Bioresour Technol 2013;143:378–83. https://doi.org/10.1016/j.biortech.2013.06.026.

[34] Vyazovkin S V., Lesnikovich AI. An approach to the solution of the inverse kinetic problem in the case of complex processes. Part 1. Methods employing a series of thermoanalytical curves. Thermochim Acta 1990;165:273–80. https://doi.org/10.1016/0040-6031(90)80227-P.

[35] Mallick D, Poddar MK, Mahanta P, Moholkar VS. Discernment of synergism in pyrolysis of biomass blends using thermogravimetric analysis. Bioresour Technol 2018;261:294–305. https://doi.org/10.1016/j.biortech.2018.04.011.

[36] Yuan X, He T, Cao H, Yuan Q. Cattle manure pyrolysis process: Kinetic and thermodynamic analysis with isoconversional methods. Renew Energy 2017;107:489–96. https://doi.org/10.1016/J.RENENE.2017.02.026.

[37] Zhang S, Zhu S, Zhang H, Liu X, Zhang H. Evaluation of pyrolysis behavior and products properties of rice husk after combined pretreatment of washing and torrefaction. Biomass and Bioenergy 2019;127:105293. https://doi.org/10.1016/j.biombioe.2019.105293.

[38] Wang Z, McDonald AG, Westerhof RJM, Kersten SRA, Cuba-Torres CM, Ha S, et al. Effect of cellulose crystallinity on the formation of a liquid intermediate and on product distribution during pyrolysis. J Anal Appl Pyrolysis 2013;100:56–66. https://doi.org/10.1016/j.jaap.2012.11.017.

[39] Kawamoto H, Horigoshi S, Saka S. Pyrolysis reactions of various lignin model dimers. J Wood Sci 2007;53:168–74. https://doi.org/10.1007/s10086-006-0834-z.

[40] Sharma RK, Wooten JB, Baliga VL, Lin X, Chan WG, Hajaligol MR. Characterization of chars from pyrolysis of lignin. Fuel 2004;83:1469–82. https://doi.org/10.1016/j.fuel.2003.11.015.

[41] Vlaev L., Markovska I., Lyubchev L. Non-isothermal kinetics of pyrolysis of rice husk. Thermochim Acta 2003;406:1–7. https://doi.org/10.1016/S0040-6031(03)00222-3.

[42] Song F, Li T, Zhang J, Wang X, Bai Y, Giesy JP, et al. Novel Insights into the

Kinetics, Evolved Gases, and Mechanisms for Biomass (Sugar Cane Residue) Pyrolysis. Environ Sci Technol 2019;53:13495–505. https://doi.org/10.1021/acs.est.9b04595.

[43] Hwang H, Oh S, Cho TS, Choi IG, Choi JW. Fast pyrolysis of potassium impregnated poplar wood and characterization of its influence on the formation as well as properties of pyrolytic products. Bioresour Technol 2013;150:359–66. https://doi.org/10.1016/j.biortech.2013.09.132.

[44] Wu S, Shen D, Hu J, Zhang H, Xiao R. Role of β-O-4 glycosidic bond on thermal degradation of cellulose. J Anal Appl Pyrolysis 2016;119:147–56. https://doi.org/10.1016/j.jaap.2016.03.006.

Chapter 4: **Effect of inherent tire ash on co-gasification of biomass/hydrochar and tire char**

Abstract

The influence of inherent tire char ash during co-gasification with coconut hydrochar prepared at different intensities was investigated using thermogravimetric analysis to ascertain the extent to which synergistic interaction, reactivity, and activation energy reduction were altered. Moreover, the nature of interactions during the pyrolysis stage of co-gasification were determined using a two-stage fixed bed reactor. In the pyrolysis stage, bio-volatiles were subjected to cracking/deoxygenation reactions, namely, dehydration, decarboxylation, and decarbonylation reactions. The deoxygenation reactions are more pronounced for tire tread (TT) than sidewall (SW) char because of the high concentration of Zn-containing minerals in tire tread. High-ash TT and low-ash SW both exhibited enhanced synergy, reactivity, and activation reduction upon co-gasification with hydrochars; however, the extent of promotion was more pronounced in SW-hydrochar blends. This difference was caused by the inhibiting nature of TT inherent ash, particularly the role of Si-containing compounds. Inhibition in TT-hydrochar blends was mainly due to the promotion of alkaline and alkaline earth metal transformation into inactive silicates, and to a lesser extent, the mass transfer effect caused by accumulated ash, especially at conversions higher than 70%. The extent of enhancement correlated well with the concentration of available alkaline and alkaline earth metals. The findings may be useful in justifying the exclusion of high ash tire char as gasification feedstock to mitigate ash-related problems.

4.1 Introduction

Hitherto, the impetus to reduce dependency on fossil fuels by exploring alternative, green and (or) sustainable energy sources such as biomass [1,2] waste tire [3,4] and municipal solid waste [5] has intensified, leading to the exploitation of these alternatives in already existing coal-based gasification facilities [6]. However, the commercialization of unary gasification of these candidate fuel-sources is thwarted by several critical fuel quality issues and operational problems. Sole biomass gasification bottlenecks include and are not limited to low bulk and carbon density, high moisture content, mineral matter, irregular morphology, and tar generation [7,8]. Hydrothermal treatment (HT) is one of the pre-treatment methods used to address some of the limitations of biomass utilization, particularly better solid dewatering performance, improving energy density, and homogenization of solid fuel morphology.

Hydrothermal treatment is the thermochemical conversion of biomass into an energy-dense carbonaceous solid using an aqueous medium operated under subcritical conditions [10]. The densified solid, also known as hydrochar, is a result of biomass transformation via chemical reactions which include decarboxylation, decarbonylation, dehydration, polymerization, re-condensation, aromatization, and hydrolysis [11]. Simultaneously, the process extracts water-soluble ash-forming minerals from biomass into the aqueous phase, thus reducing the alkaline index of resultant hydrochar [12]. Consequently, the tendency for ash fouling and slagging is diminished [13]. Intensive HT conditions can yield chars similar to lignite coal at best, beyond which, more severe conditions render the process uneconomical. Furthermore, the energy density of hydrochar is significantly lower than that of higher rank coals used in gasification facilities, therefore it is imperative to improve the energy density of hydrochar by co-utilization with high calorific carbonaceous material such as waste tire.

Waste tire is an energy-dense (30-40 MJ/kg) carbonaceous material [3] with a heating value higher than that coal [14]. Nascent pyrolytic tire char is relatively inert under CO_2 gasification conditions [6,15] owing to the graphitic structure and a deficiency in reaction-promoting heteroatoms hence requires harsh reaction conditions [16,17]. On the other hand, lignocellulose biomass has ample heteroatoms and catalytic species in the form of alkaline and alkaline earth metals (AAEMs), these are known to significantly improve reactivity [17–19]. Although biomass can greatly improve gasification reactivity, it inevitably produces problematic condensable organic compounds referred to as tar. Tar can be reduced and (or) eliminated by carbonaceous chars [18], reforming performance is significantly enhanced by doping with transitional metals [20,21]. Zinc-rich tire char is also exploited as an in-situ or ex-situ tar

reforming catalyst during co-gasification [22, 23]. Co-gasification of biomass and waste tire is therefore complementary because the latter can sequestrate the demerits of the former, and vice versa. A deep understanding of the nature of interactions during co-gasification is, therefore, by no means a trivial matter.

Research on co-gasification of waste tire and biomass has not garnered much attention [4], to the best of the authors' knowledge only one research group reported on the isothermal and non-isothermal kinetics of CO_2 co-gasification with several biomass residues [16,17]. They confirmed that co-gasification improved process thermodynamics and synergistic interaction, owing to the catalytic role of AAEMs. It is worth mentioning that these previous studies were restricted to one non-specified part of a tire; however, tires are composed of low-ash sidewall (SW) and high-ash tire tread (TT) components. This heterogeneity is not accounted for in co-gasification studies. It follows that the effect of inherent ash on tire-biomass interaction requires investigation to attain a more holistic understanding of synergistic or antagonistic effects during gasification. Our previous study compared the effect of inherent tire ash on the physicochemical evolution of SW and TT char and found that TT formed silica-based ash clusters, which inhibited gasification through an increase of mass transfer effects and suppression of structural development [24]. SW did not exhibit any inhibition even at near-completion conversion. By inference, such phenomena may have a deleterious effect on co-gasification. For a better understanding of the effect of inherent ash during co-gasification, the mechanism of catalysis requires reviewing.

The proposed mechanism of catalysis is initiated by AAEMs migration from biomass to the tire char. Subsequently, there is deposition and preferential accommodation on and within carbon matrix imperfections resulting in the formation of swelling graphitic intercalation compounds that strain carbon bonds and ease bond breaking [25]. In addition, the degree of graphitization [12] and aromatic ring condensation is suppressed [27], and consequently, the gasification reaction is promoted via a reduction in activation energy. It is, therefore, reasonable to infer that migration and accessibility of the char matrix by catalytic species has a profound effect on the extent and nature of the interaction. High-ash chars can reduce carbon matrix accessibility by intercepting AAEMs and (or) encapsulating the carbon matrix and thus reduce the extent of interaction [24]. Based on this hypothesis, it is worth investigating and quantitatively evaluating the effect of different ash content on synergy or inhibition. Results from such a study are key in justifying the necessity of tire pre-handling protocols to mitigate possible ash-related issues such as incomplete carbon conversion and ash fusion.

The multistep co-gasification process was reviewed to determine the nature of interactions during the co-gasification of coconut hydrochar and tire chars. The proximate analysis shows that hydrochars comprise at least 70% volatile matter while tire char does not have any volatile matter. Preliminary experiments for gasification of individual treated/untreated coconut fiber and tire are shown in the figure below.

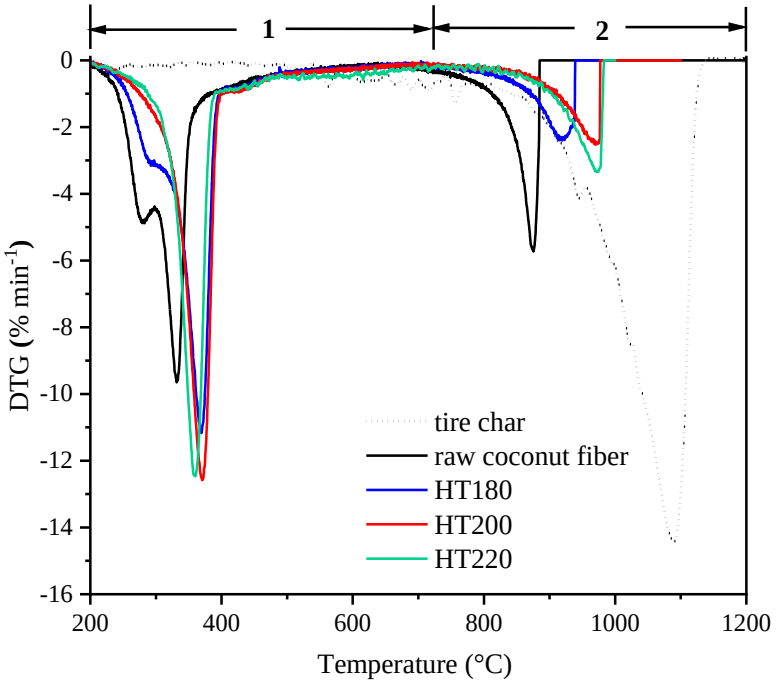

Figure 4-1. TG and DTG curves of tire char, and hydrochars at the heating rate of 10°Cmin^{-1}

According to Figure 4-1, the co-gasification process under non-isothermal conditions can be divided into the following steps;

1. When temperature increases, bio-samples release volatiles in the pyrolysis stage, as shown by the prominent peaks between the temperature range 300-400°C. At the same time, tire char does not exhibit any devolatilization because the char is formed at a much higher pyrolysis temperature.
2. After devolatilization, the hydrochar volatiles interacts with the hot tire char particles.
3. Bio-char formed after devolatilization is then gasified in the temperature range 850-1000°C; consequently, inherent mineral matter in biomass is released and released onto hot tire char, which reacts at a higher temperature as shown by the peak at 1100°C.
4. Finally, the mineral-laden tire char reacts with CO_2 and is transformed into syngas.

These four stages can be divided into the pyrolysis stage [steps 1 and 2] and the gasification stage [steps 3 and 4]. This chapter considers these stages separately to determine the nature of interactions and their effect on the overall gasification process. Emphasis is placed on how inherent tire mineral content affects the nature or extent of interactions during gasification.

In light of this discussion, this chapter presents the co-gasification of tire chars of different ash composition with hydrochars from potassium-rich coconut fiber to gain insights on the effect of AAEM concentration on the extent of synergy, reactivity and reduction of activation energy and to delineate the impact of inherent tire ash on the same. Moreover, the interactions that occur in the first stage of pyrolysis are determined using a two-staged fixed bed reactor.

4.2 Materials and Methods

4.2.1 Sample Preparation

The detailed preparation and characterization of pyrolytic tire char and hydrochar are presented in the previous chapters. Tire chars used in this section are the sidewall (SW) and the tire tread (TT) char. Hydrochars produced at 180°C, 200°C and 220°C herein tagged HT180, HT200 and HT220, respectively were used. The chemical analysis of the and hydrochars is presented in previous chapters.

4.2.2 Char preparation

Pyrolysis experiments were carried out in an electric reactor; a detailed description of the equipment is reported elsewhere. [28] Chars were prepared in a pyrolysis reactor operated at a temperature of 950°C, and the samples were held for 30 minutes to ensure complete devolatilisation. All samples were ground and sieved to a particle size of less than 105 µm. Pyrolyzed hydrothermally treated coconut fiber prepared at 180, 200, and 220 °C was labeled HT180P, HT200P, and HT220P, respectively.

4.2.3 Chemical and Physical Analysis

Char samples' morphological surface characteristics were determined by scanning electron microscopy (SEM: JSM-6610LA, JEOL Ltd. Japan). The Raman spectra of tire char samples were determined by a NRS-4100 Raman spectroscopy (JASCO, Japan) employing a laser beam of wavelength 532 nm and 10 cm^{-1} resolutions. Spectra of wavenumber range 800-2000 cm^{-1} were recorded. The surface area of pyrolyzed chars was measured using an ASAP 2020 analyzer by N_2 gas adsorption method at 77.15 K for pores with a diameter range from 2 nm to 200 nm. The Brunauer–Emmet–Teller (BET) model was used to calculate the specific surface

areas of the samples. Water-soluble and ion exchangeable cationic species of pyrolyzed samples were determined using chemical fractionation analysis [29], and AAEM concentration was measured by an inductively coupled plasma optical emission spectrometer (ICPE-9000, Shimadzu, Japan).

4.2.4 Pyrolysis experiments

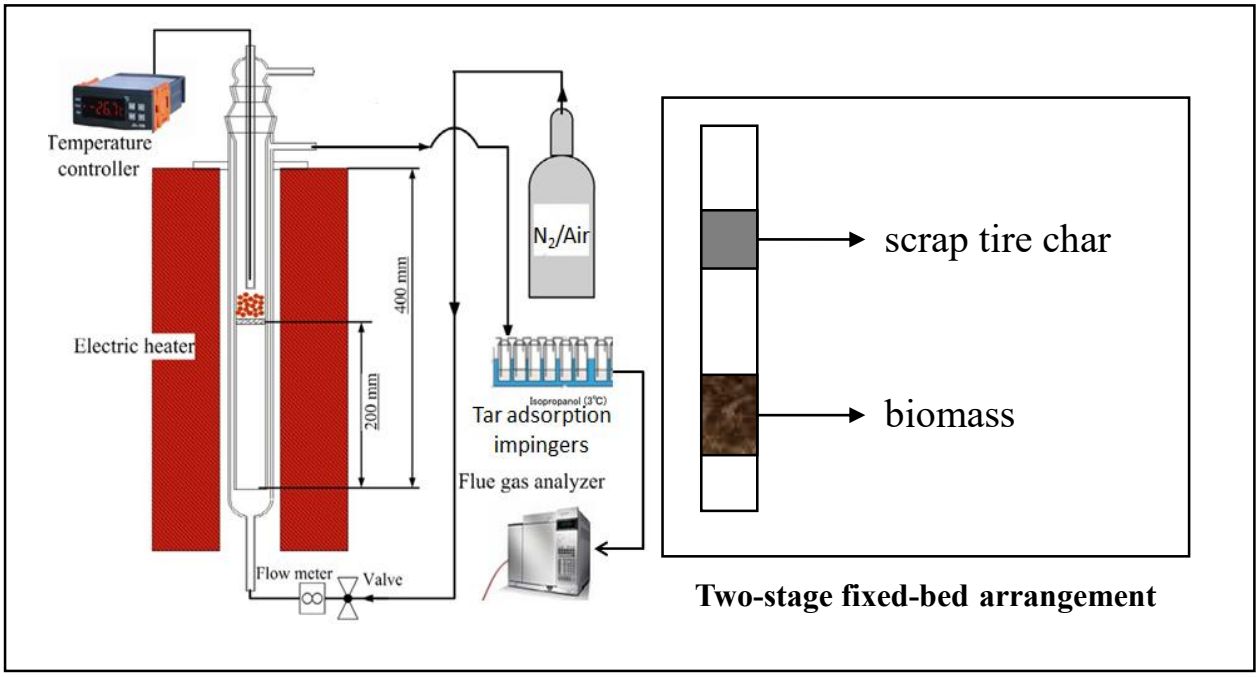

Figure 4-2. Schematic diagram of the two-stage fixed-bed pyrolysis reactor.

A two-stage fixed bed reactor was used to determine the nature of interactions in the pyrolysis stage, however prior this, tire and biomass was mixed. First, a bed of tire char was spread evenly on top of a biomass bed as depicted in Figure 4-2, and N_2 purging gas was introduced from the bottom of the reactor at 600 mL/min. For each experimental run, 50g of biomass and tire char of ratio 0-50 wt% on biomass weight was used. For the pyrolysis stage, only HT180 was used as the model biomass for determining the nature of interactions. The reactor was heated from ambient conditions to 600°C at a heating rate of 10°C/min and held for 20 minutes to ensure complete biomass devolatilization. The volatiles from the biomass were condensed using a series of impinge trains with dry ice/water as the cooling agent. Incondensable gases emerging from the train were then analyzed using a GC analyzer to quantify H_2, CO, CO_2, and CH_4. Water content in the condensable tar was quantified using a Karl Fischer volumetric titrator. All experimental runs were carried out in triplicate to ensure reproducibility.

4.2.5 Gasification experimental procedure

Char blends were prepared by mixing pyrolytic tire char (TC) and hydrochar at equal proportions. The blends were labeled accordingly; for example, a mixture of pyrolyzed SW and HT180P was tagged SW-HT180P. Experimental runs were initiated by loading an 8.0 ± 0.5 mg sample in an alumina crucible and heating to a target temperature at 20 °C/min under N_2 (80 mL/min). The sample was held at target temperature for 5 minutes to ensure temperature equilibration; after that, inert gas was switched to high-purity CO_2 (150 mL/min) to initiate gasification. All experiments were done in triplicate. Semichars were prepared by interrupting gasification TGA tests at times corresponding to appropriate conversion, this was achieved by switching CO_2 flow for N_2 to stop the reaction.

4.2.6 Data processing

Raw mass-loss data was converted to conversion-time data by the following equation,

$$x = \frac{m_0 - m_t}{m_0 - m_a} \tag{4-1}$$

where m_0 is the initial mass of samples, m_t is the instantaneous sample mass at time t and m_a is ash mass. The existence of synergistic/ inhibition effects is determined by comparing non-interactive theoretical conversion and experimental conversion. The theoretical conversion was calculated according to Equation 4-2; [30]

$$x_{cal} = \frac{F_{TC}\left(m_{TC,0} - m_{TC,t}\right) + F_{HT}\left(m_{HT,0} - m_{HT,t}\right)}{F_{TC}\left(m_{TC,0} - m_{TC,a}\right) + F_{HT}\left(m_{HT,0} - m_{HT,a}\right)} \tag{4-2}$$

where F_{TC} and F_{HT} is tire char and hydrochar mass fractions in the blended chars, respectively.

4.2.7 Determination of activation energy

The activation energy can be obtained by using an isoconversional method [31] and the derivation is presented below. The rate law is given by;

$$r = \frac{dx}{dt} = k(T)\, f(x) \tag{4-3}$$

where $f(x)$ is a mathematical expression of a suitable reaction model, $k(T)$ is the rate constant at temperature T. The reaction rate expressed as a function of temperature is described by the Arrhenius equation given by;

$$k = k_0 e^{-\left(\frac{E_A}{RT}\right)} \tag{4-4}$$

where E_A is the activation energy (J/mol), k_0 is the frequency factor in min^{-1}, R is the ideal gas constant $(8.314\ J/mol\ K)$, T is temperature in kelvin.

Equation 4-3 is solved by integration of separated variables;

$$\int_0^x \frac{dx}{f(x)} = G(x) = k_x(T)t_x(T) \tag{4-5}$$

where k_x and t_x is the rate constant (min^{-1}) and residence time (min) at a specific conversion x. Combining equations 4-4 and 4-5 and solving yields

$$\ln[t_x(T)] = \alpha + \frac{E_A}{RT} \tag{4-6}$$

where $\alpha = \ln G(x) - lnk_0$, is a constant at a specified conversion. The activation energy is calculated from the gradient of ln (t_x) against 1/T plots at varying conversion levels.

4.3 Results and Discussion

4.3.1 Interaction of biomass volatiles and tire char of different ash content

Figure 4-4 shows that when biomass is mixed with tire char, there is a simultaneous reduction in tar generation and increased water and gas production (CO_2, CO, and CH_4). Gas evolution and water production can be explained with reference to the biomass pyrolysis mechanism [32] shown in the figure below.

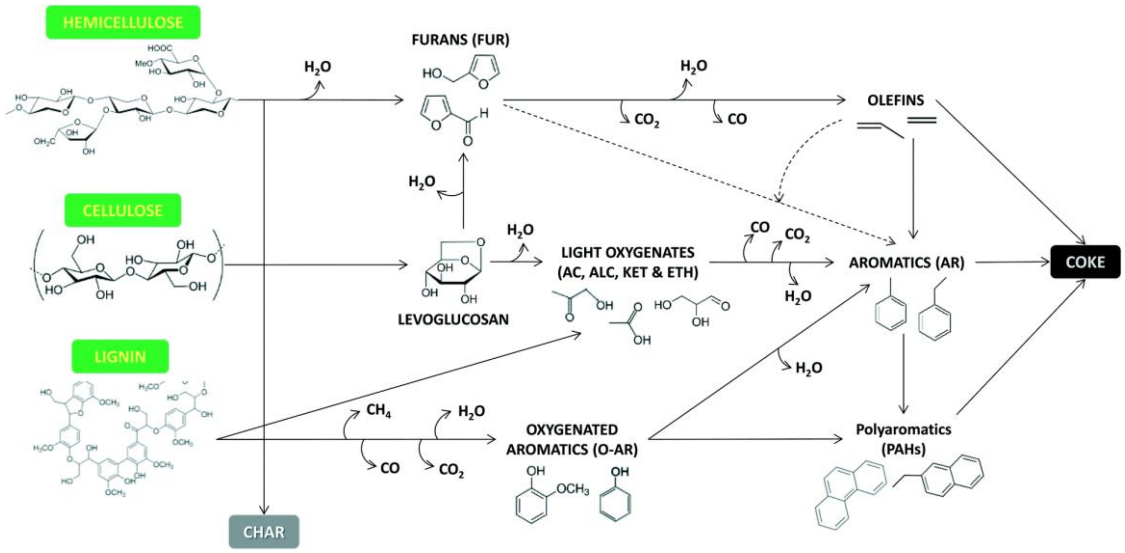

Figure 4-3. Illustration of biomass pyrolysis mechanism

Tar generation reduction indicates that waste tire char has tar reforming properties. Tire tread has a higher tar reforming performance compared sidewall char. When only biomass is pyrolyzed, experimental results are highly reproducible, as shown by the low degree of variance. Conversely, mixed tire and hydrochar exhibited a high variance (indicated by wide error bars), attributed to poor mixing before pyrolysis.

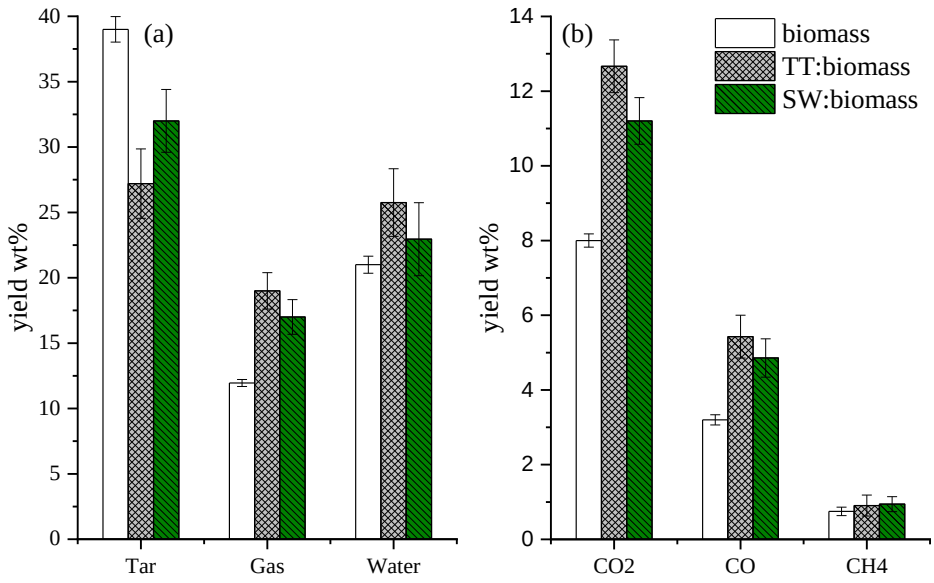

Figure 4-4. Pyrolysis products of biomass only, (a) biomass with 50 wt% tyre tread char and (b) biomass with 50 wt% sidewall char

Due to the challenges in achieving a homogeneous mixture, there are two extremes that can be achieved; (1) when biomass particles are placed on top of tar char, the interaction of bio-volatiles is minimized, and (2) if the arrangement is opposite the interaction between volatiles and tire char is maximized. Therefore, to ensure control of how long volatiles interacts with tire chars and to highlight the nature of these interactions in an approach that is both reproducible and repeatable, the authors resolved to employ a two-stage arrangement of biomass and tire char to maximize the interaction between volatiles and tire char. In this manner, the variance of experimental results is reduced.

Figure 4-5 and 4-6 present the results for the pyrolysis of biomass in a two-staged arrangement with waste tire char at different loading proportions ranging from 0 to 50wt%. According to these figures, tar yield reduces from 39 wt% to 24 wt% for TT 29.5 wt% for SW at 50wt% tire loading. Conversely, the gas yield increases from 11.95 wt% to 21 wt% for TT and 19.2 wt% for SW. Similarly, water generation increases from 21 wt% to 29.5 wt% for TT and 25 wt%

for SW. Gas analysis results show that the most abundant gases produced in the pyrolysis stage are CO_2 and CO. CH_4 was detected but only in small amounts relative to other gases. The decrease incondensable volatiles (tar) can be attributed to the preferential cracking of heavy hydrocarbons into smaller fragments and gas. This decrease is more pronounced for high-ash tire tread char than low-ash char due to Zn-containing minerals. It is widely reported that transitional metals play a catalytic role in tar reforming reactions [32]. The increase in water generation indicates that tire char intensifies dehydration reactions during catalytic cracking of bio-volatiles. It is also demonstrated that as the tire proposition is increased the tar reforming performance is also enhanced.

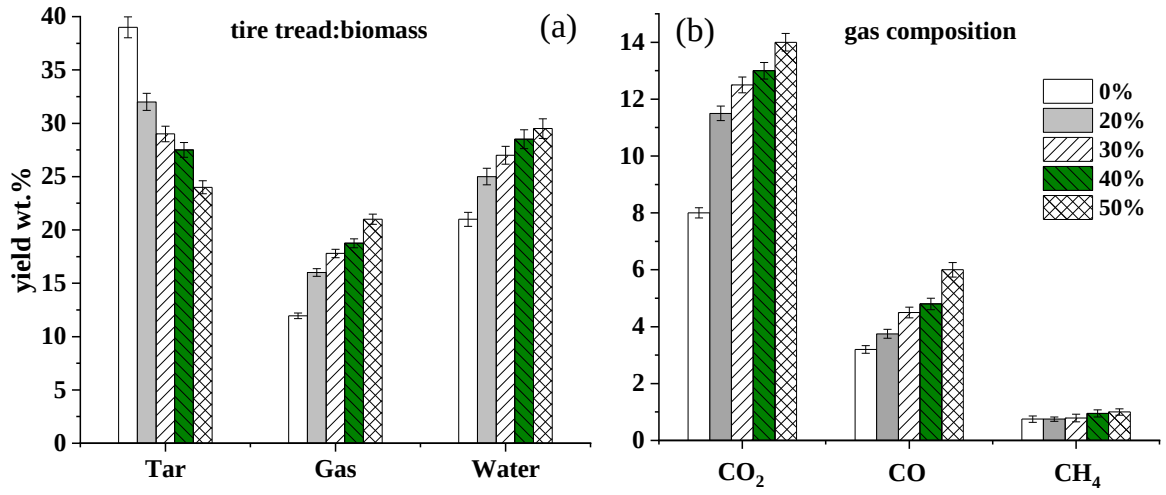

Figure 4-5. Catalytic pyrolysis of biomass at different tire tread char to biomass ratios (a) Overall pyrolysis distribution and (b) Yield distribution of gas compositions

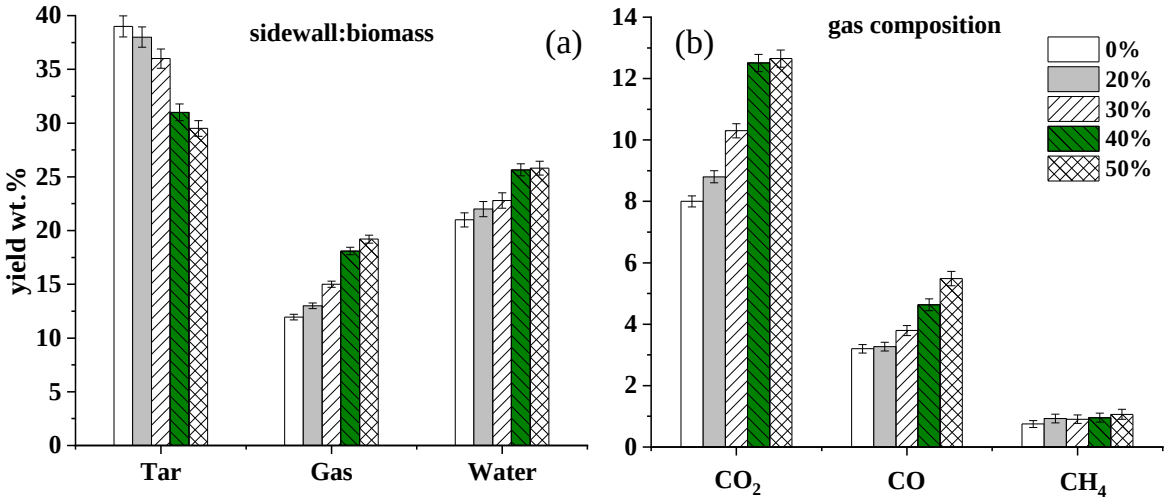

Figure 4-6. Catalytic pyrolysis of biomass at different sidewall char to biomass ratios (a) Overall pyrolysis distribution and (b) Yield distribution of gas compositions

The increase in water generation indicates that tire char intensifies dehydration reactions during catalytic cracking of bio-volatiles. In addition, the generation of CO_2 and CO also indicates that decarboxylation and decarbonylation reactions occur during cracking.

It can be concluded that tire char enhances cracking/ deoxygenation reactions in the pyrolysis stage and these reactions are more pronounced for TT due to high concentration of Zn-containing minerals.

4.3.2 Characterization of pyrolytic char samples

Scanning electron microscopy micrographs of pyrolyzed raw coconut fiber and hydrochars are shown in Figure 4-7, demonstrate the morphological changes associated with the combined effect of the severity of HT conditions and pyrolysis. The longitudinal section of the raw fiber is characterized by a filamentous morphology with a relatively smooth epidermis on which there are nearly-even distributed globular protrusions. The cross-sectional area is xylem composed of a honeycombed-shaped network with hollow channels. Pyrolytic HT180 suggests that HT erodes or facilitates the erosion of protrusions resulting in pits on the fiber surface, while the inner skeletal morphology does not exhibit considerable change. It is reasonably inferred that the protrusions are composed of non-refractory biomass components such as extractives and hemicellulose.

As the HT conditions intensified, the pits were transformed into parallel reticulate micro-ridges that run parallel to strand length, leaving behind an open-structured HT recalcitrant xylem skeletal core, as shown in Figure 4-7 (d). Nitrogen adsorption test results show that pyrolyzed hydrochars have a well-developed porous structure. The surface area of the pyrolytic HT180P, HT200P, and HT220P chars is 312.7 m^2/g, 324.9 m^2/g, and 365.2 m^2/g, respectively. The SW is characterized by a smooth surface with no perceivable degree of defects or porosity, while TT has a relatively rough surface. The presence of silica-based ash clusters causes surface roughness. Detailed ash characterization is reported elsewhere [24]. The surface area of the tire chars is 111.82 m^2/g and 41.94 m^2/g for TT and SW, respectively. It should be remarked that tire char is meso/macroporous solid, [33,34] implying that premature pore coalescence during gasification, thus inhibiting the reaction through a reduction in available surface area. The surface area of chars is dependent on the type of carbon black used during tire manufacture. For example, common commercial carbon blacks, N660, NCB, and HCB have a surface area of 35.75 m^2/g, 80.08 m^2/g, and 138.90 m^2/g [33].

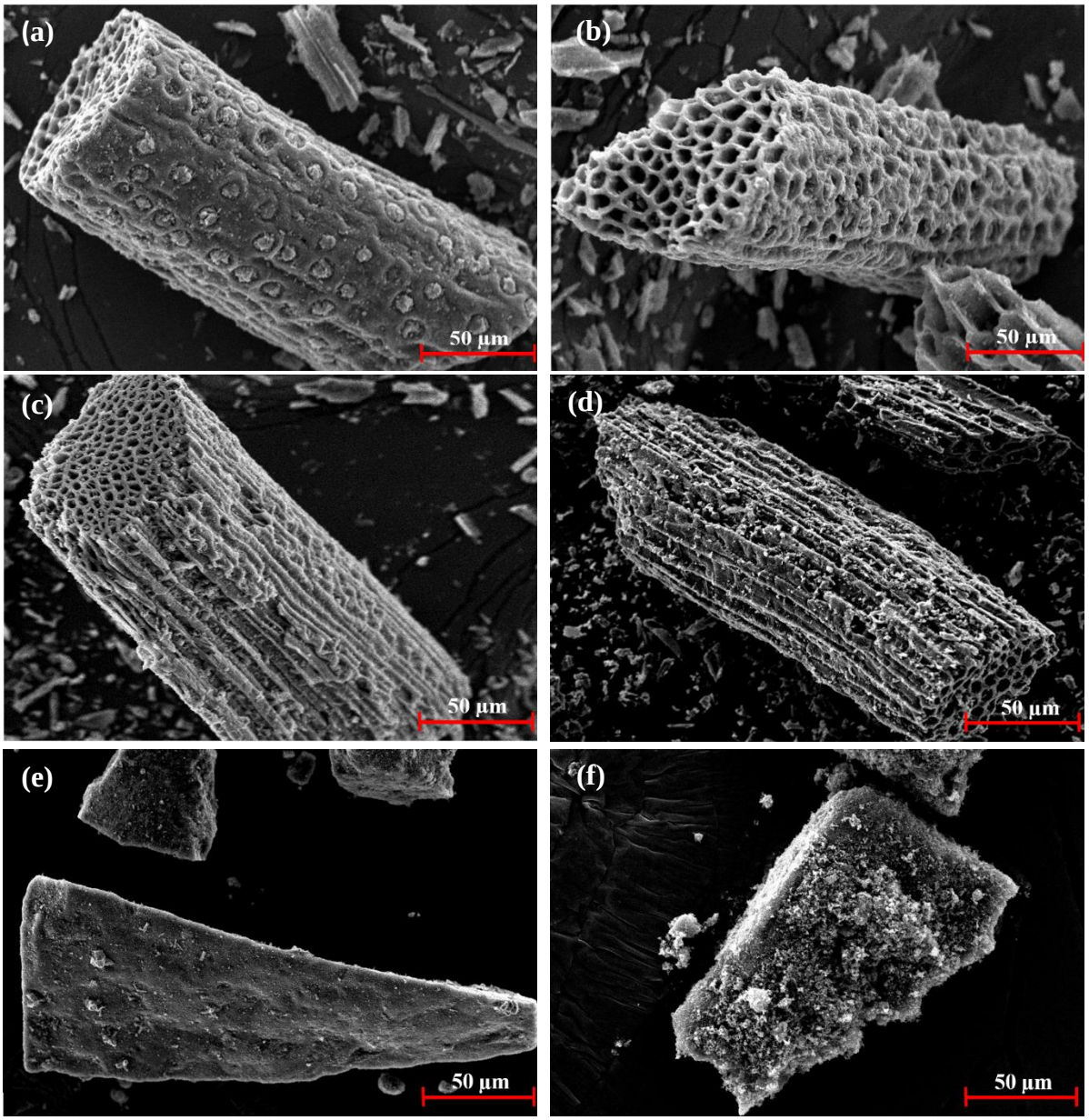

Figure 4-7. SEM images of pyrolytic samples. (a)raw coconut fiber (b) HT180 (c) HT200 (d) HT220 (e) SW (f)TT

4.3.3 Influence of inherent tire ash on gasification characteristics

Preliminary gasification tests with 10±0.5 mg samples were conducted to investigate the effect of ash on gasification, and to emphasize and make clear the distinct reaction profiles of tire char caused by a difference in ash content. The TT and SW CO_2 gasification profiles of chars are superimposed on each other and presented in Figure 4-8.

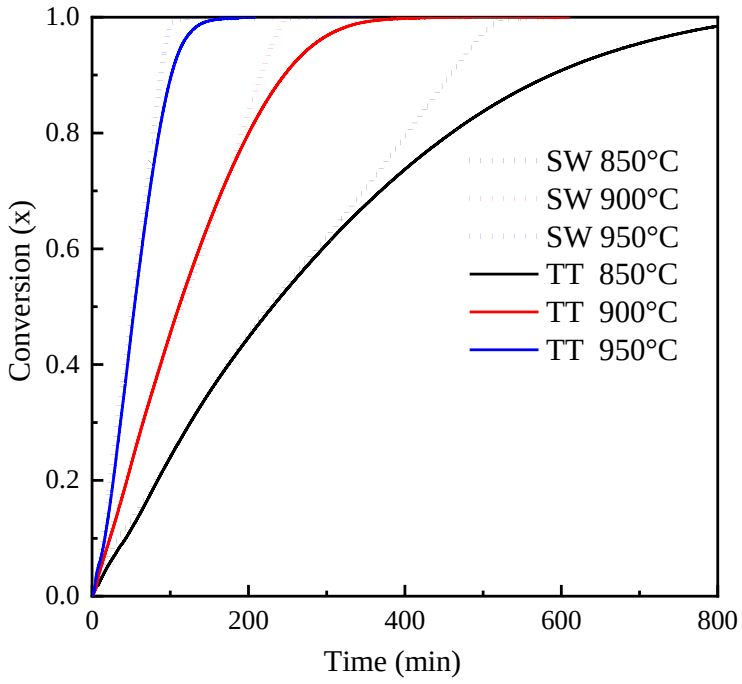

Figure 4-8. Conversion-time profiles of tire char

Line graphs indicate that the effect of ash is inconsequential at conversions averaging below 70% despite the significant difference in ash content and composition. It is observed that the profiles are coincident up to nearly 70% conversion at all temperatures, suggesting that the reactivity is similar within that range. The coincidence can be explained by considering the chemical composition of waste tire rubber.

Waste tire rubber (by order of abundance and excluding steel/fabric reinforcement) is comprised of carbon black, natural rubber, synthetic rubber, and mineral matter [35,36]. During pyrolysis, most, if not all, of the rubber is expelled as volatiles, leaving behind an ash-laden carbon-black-rich char with minor proportions of entrapped rubber remnants/deposits [34]. Therefore, tire pyrolysis can be considered a carbon black enriching or recovery process [37]. For this reason, it is reasonable to infer that the coincidence of the conversion profiles is a consequence of the reaction of the most dominant component of tire char, carbon black. Deviation from coincidence at higher conversions is attributed to the inhibiting nature of residual ash in the fixed bed, particularly silica-based ash clusters. A linear profile characterizes SW, while TT has a linear trend at lower conversions and a protracted profile at higher conversions. The effect of inherent ash is quantitatively evaluated by comparing the reaction times of these chars. In contrast to SW char, the reaction time of TT is increased by a factor of 1.58, 1.72, and 1.86 times at temperatures 850, 900, and 950°C because of mass transfer resistance imposed by the presence of silica-laden ash. Conversion profile coincidence also

suggests that ash components act as spectator inorganic species; some researchers [38] reported that tire char is mostly comprised of acid-leachable (at elevated temperature) inorganic species, which implies inactivity during gasification. Only water-soluble and ion-exchangeable inorganic AAEMs have been reported to affect gasification positively through catalysis [39,40]. For TT char, the char-ash transition for conversion less than 70% is described by the shrinking particle model, within which the carbon structure is the dominant factor, while at a later stage, transition model changes to the shrinking particle core model as the effect of accumulated ash gradually takes a more significant role [24,41]. The SW char can only be described by the shrinking particle model owing to the low content of ash [24]. To ensure that only the influence of ash is studied, the chemical structure of carbon in TT and SW char has to be similar if not the same. For this reason, the chemical structure of tire chars was determined using Raman spectroscopy.

As presented in Figure 4-9, both chars are characterized by two shifts at ~1350 cm^{-1} and ~1600cm^{-1}, these are referred to as D-band and G-band, respectively. The D-band represents structural defects and disorder in the carbon structure derived from sp^3 carbon vibrations, while the G-band represents a graphitic crystalline structure related to sp^2 carbon vibrations [42]. The intensity of the G-band is higher than that of the D-band, indicating a high degree of graphitization and a lack of structural defects; this explains the low reactivity of tire char. Visually, the two spectra suggest a similar structure in TT and SW, therefore the spectra were deconvoluted to evaluate individual band intensities quantitatively. The intensity ratio I_G/I_{all} was used to evaluate the carbon ordering degree of chars [43], a high value of the intensity ratio indicates a degree of graphitization.

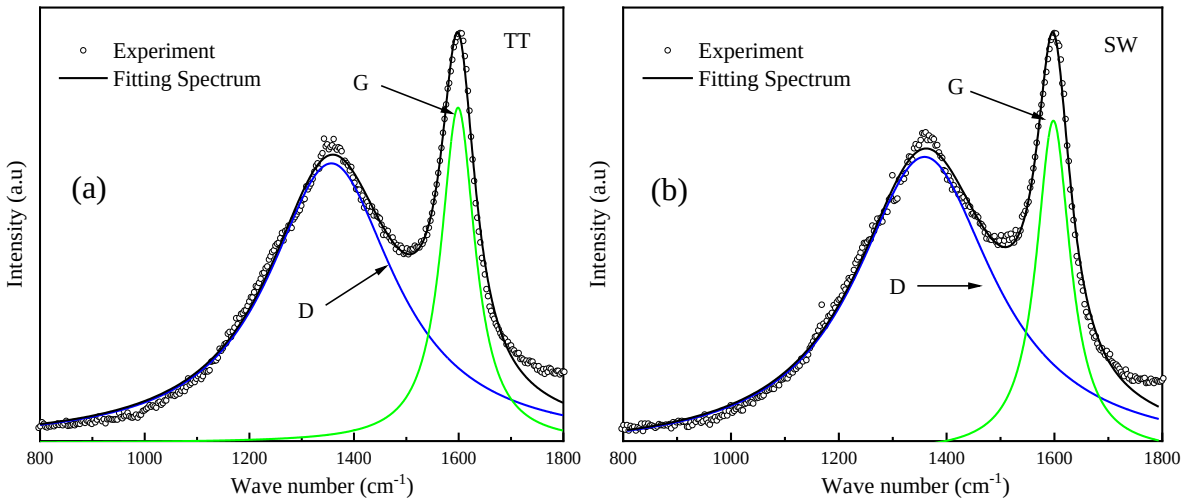

Figure 4-9. Raman spectra for (a) tire tread and (b) sidewall char

It was found that the order degree for both chars is 0.2645 ± 0.0045, with SW char exhibiting a slightly higher graphitization degree. Considering char compositions discussed hereinabove and the same thermal history of the chars, the slight variation may be due to the varying extents to which nascent pyrolytic chars expel or retain repolymerization products owing to the role of initial mineral matter.

To corroborate this speculation, one study [37] reported that pyrolytic tire char recovered for high-temperature pyrolysis is predominantly mineral-rich carbon black with carbonaceous deposits on its surface. Based on this analysis and discussion, the chemical structure of chars can be considered to be the same since the effect on gasification reactivity is slight, as demonstrated by the coincidence of SW and TT char gasification profiles.

4.3.4 The effect of blending on tire char reactivity

Gasification reactivity curves of individual and blended char samples are shown in Figure 4-10. Figure 4-11 shows the extent of gasification enhancement when tire char is blended with hydrochars.

The gasification reactivity was quantitatively evaluated by the reactivity index ($R_{0.9}$) in h^{-1}, which is calculated as follows [44]:

$$R_{0.9} = \frac{0.9}{t_{0.9}} \tag{4-7}$$

where $t_{0.9}$ is the gasification time needed to reach char conversion of 0.9.

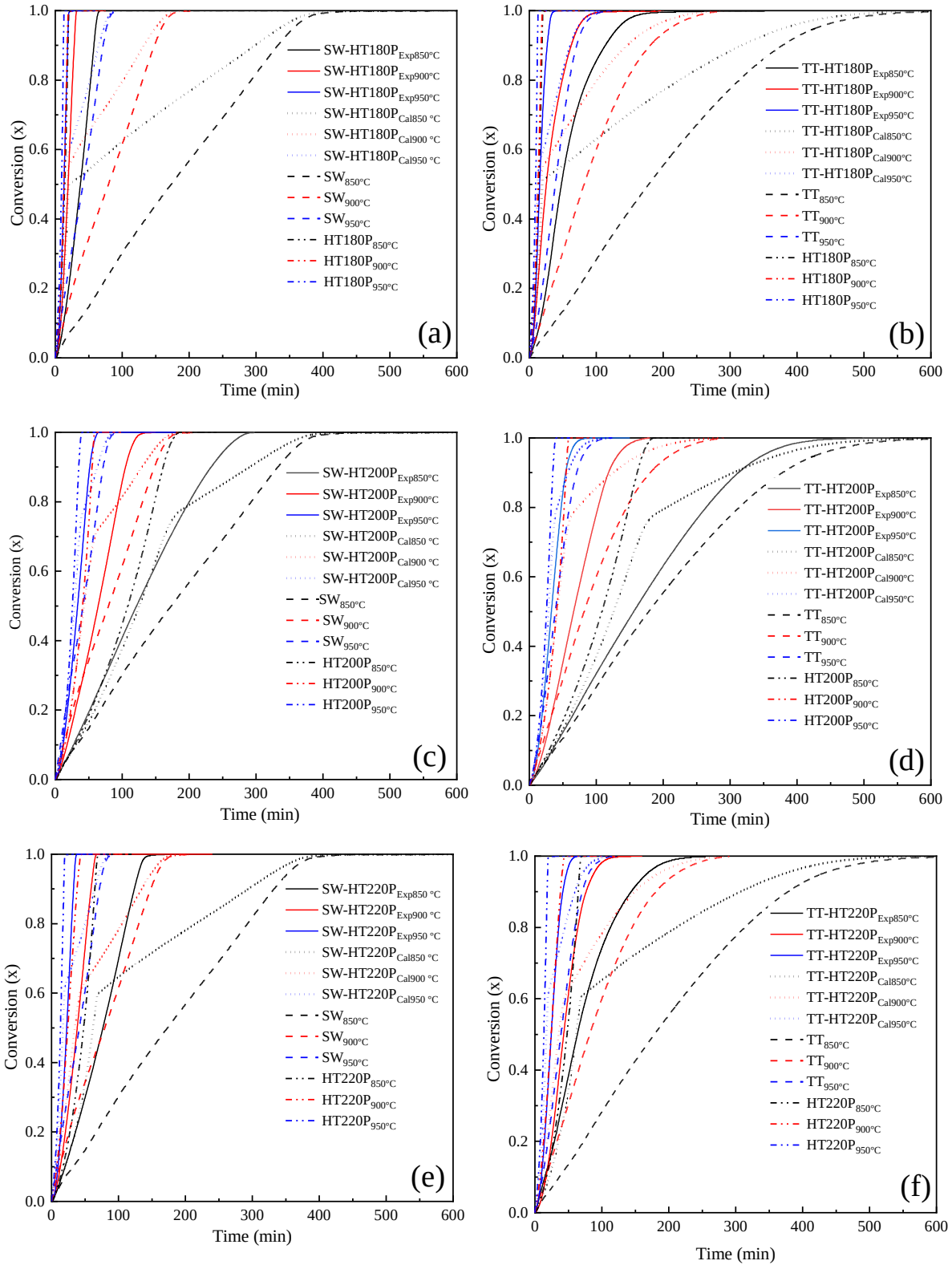

Figure 4-10. Gasification reactivity curves of tire char and tire-hydrochar blends: (a) SW-HT180, (b) TT-HT180, (c) SW-HT200, (d) TT-HT200, (e) SW-HT220, and (f) TT-HT220

It is observed that the reactivity of TT is much lower than that SW char, owing to the inhibiting nature inherent ash. Generally, the blending of tire char with hydrochar improved the reactivity of tire char. The trend of reactivity for SW and SW-hydrochar blends is; SW-HT180P > SW-HT220P > SW-HT200P > SW. The same trend was observed for TT and TT-hydrochar blends. This trend correlates well with the available AAEMs concentration in hydrochars. It is observed that HT180P has the highest enhancement effect on reactivity. The order of hydrochar reactivity enhancement follows the trend; HT180P > HT220P > HT200P. The high reactivity enhancement capacity of hydrochars emanates from the role of AAEMs. The low reactivity of tire chars is due to the low available micropore surface area, high graphitic crystalline structure, and the presence of a high concentration of acid mineral content.

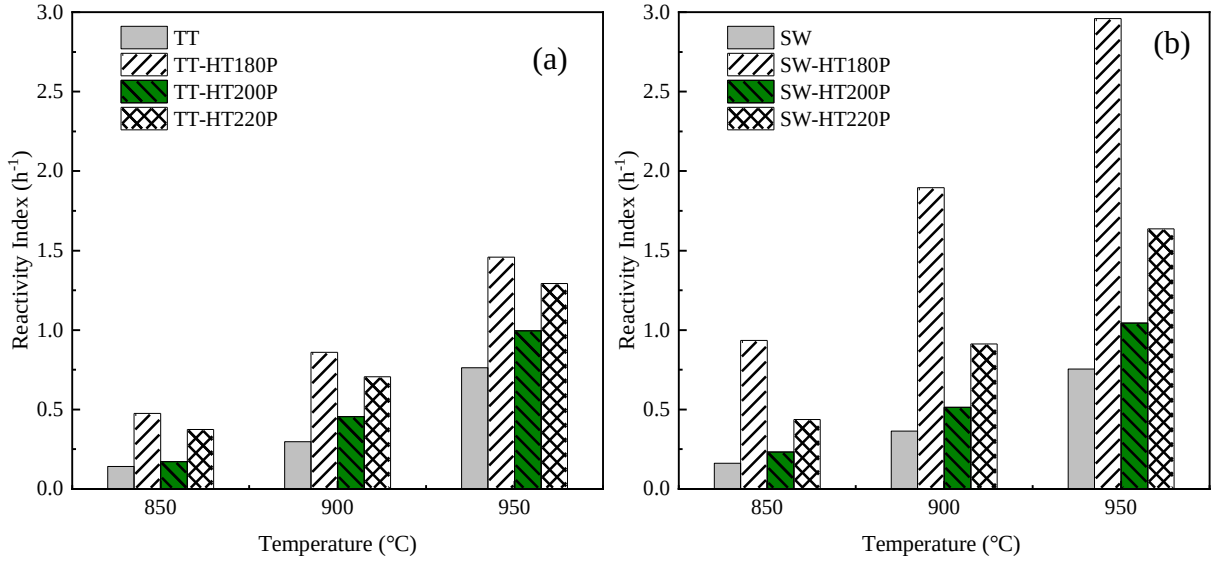

Figure 4-11. Effect of blending on the reactivity of (a) Tire tread and (b) Sidewall

The addition of hydrochars to tire chars significantly improves gasification performance. The promotional effect of elevated temperature on gasification is demonstrated in the same figure. For example, when the gasification temperature is increased from 850 to 950°C, the reactivity of SW-HT180P triples. The same figure illustrates that the extent of enhancement for SW is more pronounced compared to TT owing to the difference in ash content highlighted above. It is reasonable to infer that the inherent tire ash has an inhibiting influence on reactivity enhancement since the magnitude of reactivity indices of TT-hydrochar blends is much lower compared to SW blends.

4.3.5 Effect of blending on synergy

Reactivity curves shown in Figure 4-12 have experimental and calculated reactivity curves. Calculated reactivity curves are a result of combining individual reactivity curves of tire char and hydrochar, according to Equation 4-2. Synergistic behavior or inhibition is derived from comparing experimental and calculated reactivity curves. When the latter is higher than the former, it means there is synergistic interaction, and when the former is higher than the latter, inhibition is confirmed. A special case exists when the two curves are coincident, in which case non-interaction exists.

The synergy factor was calculated to determine the nature of interaction according to the equation; [45]

$$Synergy\ factor = \frac{R_{0.9,\exp}}{R_{0.9,cal}} \tag{4-8}$$

where $R_{0.9,cal}$ and $R_{0.9,\exp}$ denotes calculated and experimental reactivity, respectively. Figure 4-12 shows the effect of blending on the synergy factor.

The primary interaction mechanism between tire char and hydrochar was found to be the synergistic effect. Blends with SW char exhibited a stronger synergistic effect compared to TT containing blends. At all temperatures, the trend for synergy for all chars followed the trend; TC-HT180P > TC-HT220P > TC-200P. This trend has a strong correlation with the concentration of K in the hydrochars.

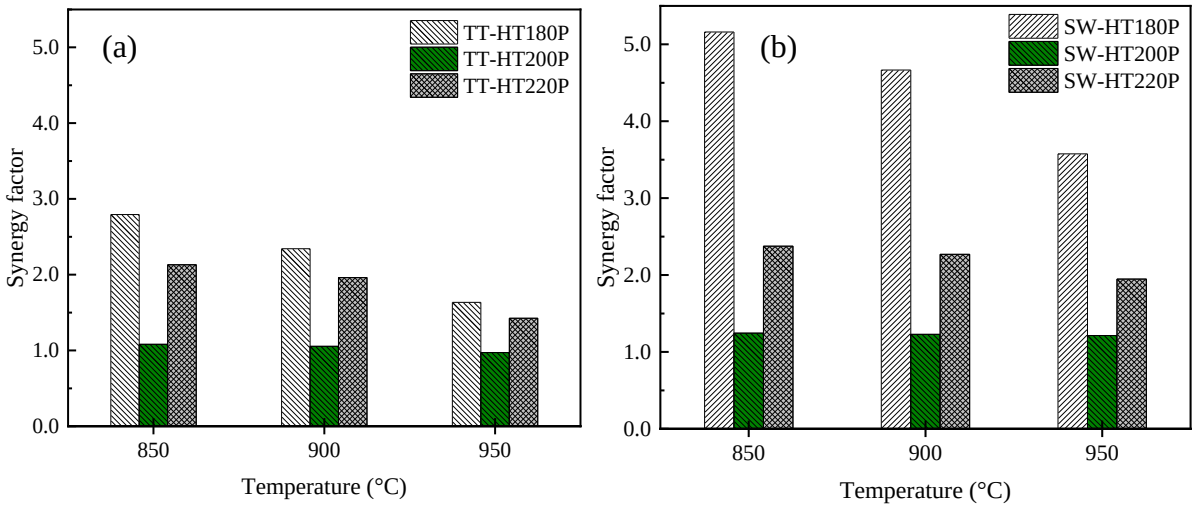

Figure 4-12. Effect of blending on synergy for (a) Tire tread and (b) Sidewall char

Interestingly, when tire chars are blended with the same hydrochar, the SW blends show a significantly higher synergy factor. This observation implies that acidic ash decreases the extent of synergy. The extent of synergy enhancement in the case of HT200P is not significant compared to HT180P and HT220P owing to low AAEM concentration and possibly deactivation thereof. An increase in temperature is marked by a decrease in the synergy factor owing to the promotion of internal and external AAEMs deactivation reaction with silica and alumina minerals. On the basis of these findings, it is concluded that an increase in AAEMs concentration promotes synergy, while an increase in temperature or acidic ash concentration hampers synergistic interaction.

The apparent negative effect of accumulated ash on tire reactivity at conversions higher than 70% is discussed hereinabove, and it is, therefore, necessary to explore the effect thereof on activation energy reduction since AAEMs are known to catalyze gasification reactions. Only conversions greater than 70% are considered in a bid to elucidate the effect of accumulated ash on co-gasification.

4.3.6 Effect of blending on activation energy reduction

It was established that ash accumulation at high conversion causes a protracted gasification time for TT; it follows that initiating and maintaining the gasification reaction becomes more energy-intensive as the reaction reaches near-completion. The effect can be observed by calculating the fractional observed activation energy of chars during gasification calculated according to the isoconversion method [31]. The same approach can be used to determine the extent to which activation energy is altered when tire char is blended.

The observed activation energy of TT and SW between the conversion range 75-95% averages between 189 and 175 kJ/mol, respectively. Blending tire char and hydrochar reduced the activation energy in all blends; however, the change for TT-HT200P is negligible, as illustrated in Figure 4-13 and Figure 4-14. This implies that the HT220P AAEMs concentration is not adequate to pose a significant catalytic effect for TT; on the contrary, SW-HT220P activation energy reduced to a range much lower compared to the former. At conversions greater than 75%, there is a significant accumulation of Si-containing ash, which increases with reaction progress, and as such, the negative effect of ash becomes more prominent. It is reasonable to infer that, for TT-HT200P, a relatively greater proportion of AAEMs is immobilized and deactivated before accessing the carbon matrix, while TT-HT180 may have more available AAEMs even after experiencing the same extent of deactivation as the former. Furthermore,

the higher concentration of AAEMs may result in suppressing carbon graphitization, thus decreasing the observed activation energy of the gasification reaction.

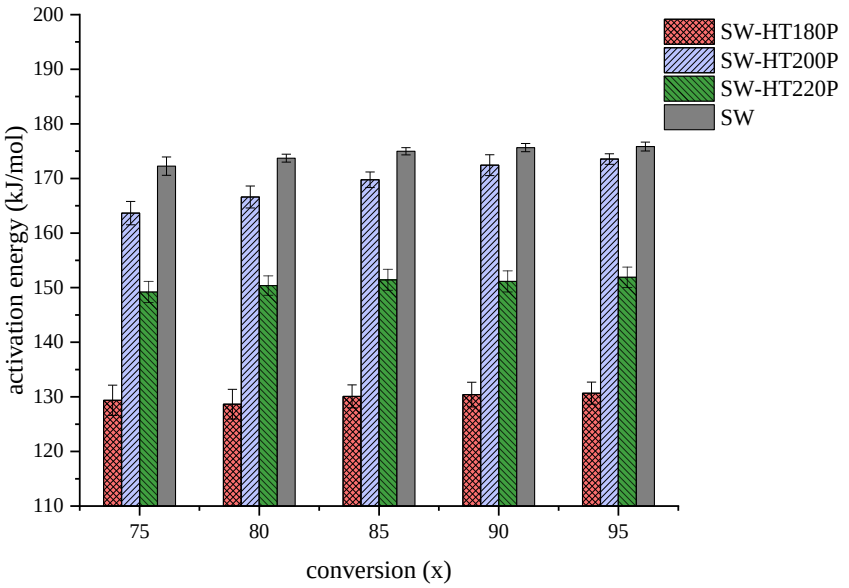

Figure 4-13. Effect of blending and conversion on activation energy for tire tread-hydrochar blends

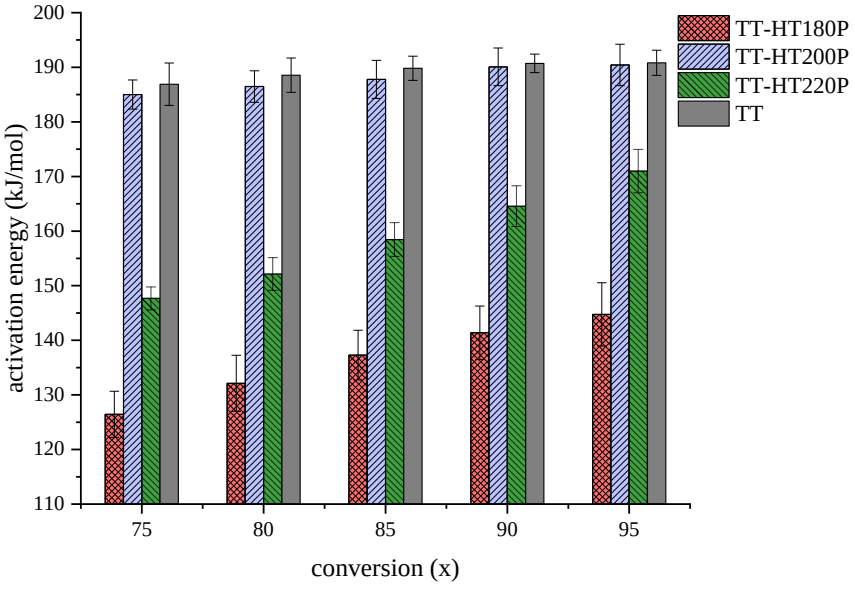

Figure 4-14. Effect of blending and conversion on activation energy for tire tread-hydrochar blends

These observations suggest that TT ash inhibits carbon matrix accessibility via mass transfer effects and (or) AAEMs transformation into inactive AAEM-aluminosilicates or silicates. By extension, comparison with SW-HT200P reveals that inherent ash inhibition is not pronounced because of the low ash content. The change in activation energy with respect to conversion for SW-HT180P and SW-HT220P shows that blending reduced the observed activation energy of

SW to an average of 130 and 151 kJ/mol, respectively. The nearly horizontal trend implies the absence of any significant inhibition effects. On the contrary, TT-HT180P and TT-HT220P observed activation energy ranges are 126 -145 kJ/mol and 148-171 kJ/mol, respectively. A positive gradient characterizes the change in activation for TT-hydrochar blends, as illustrated in Figure 4-14. This case confirms the presence of noticeable inhibition effects associated with a significant amount of acidic tire ash. The degree of activation energy reduction for all blended samples follows the trend; TC-HT180P > TC-HT220P > TC-HT200P. The trend has a good correlation with the concentration of AAEMs.

Interestingly, the trend for observed activation for tire blends with HT180P and HT220P show a good correlation with conversion-time profiles of tire char, which is near-coincidence at low conversions and divergence at higher conversions. This observation further demonstrates the negative effect of tire ash on co-gasification, and it is reasonable to infer that inhibition is a combination of mass transfer effects caused by ash accumulation and possibly a decrease in matrix accessibility by physical interception and (or) AAEMs deactivation. Further analysis was conducted to confirm the presence and degree of AAEMs transformation exhibited by different tire chars.

Tire blends with HT220P were gasified at 950°C and interrupted at 90% conversion to evaluate the degree of deactivation. The gasification temperature of 950°C was selected because the temperature in this range promotes AAEM transformation into non-active species such as alkaline metal-aluminosilicates and silicates [5]. The results are summarized in Table 4-1.

Table 4-1. AAEM concentration of blended pristine chars and semichars

samples	AAEM concentration (mg/g)		
	K	Na	Ca
TT-HT220P	17.87	7.10	11.59
TT-HT220P-90-950°C	3.12	1.03	3.27
SW-HT220P	17.80	7.13	11.58
SW-HT220P-90-950°C	3.22	1.22	9.11

Note: TC-HT220P-90-950°C is semi-char (conversion, 0.9) of TC-HT220P gasified at temperature of 950°C

Initial total AAEM concentration of blends is almost equal; however, after gasification up to 90% conversion, the concentration is reduced to a much higher degree for TT than SW. It should be noted that alkaline metals are released from char at temperatures higher than 850°C, [46,47] while calcium is retained in the char or semichar during gasification [5]. For this reason, experimental results of potassium and sodium are considered as volatilized inorganics owing

to elevated temperature. To corroborate the veracity of this reasoning, the two semichars constituting high and low-ash tire char has at least 82% reduction of alkaline metals, although ash content is different. This confirms that ash behavior other than alkaline deactivation is at play; therefore, only calcium species were considered for semi-quantitative determination of the extent of deactivation through the reaction with silica and alumina. Furthermore, there is a preferential reaction of calcium with silica compared to sodium and potassium. [48]

In the SW-HT220P blend, calcium content reduced by 21%, while TT-HT220P blend reduced by 72%, confirming the negative effect of TT silica-rich ash on co-gasification. These findings confirm deactivation as one of the mechanisms through which the capability of hydrochar to decrease tire char activation energy is reduced. The same can be used as a measure of interception since catalyst species are immobilized and prevented from accessing residual carbon structure through migration.

It should be noted that the deactivation levels may be higher than the actual levels because of the tendency of AAEMs species to stick to the alumina pan surface; however, the findings are still useful for a comparative study and should be strictly treated as apparent values. Nevertheless, the negative impact of inherent tire ash is adequately demonstrated.

4.4 Conclusion

Tire chars of different ash compositions were co-gasified with hydrochars from potassium-rich coconut fiber to gain insights on the effect of inherent tire ash on nature of interaction during pyrolysis, the extent of synergy, reactivity, and reduction of activation energy. Tire char acts as tar reforming catalyst during the pyrolysis stage and the reforming performance is more pronounced for TT than SW owing to the presence of Zn-containing minerals. During this catalytic action, deoxygenation reactions namely dehydration, decarboxylation, and decarbonylation reactions occurred. A high concentration of AAEMs enhanced reactivity, synergistic effects, and the degree of activation energy reduction. An increase in temperature promoted reactivity because of the endothermic nature of gasification reactions; in contrast, synergy decreased owing to the promotion of AAEMs transformation at elevated temperatures. The extent of enhancement for all the factors mentioned above was more pronounced for SW compared to TT, owing to the inhibiting nature of TT inherent ash. Additionally, inhibition in TT was mainly due to the high concentration of acidic ash, particularly Si-containing minerals, which acts as a site of AAEMs deactivation and, to a lesser extent, the mass transfer effect caused by accumulated ash. It may be prudent to exclude the tire tread from the tire when

considering co-gasification as it may result in high catalyst consumption and unreacted carbon, thus reducing reactor efficiency.

References

[1] Fang J, Zhan L, Ok YS, Gao B. Minireview of potential applications of hydrochar derived from hydrothermal carbonization of biomass. J Ind Eng Chem 2018. https://doi.org/10.1016/j.jiec.2017.08.026.

[2] Shen Y, Fu Y. Advances in: In situ and ex situ tar reforming with biochar catalysts for clean energy production. Sustain Energy Fuels 2018;2:326–44. https://doi.org/10.1039/c7se00553a.

[3] Czajczyńska D, Krzyżyńska R, Jouhara H, Spencer N. Use of pyrolytic gas from waste tire as a fuel: A review. Energy 2017. https://doi.org/10.1016/j.energy.2017.05.042.

[4] Oboirien BO, North BC. A review of waste tire gasification. J Environ Chem Eng 2017;5:5169–78. https://doi.org/10.1016/j.jece.2017.09.057.

[5] Wei J, Guo Q, He Q, Ding L, Yoshikawa K, Yu G. Co-gasification of bituminous coal and hydrochar derived from municipal solid waste: Reactivity and synergy. Bioresour Technol 2017;239:482–9. https://doi.org/10.1016/j.biortech.2017.05.014.

[6] Straka P, Bučko Z. Co-gasification of a lignite/waste-tire mixture in a moving bed. Fuel Process Technol 2009. https://doi.org/10.1016/j.fuproc.2009.05.021.

[7] Fermoso J, Arias B, Gil M V., Plaza MG, Pevida C, Pis JJ, et al. Co-gasification of different rank coals with biomass and petroleum coke in a high-pressure reactor for H2-rich gas production. Bioresour Technol 2010. https://doi.org/10.1016/j.biortech.2009.12.035.

[8] Rizkiana J, Guan G, Widayatno WB, Hao X, Huang W, Tsutsumi A, et al. Effect of biomass type on the performance of cogasification of low rank coal with biomass at relatively low temperatures. Fuel 2014. https://doi.org/10.1016/j.fuel.2014.06.008.

[9] He C, Giannis A, Wang JY. Conversion of sewage sludge to clean solid fuel using hydrothermal carbonization: Hydrochar fuel characteristics and combustion behavior. Appl Energy 2013. https://doi.org/10.1016/j.apenergy.2013.04.084.

[10] Mumme J, Eckervogt L, Pielert J, Diakité M, Rupp F, Kern J. Hydrothermal carbonization of anaerobically digested maize silage. Bioresour Technol 2011. https://doi.org/10.1016/j.biortech.2011.06.099.

[11] Fakkaew K, Koottatep T, Polprasert C. Effects of hydrolysis and carbonization reactions on hydrochar production. Bioresour Technol 2015. https://doi.org/10.1016/j.biortech.2015.05.091.

[12] Mosqueda A, Wei J, Medrano K, Gonzales H, Ding L, Yu G, et al. Co-gasification reactivity and synergy of banana residue hydrochar and anthracite coal blends. Appl Energy 2019. https://doi.org/10.1016/j.apenergy.2019.05.008.

[13] Yang M, Xie Q, Wang X, Dong H, Zhang H, Li C. Lowering ash slagging and fouling tendency of high-alkali coal by hydrothermal pretreatment. Int J Min Sci Technol 2019;29:521–5. https://doi.org/10.1016/j.ijmst.2018.05.007.

[14] Portofino S, Donatelli A, Iovane P, Innella C, Civita R, Martino M, et al. Steam gasification of waste tire: Influence of process temperature on yield and product composition. Waste Manag 2013. https://doi.org/10.1016/j.wasman.2012.05.041.

[15] Lee JS, Kim SD. Gasification kinetics of waste tire-char with CO2 in a thermobalance

reactor. Energy 1996;21:343–52. https://doi.org/10.1016/0360-5442(95)00119-0.

[16] Lahijani P, Zainal ZA, Mohamed AR, Mohammadi M. Co-gasification of tire and biomass for enhancement of tire-char reactivity in CO2 gasification process. Bioresour Technol 2013;138:124–30. https://doi.org/10.1016/j.biortech.2013.03.179.

[17] Lahijani P, Mohammadi M, Mohamed AR. Investigation of synergism and kinetic analysis during CO2 co-gasification of scrap tire char and agro-wastes. Renew Energy 2019;142:147–57. https://doi.org/10.1016/j.renene.2019.04.113.

[18] Shen Y. Chars as carbonaceous adsorbents/catalysts for tar elimination during biomass pyrolysis or gasification. Renew Sustain Energy Rev 2015. https://doi.org/10.1016/j.rser.2014.11.061.

[19] Shen Y, Zhao P, Shao Q, Ma D, Takahashi F, Yoshikawa K. In-situ catalytic conversion of tar using rice husk char-supported nickel-iron catalysts for biomass pyrolysis/gasification. Appl Catal B Environ 2014;152–153:140–51. https://doi.org/10.1016/j.apcatb.2014.01.032.

[20] Shen Y, Zhao P, Shao Q, Ma D, Takahashi F, Yoshikawa K. In-situ catalytic conversion of tar using rice husk char-supported nickel-iron catalysts for biomass pyrolysis/gasification. Appl Catal B Environ 2014. https://doi.org/10.1016/j.apcatb.2014.01.032.

[21] Shen Y, Zhao P, Shao Q, Takahashi F, Yoshikawa K. In situ catalytic conversion of tar using rice husk char/ash supported nickel-iron catalysts for biomass pyrolytic gasification combined with the mixing-simulation in fluidized-bed gasifier. Appl Energy 2015. https://doi.org/10.1016/j.apenergy.2014.10.074.

[22] Zhou Q, Zarei A, De Girolamo A, Yan Y, Zhang L. Catalytic performance of scrap tire char for the upgrading of eucalyptus pyrolysis derived bio-oil via cracking and deoxygenation. J Anal Appl Pyrolysis 2019;139:167–76. https://doi.org/10.1016/J.JAAP.2019.02.001.

[23] Al-Rahbi AS, Williams PT. Hydrogen-rich syngas production and tar removal from biomass gasification using sacrificial tire pyrolysis char. Appl Energy 2017;190:501–9. https://doi.org/10.1016/J.APENERGY.2016.12.099.

[24] Hungwe D, Ding L, Khoshbouy R, Yoshikawa K, Takahashi F. Kinetics and Physicochemical Morphology Evolution of Low and High-Ash Pyrolytic Tire Char during CO2 Gasification. Energy and Fuels 2020;34:118–29. https://doi.org/10.1021/acs.energyfuels.9b03043.

[25] Lahijani P, Zainal ZA, Mohammadi M, Mohamed AR. Conversion of the greenhouse gas CO2 to the fuel gas CO via the Boudouard reaction: A review. Renew Sustain Energy Rev 2015. https://doi.org/10.1016/j.rser.2014.08.034.

[26] Zhang Y, Zheng Y, Yang M, Song Y. Effect of fuel origin on synergy during co-gasification of biomass and coal in CO2. Bioresour Technol 2016. https://doi.org/10.1016/j.biortech.2015.10.076.

[27] Tay H-L, Kajitani S, Wang S, Li C-Z. A preliminary Raman spectroscopic perspective for the roles of catalysts during char gasification. Fuel 2014;121:165–72. https://doi.org/10.1016/J.FUEL.2013.12.030.

[28] Hardi F, Imai A, Theppitak S, Kirtania K, Furusjö E, Umeki K, et al. Gasification of

Char Derived from Catalytic Hydrothermal Liquefaction of Pine Sawdust under a CO2 Atmosphere. Energy and Fuels 2018;32:5999–6007. https://doi.org/10.1021/acs.energyfuels.8b00589.

[29] Chen H, Chen X, Qiao Z, Liu H. Release and transformation characteristics of K and Cl during straw torrefaction and mild pyrolysis. Fuel 2016. https://doi.org/10.1016/j.fuel.2015.11.059.

[30] Wei J, Guo Q, Gong Y, Ding L, Yu G. Synergistic effect on co-gasification reactivity of biomass-petroleum coke blended char. Bioresour Technol 2017. https://doi.org/10.1016/j.biortech.2017.03.010.

[31] Gomez A, Mahinpey N. A new method to calculate kinetic parameters independent of the kinetic model: Insights on CO2 and steam gasification. Chem Eng Res Des 2015;95:346–57. https://doi.org/10.1016/j.cherd.2014.11.012.

[32] Zhou Q, Zarei A, De Girolamo A, Yan Y, Zhang L. Catalytic performance of scrap tire char for the upgrading of eucalyptus pyrolysis derived bio-oil via cracking and deoxygenation. J Anal Appl Pyrolysis 2019;139:167–76. https://doi.org/10.1016/j.jaap.2019.02.001.

[33] Wang M, Zhang L, Li A, Irfan M, Du Y, Di W. Comparative pyrolysis behaviors of tire tread and side wall from waste tire and characterization of the resulting chars. J Environ Manage 2019;232:364–71. https://doi.org/10.1016/j.jenvman.2018.10.091.

[34] Murillo R, Navarro M V., López JM, García T, Callén MS, Aylón E, et al. Activation of pyrolytic tire char with CO2: Kinetic study. J Anal Appl Pyrolysis 2004;71:945–57. https://doi.org/10.1016/j.jaap.2003.12.005.

[35] Siddique R, Naik TR. Properties of concrete containing scrap-tire rubber - An overview. Waste Manag 2004;24:563–9. https://doi.org/10.1016/j.wasman.2004.01.006.

[36] Li G, Stubblefield MA, Garrick G, Eggers J, Abadie C, Huang B. Development of waste tire modified concrete. Cem Concr Res 2004;34:2283–9. https://doi.org/10.1016/j.cemconres.2004.04.013.

[37] Roy C, Darmstadt H. Carbon blacks recovered from rubber waste by vacuum pyrolysis - Comparison with commercial grades. Plast Rubber Compos Process Appl 1998;27:341–5.

[38] Martínez JD, Cardona-Uribe N, Murillo R, García T, López JM. Carbon black recovery from waste tire pyrolysis by demineralization: Production and application in rubber compounding. Waste Manag 2019;85:574–84. https://doi.org/10.1016/j.wasman.2019.01.016.

[39] Wei J, Gong Y, Guo Q, Ding L, Wang F, Yu G. Physicochemical evolution during rice straw and coal co-pyrolysis and its effect on co-gasification reactivity. Bioresour Technol 2017;227:345–52. https://doi.org/10.1016/J.BIORTECH.2016.12.068.

[40] Wei J, Guo Q, Gong Y, Ding L, Yu G. Synergistic effect on co-gasification reactivity of biomass-petroleum coke blended char. Bioresour Technol 2017;234:33–9. https://doi.org/10.1016/J.BIORTECH.2017.03.010.

[41] Ding L, Zhou Z, Guo Q, Wang Y, Yu G. In situ analysis and mechanism study of Char-Ash/Slag transition in pulverized coal gasification. Energy and Fuels 2015;29:3532–44. https://doi.org/10.1021/acs.energyfuels.5b00322.

[42] Sánchez-Olmos LA, Medina-Valtierra J, Sathish-Kumar K, Sánchez Cardenas M. Sulfonated char from waste tire rubber used as strong acid catalyst for biodiesel production. Environ Prog Sustain Energy 2017;36:619–26. https://doi.org/10.1002/ep.12499.

[43] Liu Z, Wang G, Zhang J, Lee JY, Wang H, Sun M, et al. Study on CO2 Gasification Reactivity and Structure Characteristics of Carbonaceous Materials from the Corex Furnace. Energy and Fuels 2018;32:6155–66. https://doi.org/10.1021/acs.energyfuels.8b00072.

[44] Gil M V., Riaza J, Álvarez L, Pevida C, Rubiera F. Biomass devolatilization at high temperature under N2 and CO2: Char morphology and reactivity. Energy 2015;91:655–62. https://doi.org/10.1016/J.ENERGY.2015.08.074.

[45] Ding L, Gong Y, Wang Y, Wang F, Yu G. Characterisation of the morphological changes and interactions in char, slag and ash during CO2 gasification of rice straw and lignite. Appl Energy 2017;195:713–24. https://doi.org/10.1016/J.APENERGY.2017.03.098.

[46] Trubetskaya A, Surup G, Shapiro A, Bates RB. Modeling the influence of potassium content and heating rate on biomass pyrolysis. Appl Energy 2017. https://doi.org/10.1016/j.apenergy.2017.03.009.

[47] Trubetskaya A, Jensen PA, Jensen AD, Steibel M, Spliethoff H, Glarborg P, et al. Comparison of high temperature chars of wheat straw and rice husk with respect to chemistry, morphology and reactivity. Biomass and Bioenergy 2016. https://doi.org/10.1016/j.biombioe.2016.01.017.

[48] Zhang ZH, Song Q, Yao Q, Yang RM. Influence of the atmosphere on the transformation of alkali and alkaline earth metallic species during rice straw thermal conversion. Energy and Fuels 2012;26:1892–9. https://doi.org/10.1021/ef2011645.

Chapter 5: **Conclusions and recommendations**

Responsible waste tire management and disposal are essential in mitigating problems that result from landfilling, open dumping, and uncontrolled burning. One such method is the thermochemical conversion of waste tires to synthesize gas via gasification. Although several studies have investigated the feasibility of gasification using laboratory scale, pilot scale, and commercial-scale reactors, the effect of inherent tire ash on (co) gasification has not been successfully evaluated owing to the inefficiency of the acid-demineralization approach in reducing mineral content to near-zero levels. This study investigates the effect of inherent ash tire ash using an unconventional approach of comparing two different parts of a tire with the same chemical structure but widely different ash concentrations, namely the high-ash tire tread (TT) and the low-ash sidewall (SW). The specific objectives of this study were the following:

Chapter 2

The aim was to evaluate the effect of inherent mineral content by comparing SW and TT char on intrinsic kinetic parameters, reactivity, and the physicochemical evolution during CO_2 gasification under isothermal conditions in a TGA. The effect of ash on activation energy, reactivity, surface area evolution, particle size reduction, and surface chemical composition using a combination of analysis methods [SEM-EDX, N_2 adsorption, and TGA].

Chapter 3

The objective of this chapter was to upgrade coconut fiber via hydrothermal treatment for co-gasification with waste tire char. The effect of hydrothermal treatment temperature on the properties of the hydrochar from coconut fiber and the influence on pyrolysis behavior is presented. The influence of treatment temperature on energy density, chemical composition, physical properties, and demineralization (K removal) is presented. Potassium removal behavior phenomena are described by considering the different factors; potassium occurrence, specific surface area, contact time, oxygenated functional groups, and pH. The effect of hydrothermal intensity on pyrolysis kinetics, mechanism, and pyrolysates was determined using TGA at different heating rates and py-GC-MS.

Chapter 4

This chapter proposed determining the nature of interactions during co-gasification of waste tire char and coconut hydrochar produced at different hydrothermal temperatures. Low-ash SW

and high-ash TT chars are compared to establish the role of inherent mineral matter on interactions. Interactions during the pyrolysis stage were determined using a two-stage fixed bed reactor and a GC analyser. The effect of inherent tire ash was evaluated by mixing tire char and hydrochar at a ratio of 50:50 and calculating the extent to which activation energy, synergy, and reactivity were altered for tire char of different ash content. These factors were evaluated under isothermal conditions in a thermogravimetric analyser.

5.1 Conclusions

Chapter 2

The effect of inherent tire mineral matter on gasification was evaluated by comparing two samples with similar chemical structures and ash content of 5.23 % for SW and 20.60 % for TT. TT char has silica-based ash clusters on its surface, while SW has a relatively smooth carbon-rich surface. Inherent ash increased the reaction time and activation energy due to forming a silica-based skeletal structure that imposed gas diffusion resistance by encapsulating residual carbon. The activation energy of SW and TT is 163.6 kJ/mol and 177.1 kJ/mol, respectively. The mineral matter in TT inhibited particle size reduction during gasification; conversely, SW was marked by significant particle size reduction. The ash also suppressed pore structure development during gasification. In conclusion, inherent ash has a negative impact on gasification kinetics and physicochemical morphological evolution.

Chapter 3

Hydrothermal treatment (180-220°C) improved the energy density of coconut fiber from 17MJ/kg to 21.5 MJ/kg at 220°C. A potassium removal efficiency of 95% can be achieved if hydrothermal treatment is followed by washing, as such liberal use of coconut fiber in gasifiers is possible without posing severe ash-related issues. However, it was found that potassium removal during hydrothermal transformation is impeded when there is significant pore structure development and an emergence of a high density of oxygenated functional groups in the coconut fiber due to increased tortuosity and electrostatic attraction. As hydrothermal treatment temperature increased, pyrolysis activation energy increased slightly; however, charring reactions were delayed due to demineralization. The pyrolysis mechanism becomes insensitive to changes in heating rate (10-50°C/min) after hydrothermal treatment. Pyrolysates produced at 600°C become rich anhydrosugar derivatives and lignin derivatives due to the combined demineralization and enrichment of cellulose achieved during pretreatment.

Chapter 4

In the pyrolysis stage of cogasification of tire char and coconut fiber hydrochars, inherent tire char catalysed cracking/deoxygenation reactions. The nature of deoxygenation reactions in order of prominence are: dehydration > decarboxylation > decarbonylation reactions. Demethanation reactions only occurred to a lesser extent compared to deoxygenation reactions. The cracking reactions are more prominent for TT than SW due to the high concentration of Zn-containing minerals. The reactivity and synergy factor increased when tire char was blended with hydrochars. The extent of enhancement is directly proportional to the potassium concentration in the hydrochars and more pronounced for SW than TT. Furthermore, activation energy reduction is inversely proportional to the potassium concentration. Tire tread chars deactivated potassium via reactions with silica to form inactive potassium silicates. It can be concluded that the inherent mineral content in tires imposes a negative effect on cogasification and consumes catalysts.

5.2 Recommendations

1. It is recommended to conduct gasification in an in-situ heating stage reactor to assess real-time morphological changes accurately.

2. Furthermore, cogasification should be conducted on a larger scale to optimize the safe potassium concentration that will significantly reduce tire activation energy and pose little to no ash-related issues in reactors.

3. A detailed study of the catalytic mechanism during cogasification should be carried out.

Practical implications

Waste tire comprises low ash and high ash components. The negative impact of ash may cause incomplete transformation of char during gasification, which lowers gasification efficiency and causes dust emission, particularly at low reactions temperatures. The waste tire can be separated such that sidewall is used as direct feedstock while TT can be used upstream as a sacrificial tar reforming agent. This simple tire pre-handling approach can mitigate problems that may arise because of the negative impact of inherent mineral matter.